Scanning tunneling spectroscopy of high-temperature superconductors

Fischer, Oystein; Kugler, Martin; Maggio-Aprile, Ivan; Berthod, Christophe; Renner, Christoph

Scanning tunneling spectroscopy of high-temperature superconductors

Øystein Fischer,* Martin Kugler, Ivan Maggio-Aprile, and Christophe Berthod

*National Center of Competence in Research on "Materials with Novel Electronic Properties"
(MaNEP) and Département de Physique de la Matière Condensée (DPMC), Université
de Genève, 24 quai Ernest-Ansermet, 1211 Genève 4, Switzerland*

Christoph Renner

*London Center for Nanotechnology and Department of Physics and Astronomy,
University College London, Gower Street, London WC1E 6BT, United Kingdom*

Tunneling spectroscopy has played a central role in the experimental verification of the microscopic theory of superconductivity in classical superconductors. Initial attempts to apply the same approach to high-temperature superconductors were hampered by various problems related to the complexity of these materials. The use of scanning tunneling microscopy and spectroscopy (STM and STS) on these compounds allowed the main difficulties to be overcome. This success motivated a rapidly growing scientific community to apply this technique to high-temperature superconductors. This paper reviews the experimental highlights obtained over the last decade. The crucial efforts to gain control over the technique and to obtain reproducible results are first recalled. Then a discussion on how the STM and STS techniques have contributed to the study of some of the most unusual and remarkable properties of high-temperature superconductors is presented: the unusually large gap values and the absence of scaling with the critical temperature, the pseudogap and its relation to superconductivity, the unprecedented small size of the vortex cores and its influence on vortex matter, the unexpected electronic properties of the vortex cores, and the combination of atomic resolution and spectroscopy leading to the observation of periodic local density of states modulations in the superconducting and pseudogap states and in the vortex cores.

PACS number(s): 68.37.Ef, 74.72.−h

CONTENTS

*Electronic address: oystein.fischer@physics.unige.ch

I. INTRODUCTION

Superconductivity is one of the most remarkable phenomena observed in physics in the 20th century. Discovered in 1911 by Kamerlingh Onnes, nearly 50 years passed before it was explained by a microscopic quantum mechanical theory. The theory published in 1957 by Bardeen, Cooper, and Schrieffer (BCS) became a universal basis for describing superconductors. Among the experimental techniques that allowed testing this theory, quasiparticle tunneling introduced by Giaever (1960) played a central role. Giaever showed that a planar junction composed of a superconducting film and a normal metal separated by a nanometer-sized thin insulator has striking current-voltage characteristics. He showed that the derivative—the tunneling conductance—has a functional dependence on voltage which reflects the BCS quasiparticle density of states. Giaever's finding was subsequently put on a firm theoretical basis by Bardeen (1961). This was the beginning of tunneling spectroscopy, which was later used by McMillan and Rowell (1965) to establish a quantitative confirmation of the BCS theory and its extension by Eliashberg (1960).

In the 1980s, two major events took place. First, the invention of the scanning tunneling microscope (STM) by Binnig and Rohrer (1982a, 1982b) opened a new world of possibilities for tunneling spectroscopy. With the technique of scanning tunneling spectroscopy (STS), it is possible to carry out spectroscopic studies with a spatial resolution down to the atomic scale, something no other technique can do. A beautiful demonstration of the possibilities for studying superconductors with this new instrument was realized when Hess *et al.* (1989) observed the vortex lattice in NbSe₂, and showed how the electronic structure of the vortex core can be explored in detail. Second, the discovery of high-temperature superconductivity in cuprates by Bednorz and Müller (1986) initiated a burst of new activity in the field of superconductivity. It was soon realized that the superconductivity in these materials might be quite different from that observed in most low-temperature superconductors. As a result numerous investigations, using many different techniques with an unprecedented level of sophistication and precision, have been carried out to study these unconventional compounds. In spite of this wealth of results we still do not have a consensus on the mechanism leading to superconductivity in the cuprates.

In this quest for an understanding of high-temperature superconductors (HTS's), it was obvious from the early days that tunneling spectroscopy could turn out to be a key experimental technique. However, tunneling experiments using various techniques struggled for a long time with what appeared to be irreproducible results. In this context the availability of the STM became an important asset for tunneling spectroscopy. The difficulty of obtaining reproducible data on the cuprates was partly due to poor control of the tunnel barrier and partly due to material inhomogeneities. Using the STM it was possible to gain control over these difficulties, to demonstrate reproducible spectra, and to identify the essential intrinsic features of tunneling spectra on high-temperature superconductors (Renner and Fischer, 1994a, 1995). Although for the study of HTS there have been important contributions from several experimental methods, STM and STS have over the past ten years made remarkable progress and greatly contributed to the worldwide effort toward an understanding of the underlying mechanism. With its unrivaled spatial and energy resolution, it is complementary to other techniques like optical spectroscopy and angle-resolved photoemission spectroscopy (ARPES) which offer k-space resolution. The STM and STS techniques promise to shine new light on the key questions in the future.

In this article we review the STM and STS investigations on high-temperature superconductors which have been reported over the last decade. In Sec. II we address experimental aspects, and in Sec. III we review the tunneling theory used for the interpretation of various STS measurements. Surface characterization is essential in this field, and these aspects are the focus of Sec. IV. The following sections then discuss the main results obtained by STS, many of which are significantly new as compared to other methods. In Sec. V we report the main results on low-temperature spectroscopy, including the studies of impurities. We then address in Sec. VI the temperature dependence of the spectra and the pseudogap as measured by STS. Intrinsic spatial varia-

tions of the tunneling spectra are discussed in Secs. VII and VIII. In the former, we focus on vortex-matter and vortex-core spectroscopy, whereas in the latter we turn our attention to the recently observed spatial periodic modulations of the tunneling conductance. Each section contains an introductory paragraph and a summary highlighting the main results. The Appendixes provide additional elements of tunneling theory and a list of the superconducting gap values observed by STS in high-temperature superconductors.

II. EXPERIMENTAL ASPECTS OF STM AND STS

The invention of scanning tunneling microscopy by Binnig and Rohrer (1982a, 1982b) set a new milestone in the world of experimental physics. Scanning tunneling spectroscopy measures the tunneling current that flows between a sharp metallic tip and a conducting sample separated by a thin insulating barrier, generally vacuum. The major technological breakthrough occurred when the control of the spacing between the tip and sample and of the lateral position of the tip using piezoelectric transducers reached picometric precision. This ability added another dimension to the well-established tunneling spectroscopy. In addition to imaging the surface topography with atomic-scale resolution, it allows one to probe the local electron density of states (LDOS) with exceptional spatial resolution and well-controlled tunneling barriers. This technical accomplishment gave rise to the development of a variety of scanning probe microscopes, which turned out to be very powerful tools to investigate materials. Scanning tunneling spectroscopy provides direct insight into fundamental properties of superconductors, such as the superconducting gap, as remarkably illustrated by the real-space imaging of the vortex lattice (Hess *et al.*, 1989).

In this section, we briefly recall the basic experimental principle of STM and STS. We shall in particular describe the general configuration and operating mode of the instrument, point out some specific technical challenges, and give an overview of the various acquisition methods used to investigate superconductors. For a more detailed description of scanning tunneling microscopy, as well as other scanning probe techniques, we refer the reader to Chen (1993), Stroscio and Kaiser (1993), and Güntherodt and Wiesendanger (1994).

A. Basic principle of STM

The phenomenon behind scanning tunneling microscopy is quantum tunneling of electrons between two electrodes separated by a thin potential barrier [Fig. 1(a)]. This phenomenon has been known since the early days of quantum mechanics, and its application to study the superconducting gap was first demonstrated in superconductor/insulator/normal metal (SIN) planar junctions (Giaever, 1960) and point-contact junctions (Levinstein and Kunzler, 1966). No spatially resolved tunneling was possible in these rigid electrode configurations. In 1981, Binnig and Rohrer developed the scan-
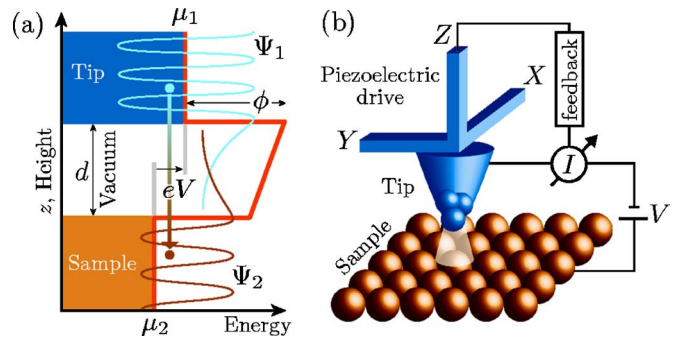
FIG. 1. (Color online) Principle of STM. (a) Tunneling process between the tip and sample across a vacuum barrier of width d and height ϕ (for simplicity, the tip and sample are assumed to have the same work function ϕ). The electron wave functions Ψ decay exponentially into vacuum with a small overlap, allowing electrons to tunnel from one electrode to the other. With a positive bias voltage V applied to the sample, electrons tunnel preferentially from the tip into unoccupied sample states. (b) Schematic view of the scanning tunneling microscope.

ning tunneling microscope. Their successful idea was to mount a sharp metallic tip, which acts as a local probe, on a three-dimensional piezoelectric drive [Fig. 1(b)]. The tip is scanned in the *x*-*y* plane above the sample using the X and Y actuators, while its height is controlled using the Z actuator. Applying a bias voltage between the metallic tip and conducting sample, and approaching the tip within a few angstroms of the sample surface, results in a measurable tunneling current. An electronic feedback loop is used to maintain this current constant by permanently adjusting the tip height.

The most striking feature of this instrument is the remarkable spatial resolution it can achieve. The key for reaching a vertical resolution of a few hundredths of an angstrom is the exponential dependence of the tunneling current I on the tip-to-sample spacing d:

$$I \sim e^{-2\kappa d}, \quad \kappa = \sqrt{\frac{2m\phi}{\hbar^2}} \approx 0.5\sqrt{\phi \text{ (eV)}} \text{ Å}^{-1}. \quad (1)$$

For a typical metal ($\phi \sim 5$ eV) the current will decrease by about one order of magnitude for every angstrom increase in the electrode spacing. The lateral resolution mainly depends on the apex geometry and electronic orbitals of the scanning tip, which confine the tunneling electrons into a narrow channel, offering the unique opportunity to perform real-space imaging down to atomic length scales. Section III provides a more detailed discussion of the theoretical aspects of electron tunneling.

The tunneling regime is defined by a set of three interdependent parameters: the electrode spacing d (typically 5–10 Å), the tunneling current I (typically 0.01–10 nA), and the bias voltage V (typically 0.01–2 V). The parameters I and V are generally chosen to set the tunneling resistance $R_t = V/I$ in the gigaohm range. It is worth mentioning that the absolute electrode spacing d is not readily accessible by experiment: only relative variations can be measured. Another important

TABLE I. Selection of homebuilt low-temperature STM's listing the main experimental conditions (temperature range, vacuum condition, magnetic field) and specific design features. This is not an exhaustive list, but rather a guide for further reading. References are classified chronologically for each refrigeration type. Abbreviations are RT, room temperature; ExGas, exchange gas; CryVac, cryogenic vacuum; UHV, ultrahigh vacuum; L^{3}He, liquid ^{3}He; and ULT, ultralow temperature.

Description	Experimental conditions			Specificities	Reference
^{4}He STM[a,b]	1.6/4.2 K	ExGas	8/10 T	Cleavage and tip-sample exchange in UHV	Kent *et al.* (1992)
^{4}He STM[a]	35 K–RT	UHV		*In situ* cleaving	Ikeda *et al.* (1983)
^{4}He STM[c]	11–400 K	UHV		*In situ* tip-sample conditioning, ^{4}He-flow cryostat	Horch *et al.* (1994)
^{4}He STM[a,c]	7 K–?	UHV	8 T	*In situ* tip-sample exchange, magnet lifted by bellow	Schulz and Rossel (1994)
^{4}He STM[a]	1.5 K–RT	ExGas	8 T	*In situ* tip-sample exchange	Tessmer *et al.* (1994)
^{4}He STM[a]	4.2 K	ExGas		Cold cleaving, magnetic coarse approach	Hancotte *et al.* (1995)
^{4}He STM[c]	15 K–RT	UHV		*In situ* sample exchange	Meyer (1996)
^{4}He STM[d]	8 K–RT	UHV	7 T	Split-coil, STM body pressed against conus	Wittneven *et al.* (1997)
^{4}He STM[a]	11 K–RT	UHV		*In situ* tip-sample condition, top loading with bellow	Foley *et al.* (2000)
^{4}He STM[d]	16 K	UHV	2.5 T	Split-coil, *in situ* tip-sample exchange	Pietzsch *et al.* (2000)
^{4}He STM	4–300 K	UHV	8 T	Rotatable field, STM cooled by superfluid ^{4}He	Kondo *et al.* (2001)
^{4}He STM[d]	6.5 K–RT	UHV		*In situ* tip-sample conditioning, ^{4}He-flow cryostat	Zhang *et al.* (2001)
^{3}He STM[d]	240 mK–RT	Cry Vac	7 T	Cold cleaving, *in situ* sample exchange	Pan *et al.* (1999)
^{3}He STM[a,b]	275 mK–RT	UHV	12/14 T	*In situ* tip-sample exchange, bottom-loading cryostat	Kugler *et al.* (2000)
^{3}He STM[a,c]	260 mK–RT	L^{3}He		Top-loading, thermally compensated STM	Urazhdin *et al.* (2000)
^{3}He STM[a]	500 mK-?	UHV	7 T	*In situ* facilities, Joule-Thomson refrigerator	Heinrish *et al.* (2003)
^{3}He STM[a,d]	315 mK–RT	UHV	12/14 T	*In situ* tip-sample conditioning, spin-polarized STM	Wiebe *et al.* (2004)
ULT STM	90 mK–RT	CryVac		*Ex situ* sample preparation	Fukuyama *et al.* (1996)
ULT STM	20 mK	UHV	6 T	*In situ* tip-sample conditioning, bottom-loading cryostat	Matsui *et al.* (2000)
ULT STM[b]	60 mK	CryVac		Very compact design, rapid cool down	Moussy *et al.* (2001)
ULT STM[b]	70 mK	CryVac	12 T	Homebuilt STM integrated into Oxford Kelvinox 100	Upward *et al.* (2001)

[a]System developed for the study of superconductors.
[b]Based on coaxial inertial slider or "slip-stick" design (Lyding *et al.*, 1988; Renner *et al.*, 1990).
[c]Based on Besocke or "beetle" design (Besocke, 1987).
[d]Based on "friction motor" design (Pan *et al.*, 1999).

point is that the measured tunneling current is a convolution of the electron densities of states of both the tip and sample (Sec. III). To study intrinsic sample properties, it is therefore preferable to use tips with a featureless density of states and a well-defined Fermi surface (ideally spherical). The metals most commonly used for the tip are Au, W, Ir, and PtIr.[1]

B. Technical challenges of low-temperature STM

A successful investigation of superconductors by STM relies essentially on three prerequisites: (i) a suitable sample surface, (ii) a scanning tunneling microscope allowing atomic resolution and stable spectroscopy; and (iii) an experimental environment featuring vacuum conditions, low and variable temperatures, as well as magnetic fields. This is a highly delicate endeavor, which requires the mastering of many technical challenges. In the

following we briefly outline the major technical difficulties, and review some of the STM designs used to study superconductors at low temperatures (see Table I).

Controlling the sample surface quality is essential. Contamination in ambient atmosphere may rapidly degrade the sample top layer, often preventing stable and reproducible tunnel junctions and the investigation of intrinsic properties. This issue is nontrivial and different for each compound, depending on its crystallographic structure and surface nature. The most suitable surfaces for STM and STS are those prepared *in situ*. Ideally, the top layers are mechanically removed by cleaving the sample in ultrahigh vacuum (UHV), either at room temperature before cooling or at low temperature. This procedure works best for the more anisotropic layered compounds with a natural cleaving plane, such as Bi2212 (Renner and Fischer, 1994a; DeWilde *et al.*, 1998; Pan *et al.*, 2001), Bi2201 (Kugler *et al.*, 2001; Shan *et al.*, 2003), Bi2223 (Kugler *et al.*, 2006), and Hg compounds (Rossel *et al.*, 1994; Wei *et al.*, 1998).

Successful STM studies have also been reported for HTS's which do not offer the advantage of a natural

---

[1]A selection of tip preparation techniques has been discussed by Ekvall *et al.* (1999).

cleaving plane, such as Y123, Nd123, and the electron-doped superconductor NCCO (Alff *et al.*, 1998). In these cases, besides cleaving in UHV (Edwards *et al.*, 1992; Pan *et al.*, 1999; Nishiyama *et al.*, 2002), a number of successful experiments have been carried out on as-grown surfaces (Maggio-Aprile *et al.*, 1995) and surfaces prepared *ex situ* by chemical etching (Wei, Tsuei, *et al.*, 1998; Shibata *et al.*, 2003b) or by cutting using a razor blade (Hayashi, Ueda, *et al.*, 1998).

Most low-temperature STM's described in this section are homebuilt and generally based on one of the following designs: the Besocke or "beetle" setup (Besocke, 1987), the coaxial inertial slider or "slip-stick" design (Lyding *et al.*, 1988; Renner *et al.*, 1990), and the "friction motor" (Pan *et al.*, 1999). A more complete description of the devices would go beyond the scope of this review: the interested reader may consult, for example, Güntherodt and Wiesendanger (1994).

Modern low-temperature STM's used for spectroscopic studies of oxide superconductors are generally mounted in a UHV chamber for the reasons mentioned above. The need for magnetic fields and ample cryogenic hold time considerably increases the system complexity. The three main design challenges are (i) ensuring optimal vibration isolation to achieve high-resolution and stable tunneling conditions, (ii) proper thermalization of the instrument to achieve low and stable temperatures, and (iii) confining the instrument inside the small bore of a superconducting coil. Table I provides a list of references for guiding the reader through the various existing low-temperature STM configurations developed to deal with these constraints.

Early low-temperature STM's were mostly based on conventional ^{4}He cryostats working at $T \geq 4.2$ K (in a few cases down to 1.5 K via a pumped ^{4}He pot), generally cooled by exchange gas. Combining low temperatures and UHV leads to more complex systems, with the difficult task of properly thermalizing the STM without coupling to mechanical vibrations. Optimal thermalization becomes even more important when subkelvin temperatures and a variable temperature range are required. Moreover, for maximal flexibility and short turnaround times, an easy *in situ* access to the STM for tip and sample exchange, as well as *in situ* tip and sample conditioning, is necessary. Magnetic fields impose further considerable size and materials constraints: the STM has to be nonmagnetic and has to fit into the coil.

In order to study ultralow-temperature phenomena with enhanced energy resolution, a few groups have developed subkelvin systems, inserting the STM into ^{3}He or dilution refrigerators. The first STS studies in small fields below 1 K were achieved by Hess *et al.*, with the historical imaging of individual Abrikosov vortex cores in NbSe$_2$, first at 300 mK using a ^{3}He refrigerator (Hess *et al.*, 1990) and later at 50 mK in a dilution refrigeration (Hess *et al.*, 1991). Other groups followed and added higher magnetic fields and/or UHV conditions with *in situ* facilities. Compared to ^{3}He refrigeration, dilution

(a) $I = \mathrm{cste} \;\Rightarrow\; \mathrm{Image} = z(x, y)$ (b) $z = \mathrm{cste} \;\Rightarrow\; \mathrm{Image} = I(x, y)$
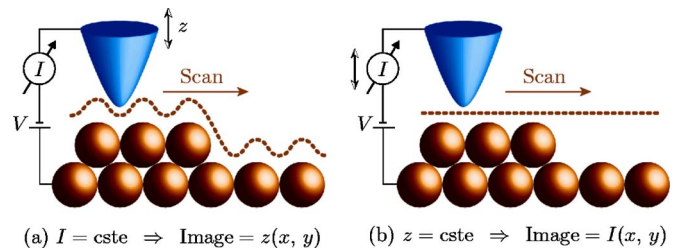
FIG. 2. (Color online) Generic STM operating modes: (a) constant-current and (b) constant-height imaging.

refrigeration offers the advantage of reaching temperatures of the order of 50 mK. However, the thermalization of the sample and STM below 100 mK is difficult, making the operation in a dilution refrigerator much more complex.

C. Operating modes

A scanning tunneling microscope offers the possibility to collect topographic and spectroscopic data on a local scale. In the topographic mode, the surface is mapped via the dependence of the tunneling current upon the tip-to-sample distance. In spectroscopy, the LDOS of the material is extracted through measurements of the tunneling conductance.

1. Topography

a. Constant-current imaging

In this standard mode, the tunneling current I is kept constant by continuously feedback-adjusting the tip vertical position during the scan [Fig. 2(a)]. Since the tunneling current integrates over all states above or below E_F, up to an energy equal to the tunnel voltage (Sec. III), the constant-current mapping corresponds to a profile of constant integrated electron density of states (DOS). If the LDOS is homogeneous over the mapped area, this profile corresponds to constant tip-to-sample spacing, and recording the height of the tip as a function of position gives a three-dimensional image of the surface $z = z(x, y)$. Because the tip follows the corrugations of the surface at a constant spacing, the scan speed is limited by the feedback loop bandwidth, which is typically in the kilohertz range.

b. Constant-height imaging

In this mode the tip is scanned over the sample surface while maintaining the tip at a constant absolute height (feedback loop turned off) [Fig. 2(b)]. For the ideal tip and sample, modulations of the tunneling current $I(x, y)$ are due only to variations in the tip-to-sample spacing, and recording the current as a function of position will reflect the surface topography. This mode allows fast scanning, but is restricted to surface areas where corrugations do not exceed a few angstroms, to avoid tip collisions with large surface protrusions. According to Eq. (1), the image corrugation de-

pends on the local work function ϕ as $d(x,y)$ $\sim \ln I(x,y)/\sqrt{\phi}$. Thus, unless the actual local value of ϕ is known, quantitative characterizations of topographic features are difficult to achieve.

2. Local tunneling spectroscopy

Locally resolved electron spectroscopy is probably the most sophisticated application of STM. The electronic density of states can be accessed by recording the tunneling current $I(V)$ while the bias voltage is swept with the tip held at a fixed vertical position. If a positive bias voltage V is applied to the sample, electrons will tunnel into unoccupied sample states, whereas at negative bias they will tunnel out of occupied sample states [Fig. 1(a)]. Although the interpretation of spectra can be quite complex, it can be shown that in ideal conditions the tunneling conductance $dI/dV(V)$ provides a valid measurement of the sample LDOS [see Eqs. (4) and (6)]. This straightforward way to interpret the experiments is used in most STM and STS studies.

dI/dV spectra can be obtained either by numerical differentiation of $I(V)$ curves or by a lock-in amplifier technique. In the latter case, a small ac-voltage modulation $V_{ac}\cos(\omega t)$ is superimposed on the sample bias V, and the corresponding modulation in the tunneling current is measured. Expanding the tunneling current into a Taylor series

$$I = I(V) + \left(\frac{dI}{dV}\right)V_{ac}\cos(\omega t) + O(V_{ac}^2),$$

one finds that the component at frequency ω is proportional to $dI/dV(V)$. This statement is valid only if $V_{ac} \ll V$ and if $I(V)$ is sufficiently smooth. For optimal energy resolution V_{ac} should not exceed $k_B T$, and typical values are in the few hundred μV range. The advantage offered by the lock-in technique is that the sampling frequency ω can be selected outside the typical frequency domains of mechanical vibrations or electronic noise, considerably enhancing the measurement sensitivity.

3. Spectroscopic imaging

Most STS experiments use "current-imaging tunneling spectroscopy" (CITS), introduced by Hamers *et al.* (1986). A CITS image is based on a regular matrix of points distributed over the surface. The tip is scanned over the sample surface with a fixed tunneling resistance $R_t = V_t/I$, recording the topographic information. At each point of the CITS array, the scan and feedback are interrupted to freeze the tip position (x, y, and z). This allows the voltage to be swept to measure $I(V)$ and/or dI/dV, either at a single bias value or over an extended voltage range. The bias voltage is then set back to V_t, the feedback is turned on, and the scanning resumed. The result is a topographic image measured at V_t and simultaneous spectroscopic images reconstructed from the $I(V)$ and/or dI/dV data. Because the feedback loop is
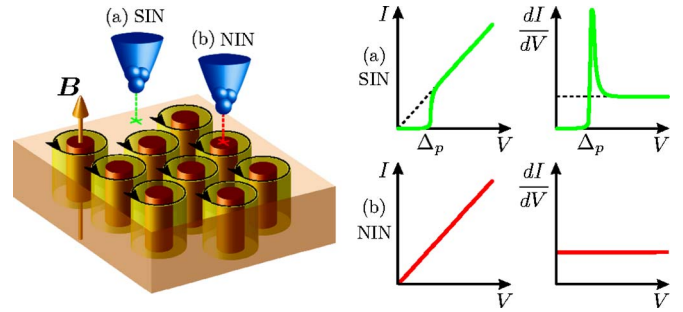
FIG. 3. (Color online) Illustration of the vortex-lattice imaging by STM: (a) Local SIN junction with typical BCS *s*-wave characteristics when the tip is between vortices. (b) Local NIN junction with a constant conductance (for a dirty BCS superconductor) when the tip is positioned over a vortex core.

interrupted, V can take any value, even those where $I(V) = 0$. This technique provides a very rich set of information.

For best contrast in the spectroscopic images it is important to select the energy where maximal variations in the tunneling conductance occur. In the case of vortex imaging (Fig. 3) the mapping energy is usually selected at the position of the coherence peaks (superconducting gap) or close to zero energy where the amplitude of the localized core states is largest (Sec. VII). This technique also enables reconstruction of spectroscopic maps acquired simultaneously at different energies. An example of such analysis was provided by Hess *et al.* (1991), who measured the energy dependence of the star-shaped vortex core structure in NbSe$_2$, and by Pan, Hudson, Gupta, *et al.* (2000), who used Fourier transforms of such maps on Bi2212 to reveal periodic modulations of the LDOS in real space (Sec. VIII). From the energy dependence of these modulations, energy dispersion curves can be extracted, opening the possibility of reciprocal-space spectroscopies in STS.

III. THEORY OF ELECTRON TUNNELING

The theory of tunneling began in the first years of quantum mechanics and now covers a large variety of experimental situations.[2] The interpretation of most tunneling measurements on high-T_c superconductors is based on the tunneling Hamiltonian formalism, which we briefly describe in Sec. III.A and present in more detail in Appendix A. In Sec. III.B we mention some of the more sophisticated approaches to electron tunneling that have been developed over the years. Section III.C is primarily dedicated to the often overlooked question of the tunneling matrix element, with a particular emphasis on the case of local vacuum tunneling (STM junction). Finally, in Sec. III.D we formulate some issues in the theoretical interpretation of tunneling experiments on HTS's.

---

[2]See, for example, Duke (1969), Wolf (1985), and the series edited by Wiesendanger and Güntherodt (1993).

FIG. 4. (Color online) Schematics of a tunnel junction. (a) Geometrical view: $\mathcal{H}_L$ and $\mathcal{H}_R$ are the Hamiltonians of the isola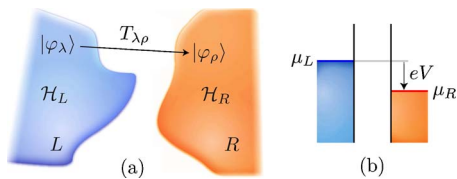ted left and right materials, respectively, and $T_{\lambda\rho}$ is the probability of tunneling from a state $|\varphi_\lambda\rangle$ on the left side to a state $|\varphi_\rho\rangle$ on the right side. (b) Energy diagram: a potential difference V is applied to the junction, resulting in a relative shift of the chemical potentials μ_L and μ_R in both materials.

A. Tunneling Hamiltonian formalism

Like any transport process, the tunneling of electrons across a vacuum or insulating barrier is a nonequilibrium phenomenon and injected quasiparticles are not *a priori* in thermal equilibrium with the lattice. In STM experiments, however, the amplitude of the current is so low that the time between two tunneling events is much longer than the typical quasiparticle relaxation time. In this situation it is appropriate to use an equilibrium theory; it is also reasonable to assume that correlations play no role in the barrier and that the elementary process involved is the tunneling of a single electron. When the two metals are superconductors, coherent tunneling of a Cooper pair can also take place, leading to the celebrated Josephson effect (Josephson, 1962).

The tunneling Hamiltonian formalism (Bardeen, 1961, 1962; Cohen *et al.*, 1962) provides a framework to understand both the single-particle and pair tunneling phenomena. The two materials forming the tunnel junction are considered as two independent systems (Fig. 4). The transfer of particles across the barrier is described by the phenomenological tunneling Hamiltonian

$$\mathcal{H}_T = \sum_{\lambda\rho} T_{\lambda\rho} c_\rho^\dagger c_\lambda + \text{H.c.} \tag{2}$$

We use the index λ to label single-particle states on the left side of the junction and the index ρ for states on the right side. The operator c_λ destroys a particle in the state φ_λ, and the operator $c_\rho^\dagger$ creates a particle in the state φ_ρ. The quantity $T_{\lambda\rho}$ is known as the tunneling matrix element. It mainly depends upon the geometry of the tunnel junction, but also on the details of the electronic states on both sides. The proper definition and explicit evaluation of $T_{\lambda\rho}$ are difficult problems which have stimulated a lot of work, especially in the case of the STM junction. We shall discuss the tunneling matrix element further in Sec. III.C.

If the bias V applied across the junction is small, the current can be calculated using linear-response theory (see Appendix A.1). The total current turns out to be the sum of two contributions I_s and I_J. The first part is the single-particle current and is given by

$$I_s = \frac{2\pi e}{\hbar} \int d\omega [f(\omega - eV) - f(\omega)]$$
$$\times \sum_{\lambda\rho} |T_{\lambda\rho}|^2 A_\lambda(\omega - eV) A_\rho(\omega), \tag{3}$$

where $A_\lambda(\omega)$ and $A_\rho(\omega)$ are single-particle spectral functions of the (isolated) left and right materials, respectively, and $f(\omega)$ is the Fermi function. Equation (3) applies to any type of tunnel junction. The most common cases, planar and STM junctions, will be discussed shortly. The meaning of Eq. (3) is obvious: the Fermi factors select the energy window where occupied states in one material—say, on the left—can be aligned with empty states on the right; within that window, an electron in a state λ can tunnel into an empty state ρ if the two states are connected by a nonvanishing matrix element and if they are aligned in energy by the applied bias. Equation (3) can also be rationalized within the simple semiconductor model (Nicol *et al.*, 1960; Tinkham, 1996). We shall not consider in this review the second contribution I_J to the current, which describes the coherent tunneling of electron pairs.[3]

The main strength of Eq. (3) is its generality: it applies to any tunnel junction, provided that tunneling takes place at energies lower than the barrier height and that high-order effects in $\mathcal{H}_T$ (such as interferences occurring within the barrier) are not important. Surface and geometric effects are in principle embodied in the spectral functions and in the matrix element. In practice one often assumes that surface disruption does not significantly change the electronic properties and that the spectral functions entering Eq. (3) can be identified with the bulk ones.

The explicit appearance of the spectral functions in Eq. (3) is another appealing feature of this formalism, which opens the door for tunneling spectroscopy. Consider a junction between a simple metal with a structureless DOS on the left—the probe—and a given material on the right—the sample. In general, the tunneling matrix element depends upon the electron quantum numbers (see Sec. III.C), but for the sake of the argument we assume here that it is a constant: $T_{\lambda\rho} \equiv T$. Then at zero temperature Eq. (3) leads to the following expression for the tunneling conductance:

$$\sigma(V) = \frac{dI_s}{dV} = \frac{2\pi e^2}{\hbar} |T|^2 N_L(0) N_R(eV), \tag{4}$$

where L and R denote "left" and "right" and $N(\omega)$ is the DOS measured from the Fermi energy. This simple formula shows the essence of tunneling spectroscopy: the bias dependence of the tunneling conductance directly

---

[3]The observation of the Josephson current by STM using a superconducting tip is challenging because it requires a relatively low junction resistance. This type of experiment has not been reported so far for the HTS's, but was recently achieved with conventional superconductors (Namman *et al.*, 2001; Suderow *et al.*, 2002; Martinez-Samper *et al.*, 2003; Naaman and Dynes, 2003, 2004; Rodrigo and Vieira, 2004).

probes the DOS of the sample. This result is not valid in general, however, as discussed in Sec. III.C. The correspondence between the tunneling conductance and sample DOS, first postulated by Giaever (1960), was the initial motivation for the Bardeen (1961) tunneling theory.[4]

For understanding local probes like STM, it is helpful to express Eq. (3) in terms of the real-space spectral function, which is closely related to the LDOS (Appendix A.1). Tersoff and Hamann (1983) performed the first calculation of the tunneling matrix element for the STM junction and found an explicit relation between the tunneling current and the sample LDOS $N_{sample}(x, \omega)$:

$$I_s \propto \int d\omega [f(\omega - eV) - f(\omega)]$$
$$\times N_{tip}(\omega - eV) N_{sample}(x, \omega), \quad (5)$$

where x denotes the tip center of curvature (Appendix A.2). Assuming a structureless tip DOS, $N_{tip}(\omega - eV)$ = const, Eq. (5) gives

$$\sigma(x, V) \propto \int d\omega [-f'(\omega - eV)] N_{sample}(x, \omega), \quad (6)$$

where f' is the derivative of the Fermi function. Thus the interpretation of scanning tunneling spectroscopy becomes remarkably simple: the voltage dependence of the tunneling conductance measures the thermally smeared LDOS of the sample at the position of the tip. Because the local tunneling matrix element is properly taken into account, Eq. (6) describes the STM much better than Eq. (4) describes planar junctions.

B. Other approaches to the tunneling problem

The success of the tunneling Hamiltonian formalism in describing many experimental results, in particular the Josephson effect, led several authors to investigate this approach in depth. One of the first questions raised concerned the primary assumption of the theory—namely, the possibility of representing the junction as two independent systems coupled by a term like $\mathcal{H}_T$. Not surprisingly it was found that this assumption is not valid in general (Prange, 1963; Zawadowski, 1967); however, the associated error turned out to be small. The effect of interactions in electrodes and in the barrier was also investigated (Schrieffer, 1964; Scalapino *et al.*, 1966; Appelbaum and Brinkman, 1969a, 1969b; Duke, 1969); this allowed, in particular, an explanation of the fine structure of conductance in BCS superconductors in terms of the phonon spectrum (McMillan and Rowell, 1965). The most significant improvements on the original theory are perhaps the incorporation of nonequilibrium effects by

means of the Keldysh formalism (Caroli *et al.*, 1971; Feuchtwang, 1974), and nonperturbative treatments (Noguera, 1990; Sacks and Noguera, 1991), which gave useful information on the accuracy of the perturbative approach. The resulting theories are rather complicated, and have not yet been used in context of the high-T_c superconductors.

In order to avoid difficulties inherent to the tunneling Hamiltonian formalism and for treating the regime where the interaction between the two materials cannot be neglected, several authors proposed approaches based on scattering theory (Lucas *et al.*, 1988; Doyen *et al.*, 1993; Cuevas *et al.*, 1996; Ness and Fisher, 1997; Carminati and Sáenz, 2000), in the spirit of the Büttiker *et al.* (1985) transport theory. For superconducting junctions, the most popular method is due to Blonder *et al.* (1982). Initially developed for planar junctions involving a BCS s-wave [or d-wave (Tanaka *et al.*, 1995)] superconductor, this approach was nevertheless occasionally used to interpret STM spectra on HTS materials.

Another approach was explored by Lang (1985), who represented both tip and sample by a single atom adsorbed on a jellium surface, and calculated the tunneling current using a first-principles method. This study illustrated the atomic character of the STM junction, which in effect can be viewed as an atom-to-atom contact (see also Tsukada *et al.*, 1983), and initiated many subsequent works based on *ab initio* methods (see, e.g., Ciraci and Batra, 1987; Tersoff, 1989; Hofer *et al.*, 2001, 2003).

C. Tunneling matrix element

In the Bardeen (1961) theory the matrix element is the expectation value of the single-particle current in the direction z normal to the plane of the junction, through a surface S lying entirely in the barrier region:

$$T_{\lambda\rho} = -\frac{\hbar^2}{2m} \int_S dS \left(\varphi_\rho^* \frac{\partial \varphi_\lambda}{\partial z} - \varphi_\lambda \frac{\partial \varphi_\rho^*}{\partial z} \right). \quad (7)$$

Duke (1969) and Wolf (1985) give comprehensive reviews of the various models for $T_{\lambda\rho}$ developed prior to the invention of the STM. Hereafter we describe the most popular models for planar and STM junctions.

1. Planar junction

$T_{\lambda\rho}$ has a particularly simple form at ideal planar junctions, due to conservation of momentum in the plane parallel to the interface (Harrison, 1961; Duke, 1969; Wolf, 1985). The exponential decay of the wave functions in the barrier leads to an exponential dependence of $|T_{\lambda\rho}|^2$ on the barrier thickness d, which reduces to $\exp(-2\kappa d)$ in the limit of a wide and square barrier; $\kappa = [(2m/\hbar^2)(U - \varepsilon_z)]^{1/2}$ is the electron momentum in the barrier and ε_z is the energy for the motion normal to the interface, measured from the top U of the barrier. This exponential factor suggests that the tunneling current is dominated by states with a large velocity along the z direction and consequently a small momentum in the

---

[4]For SIS junctions, i.e., junctions involving two superconductors separated by a thin insulating barrier, Eq. (3), and the assumption $T_{\lambda\rho} \equiv T$ yield a partial convolution of the materials' DOS's instead of the DOS itself, that is, $I_s \propto \int_0^{eV} d\omega N_L(\omega - eV) N_R(\omega)$ at zero temperature.

(x,y) plane, leading to a momentum selectivity often referred to as the "tunneling cone" (Beuermann, 1981). The matrix element is also proportional to the group velocity along z (Harrison, 1961). In Eq. (3), however, this velocity factor $\partial \xi_{\boldsymbol{k}}/\partial k_z$ is canceled by an equivalent DOS factor. A counterintuitive consequence of this cancellation is the possibility of tunneling along the c axis into a quasi-two-dimensional material (without dispersion along k_z), in spite of the low conductivity in the z direction. This latter property would imply that k_z-related DOS features should not show up at all in planar tunneling spectra (Harrison, 1961), in sharp contrast with the simple result of Eq. (4), and with the experimental observation of the superconducting DOS by Giaever. Bardeen (1961) attributed this discrepancy to the fact that electrons are not paired in the barrier region; thus the velocity entering $T_{\lambda\rho}$ would be the velocity of bare electrons rather than the quasiparticle velocity $\partial E_{\boldsymbol{k}}/\partial k_z$, and the superconducting gap would show up in tunneling spectra, although the normal-state DOS would not.

It should be noted that these arguments apply to materials with spherical Fermi surfaces and isotropic superconducting gaps and must be reconsidered when dealing with cuprate superconductors. As pointed out by Wei, Tsuei, *et al.* (1998), the tunneling cone "flattens out" for c-axis tunneling into the ab plane of the HTS, because ε_z is almost independent of the in-plane momentum. Therefore one expects to measure the ab-plane band structure in the planar c-axis tunneling spectra of the HTS's.

2. STM junction

Because of lateral confinement, one-electron states of the STM tip cannot be characterized by a single momentum in the (x,y) plane, which makes the calculation of the tunneling matrix element more difficult than in the planar junction case. Soon after the invention of the STM, Tersoff and Hamann (1983, 1985) proposed an expression for $T_{\lambda\rho}$ that is still widely used to interpret STM images. They represented the tip apex by a spherical potential well and found that Bardeen's matrix element, Eq. (7), is proportional to the sample wave function at the center $\boldsymbol{x}$ of the tip apex:

$$|T_{\lambda\rho}|^2 \propto |\varphi_\rho(\boldsymbol{x})|^2. \tag{8}$$

Using Eq. (8) they were able to explain the measured corrugations for various superstructures observed on the reconstructed Au (110) surface. The case of a nonspherical tip and a rough sample surface was later treated along the same lines (Sacks *et al.*, 1988; Šestović and Šunjić, 1995). In these models the atomic structure of the tip is not taken into account. This issue was investigated by Chen (1988, 1990a, 1990b), who assumed instead that a single atom at the tip apex is responsible for the interaction with the sample surface. Chen summarized his results in a derivative rule: $T_{\lambda\rho}$ is proportional to a derivative of the sample wave function; the kind of derivative depending upon the orbital state of the apex atom.

Equation (8) can be regarded as a particular case appropriate for s-wave tips. The unexpectedly large corrugation amplitudes observed on HTS surfaces could possibly be explained using this formalism.

According to Eq. (8) and the resulting Eq. (5), c-axis STM tunneling into a nearly two-dimensional material is possible, as for a planar junction, but for different reasons. On the one hand, the local nature of the STM tip explains its ability to measure all momenta in the ab plane, thus preventing any momentum selectivity. On the other hand, $T_{\lambda\rho}$ in Eq. (8) is not proportional to the group velocity along z, in contrast to the planar junction case. The complete absence of a velocity factor in Eq. (8) results from specific approximations made by Tersoff and Hamann, such as having a spherical tip wave function and identical work functions in the sample and tip; the relaxation of these assumptions would yield some dependence upon the group velocity, but is not expected to change the picture qualitatively.

D. Interpretation of STM experiments on HTS's

A consistent interpretation of STM experiments on HTS's must address two different questions. The first concerns the electronic nature of the materials themselves, and the second is the coupling of material surfaces with the STM tip. Until now theorists have focused on the former problem, and made considerable progress; several excellent reviews of this effort were given recently.[5] In this section we leave this question aside and address some issues related to the tunneling process itself, concentrating on the Bi2212 compound.

Generally the conditions of the STM measurements on HTS's are consistent with the basic assumptions of the tunneling Hamiltonian theory. The absence of a substantial interaction between tip and sample was evidenced by the insensitivity of the tunneling conductance to the tip-sample distance (Renner and Fischer, 1995). The interval between two tunneling events is typically 10^{-10} s for a current of 1 nA, which is long compared to the relaxation times $\lesssim 10^{-12}$ s in the materials; therefore, nonequilibrium effects are not expected to play a role in STM spectra.

1. Role of the BiO surface layer

Many STM experiments on Bi2212 have been successfully interpreted using Eq. (6). It is commonly believed that the measured LDOS originates from the CuO_2 bilayer (see Fig. 5). According to Eq. (6), though, the LDOS is not measured directly on a CuO_2 plane, but at some point $\boldsymbol{x}$ typically 10 Å above that plane, since Bi2212 cleaves between weakly bonded BiO sheets. The CuO_2 layer lies 4.5 Å beneath the surface BiO layer,

---

[5] Dagotto (1994); Anderson (1997); Orenstein and Millis (2000); Chubukov *et al.* (2003); Kivelson *et al.* (2003); Norman and Pépin (2003); Sachdev (2003); Carlson *et al.* (2004); Demler *et al.* (2004); Lee *et al.* (2006). This is not an exhaustive list.
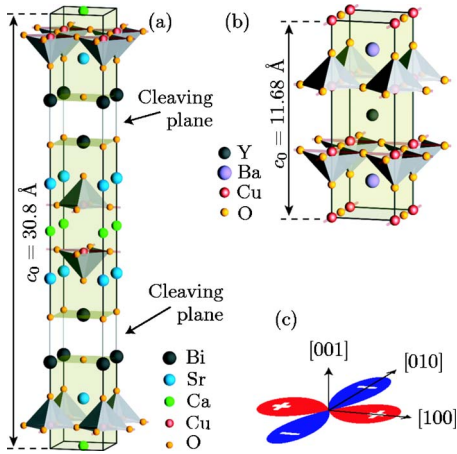
FIG. 5. (Color online) Crystal structure of the cuprate materials. (a) Tetragonal unit cell of $Bi_2Sr_2CaCu_2O_{8+\delta}$ with $a=b$ $=5.4$ Å defined along [110] and [$\bar{1}$10], respectively. (b) Orthorhombic unit cell of $YBa_2Cu_3O_{6+\delta}$ with $a_0=3.82$ Å along [100] and $b_0=3.89$ Å along [010]. (c) Schematics of the $d_{x^2-y^2}$ superconducting gap in the unit-cell coordinate system. Note that a_0 and b_0 designate the lattice constants along the Cu-O-Cu bonds (*Pmmm* space group for Y123), whereas a and b designate the lattice constants in larger unit cells (*Cmmm* space group for Bi2212).

raising the question of the role played by BiO in the tunneling process from the STM tip to the CuO_2. That BiO indeed plays a significant role is obvious from the topographic images, which show the lattice of Bi atoms on the surface (see Sec. IV.A).

Band calculations indicate that the BiO layer is metallic.[6] This result contradicts the common experimentalist's wisdom that the BiO layer is insulating. The metallic nature of BiO in these calculations is due to a pair of conduction Bi($6p$)-O($2p$) hybrids, which disperse below the Fermi energy in a small region around the $(\pi,0)$ point of the Brillouin zone. It is well known that correlation effects on the Cu($3d$) orbitals lead to a failure of the local density approximation (LDA) approaches in the antiferromagnetic phase; such effects are not expected in the BiO layer. Therefore, a Bi-O band at the Fermi surface should give rise to a sharp peak in the spectral function near E_F. This peak is not seen in ARPES experiments (Damascelli *et al.*, 2003; Campuzano *et al.*, 2004), suggesting that the Bi-O band indeed lies above E_F. Singh and Pickett (1995) found that in Bi2201 the calculated Bi-O bands move upward by ~400 meV when the distortion of the BiO planes is taken into account. Very recently, Lin *et al.* (2006) found that a similar shift occurs in Bi2212 when lead or oxygen doping is introduced in the calculation.

If the BiO surface layer is not conducting, then at sufficiently low energies STM will necessarily measure

[6]Herman *et al.* (1988); Hybertsen and Mattheiss (1988); Krakauer and Pickett (1988); Massidda *et al.* (1988); Mattheiss and Hamann (1988); Szpunar and Smith (1992); Jarlborg and Santi (2000).

the spectral properties of the buried CuO_2 bilayer. The observation of the Bi lattice in topographic images could then be due to, e.g., (i) a modulation of the shape of the tunnel barrier by the Bi atoms, (ii) a diffraction of the tunneling electron by the BiO (and SrO) intermediate layers, (iii) the admixture of some Bi($6p$) character in the Cu($3d$)-O($2p$) states of the CuO_2 bilayer, or (iv) the fact that the bias applied to record the topography (typically $\gtrsim0.5$ V) would lie within the Bi-O bands.

2. Momentum dependence of the matrix element

The matrix element Eq. (8) is local in space [see also Eq. (A15)]. In some instances, especially in the context of STM tunneling on impurities (Sec. V.E), it has been claimed that the matrix element could be nonlocal, i.e., could depend upon the sample wave function in some vicinity of the tip position x. A phenomenological generalization of Eq. (8) taking into account this possibility would be

$$T_{\lambda\rho} \propto \int d\mathbf{r} M(\mathbf{r}-\mathbf{x})\varphi_\rho^*(\mathbf{r}). \tag{9}$$

The function M weighs the various contributions of the sample wave function around the tip and reduces to $\delta(\mathbf{r}-\mathbf{x})$ for a local matrix element. For a translationally invariant system, Eq. (9) leads to (Appendix A.3)

$$\sigma(V) \propto \int d\omega[-f'(\omega-eV)]\sum_{\mathbf{k}} |M_{\mathbf{k}}|^2 A(\mathbf{k},\omega), \tag{10}$$

where $M_{\mathbf{k}}$ is the Fourier transform of $M(\mathbf{x})$ and $A(\mathbf{k},\omega)$ is the sample spectral function.[7] The vector $\mathbf{k}$ in Eq. (10) belongs to the three-dimensional Brillouin zone of the sample. In the case of HTS's, though, the k_z dependence of the spectral function can be neglected to first approximation and the k_z sum does not contribute to the V dependence of $\sigma(V)$. Anisotropic matrix elements $M_{\mathbf{k}}$ have been invoked for interpretation of various experimental results, as discussed in Secs. IV.A.2, V.E, VII.B.2, and VII.D.

The STM measurements on zinc impurities in Bi2212 (Pan, Hudson, Lang, *et al.*, 2000; see Sec. V.E) revealed a sharp maximum in the LDOS at the impurity site. Similar spectra were observed on surface defects (Yazdani *et al.*, 1999). These observations contrast with the prediction of the BCS theory in the unitary limit, namely, a vanishing LDOS on the impurity and resonances on neighboring sites (Salkola *et al.*, 1996). Martin *et al.* (2002) argued that tunneling into the planar Cu($3d$) orbitals occurs indirectly through Cu or Bi orbitals extending out of the surface and having zero in-plane orbital

[7]The assumption of translational invariance excludes from the outset any atomic-scale dependence of the tunneling conductance. Hence Eq. (10), unlike Eq. (6), cannot address the question of the atomic resolution or describe inhomogeneous systems like vortex cores. Equation (A18) provides a suitable generalization of Eq. (6) to account for a nonlocal matrix element.

momentum. As a result the STM would not probe the wave function at the Zn site, but at the four neighboring Cu sites (see Fig. 18, below). The weighting function in Eq. (9) would then take the form $M(\boldsymbol{x}) \propto \delta(\boldsymbol{x}-\boldsymbol{a}_0)+\delta(\boldsymbol{x}+\boldsymbol{a}_0)-\delta(\boldsymbol{x}-\boldsymbol{b}_0)-\delta(\boldsymbol{x}+\boldsymbol{b}_0)$, where $\boldsymbol{a}_0$ and $\boldsymbol{b}_0$ are the basis vectors of the Cu lattice. The opposite signs along the a and b directions reflect the $d_{x^2-y^2}$ symmetry of the CuO_2 orbitals near E_F. In reciprocal space this corresponds to $|M_{\boldsymbol{k}}|^2 \propto (\cos k_x a_0 - \cos k_y b_0)^2$. The absence of a large zero-bias conductance peak in vortex cores was also tentatively attributed to matrix-element effects (Wu *et al.*, 2000; see Sec. VII.B.2). In the STM literature, this $d_{x^2-y^2}$ matrix element is often attributed to Chakravarty *et al.* (1993), although these authors introduced it for describing the coherent tunneling of Cooper pairs in bilayer compounds. Franz and Teŝanović (1999) obtained the same result for a planar junction, after summing over the momenta along the c axis, and argued that this matrix element would prevent STM from measuring the Doppler-shift-induced zero-energy DOS in the mixed state (Volovik, 1993; see Sec. VII.D). Finally, a similar form for $|M_{\boldsymbol{k}}|^2$ (with a plus sign instead of a minus sign) was also suggested by arguing that direct tunneling into planar CuO_2 orbitals is blocked by atomic cores in intermediate SrO and BiO layers (Zhu *et al.*, 2000).

The anisotropic $d_{x^2-y^2}$ matrix element would prevent electrons from tunneling into states with momenta along the nodal directions and would therefore highlight the $(\pi,0)$ region of the Brillouin zone. For a homogeneous d-wave superconductor the low-energy conductance resulting from Eq. (10) with an anisotropic $M_{\boldsymbol{k}}$ would show a rounded U shape instead of the V shape characteristic of nodal quasiparticles. However, after a detailed fit of the Bi2212 data, Hoogenboom, Berthod, *et al.* (2003) concluded that the low-energy conductance is incompatible with an anisotropic matrix element. Recent observation that the STM spectra measured directly on the CuO_2 layer exhibit a U shape, while the spectra taken on the BiO layer have the d-wave V shape (Misra *et al.*, 2002a; see Sec. IV.A.2), was attributed by the authors to a different matrix element in the two tunneling configurations.

The actual form of the matrix element for STM tunneling into HTS's remains largely controversial.[8] Since

---

[8]Some authors analyzed tunneling spectra on HTS's using a matrix element analogous to the one derived by Harrison for planar junctions, $|M_{\boldsymbol{k}}|^2 \propto v_g$ (Kouznetsov and Coffey, 1996) or $|M_{\boldsymbol{k}}|^2 \propto v_g D(\boldsymbol{k})$ (Yusof *et al.*, 1998). The main motivation was to explain the absence of some sharp structures, such as van Hove singularities, in experimental tunneling spectra, and the observed asymmetry in the background conductance (Sec. V) as well as specific features observed in point-contact tunneling experiments. Here v_g is the group velocity and $D(\boldsymbol{k})$ is a function selecting the momenta close to the tunneling direction, which was introduced by Ledvij and Klemm (1995) as a generic model for Josephson coupling between planar superconductors. The validity of these planar-junction matrix elements in accounting for the STM and point-contact geometries was not addressed, however.

no direct experimental determination of $T_{\lambda\rho}$ (or $M_{\boldsymbol{k}}$) has been possible so far and no microscopic calculation of the tip-surface system has been reported, most assessments about the matrix element rely upon phenomenological or heuristic arguments. The V-shaped spectra acquired on the BiO layer support the idea of a Tersoff-Hamann-like matrix element, i.e., $M_{\boldsymbol{k}} \equiv 1$. Although there is no compelling experimental evidence in favor of an anisotropic $M_{\boldsymbol{k}}$, measurements on zinc impurities and possibly also on vortices could be interpreted in the framework of the BCS theory assuming a more complicated matrix element like $M_{\boldsymbol{k}} \propto \cos k_x a_0 - \cos k_y b_0$. However, alternate explanations which emphasize the non-BCS character of HTS have also been proposed.

E. Summary

Most STM spectroscopic measurements on HTS's have been successfully analyzed in the framework of the tunneling Hamiltonian formalism. Complemented with the Tersoff and Hamann treatment of the STM junction, this formalism provides a straightforward interpretation of the tunneling data, Eq. (6), in terms of the sample LDOS. Although there is a broad consensus regarding this interpretation of the data, a definitive assessment requires the issue of the tunneling matrix element to be resolved.

IV. CRYSTAL STRUCTURE AND SURFACE CHARACTERIZATION

The superconducting gap of standard isotropic BCS superconductors is independent of position in real space and on momentum along the Fermi surface in k space (s-wave gap symmetry). Therefore, the tunneling spectra of a homogeneous sample depend neither on the tunneling direction, nor on the position along the surface, nor on the chosen surface. Under those circumstances the measured gap does not depend upon the above-mentioned experimental configuration, allowing for an unambiguous interpretation of tunneling experiments. The situation is very different in layered HTS cuprates, owing to their very anisotropic structural, electronic, and superconducting properties.

The HTS cuprates consist of one or more superconducting copper oxide (CuO_2) sheets sandwiched between nonmetallic charge reservoir layers [Figs. 5(a) and 5(b)]. Because of the alternate stacking of superconducting and nonsuperconducting layers along the crystallographic [001] direction, tunneling spectra of (001) surfaces are likely to depend on the termination layer. As a result of the d-wave symmetry [Fig. 5(c)] of the superconducting gap, the spectra may also strongly depend on which momentum states contribute to the tunneling current (see Sec. III.D.2). Finally, the sign change of the d-wave gap function at the nodal points along (π,π) induces quasiparticle bound states at surfaces or step edges oriented perpendicular to the nodal directions. The spectroscopic signature of these bound states is an

enhanced conductance—the so-called zero-bias conductance peak—instead of a gap at E_F (Kashiwaya and Tanaka, 2000). For all these reasons, tunneling spectra measured on HTS's are likely to depend on the exposed surface layer, its orientation, and the details of the tunneling matrix element. Hence, a range of different tunneling spectra is expected, even for perfect vacuum tunnel junctions, making their interpretation very challenging.

On layered HTS's, such as $Bi_2Sr_2CaCu_2O_{8+\delta}$, a further key issue is to identify which states are being probed by STM. Does the tunneling current involve pure BiO- or CuO_2-derived states or some hybridized ones? This question, which we already touched upon in Sec. III, is of fundamental importance. Superconductivity is believed to reside in the CuO_2 plane, but most tunneling measurements of the superconducting d-wave gap were obtained on the BiO surface. Ascribing the measured gap to the superconducting state of HTS's implies that tunneling into the BiO surface allows measurement of the superconducting gap of the CuO_2 layer situated several angstroms beneath the surface. This statement is far from obvious because of the short coherence length in HTS's and nonmetallic layers sandwiching the superconducting CuO_2 sheets. The possibility of sensing electronic contributions from subsurface atomic layers is well known in highly ordered pyrolytic graphite, a very simple layered conductor. STM images of this material reveal two nonequivalent carbon sites instead of a regular honeycomb lattice (Wiesendanger and Anselmetti, 1992), due to site-dependent hybridization of carbon orbitals from the neighboring graphene sheet.

A careful assessment of the probed surface and of the tunnel junction is prerequisite to lift the above ambiguities and enable a meaningful interpretation of tunneling spectra measured on HTS's. Identification of the local surface layer is best done through atomic-scale imaging. However, such optimal resolution remains elusive on most HTS cuprates, and in Secs. IV.A and IV.B we restrict the discussion to the archetypical Bi and Y compounds, respectively. The quality of the tunnel junction can be inferred from the reproducibility of the spectra as a function of position along the surface and as a function of tip-to-sample distance as discussed in Sec. IV.C.

A. Surfaces of Bi-based cuprates

$Bi_2Sr_2CaCu_2O_{8+\delta}$ (Bi2212) is the most widely studied HTS using STM for a simple reason: it is straightforward to prepare atomically flat and clean surfaces by cleaving. Cleaving is most likely to occur between the weakly van der Waals–coupled adjacent BiO layers [Fig. 5(a)], and, with few exceptions, STM studies have focused on BiO-terminated surfaces. It was the first surface of any HTS to yield STM images with atomic-scale topographic resolution. Following the pioneering work by Kirk *et al.* (1988), the resolution steadily improved to reveal the tetragonal unit cell and the $\sim 5b$ incommensurate supermodulation along $[\bar{1}10]$ with stunning sharpness.
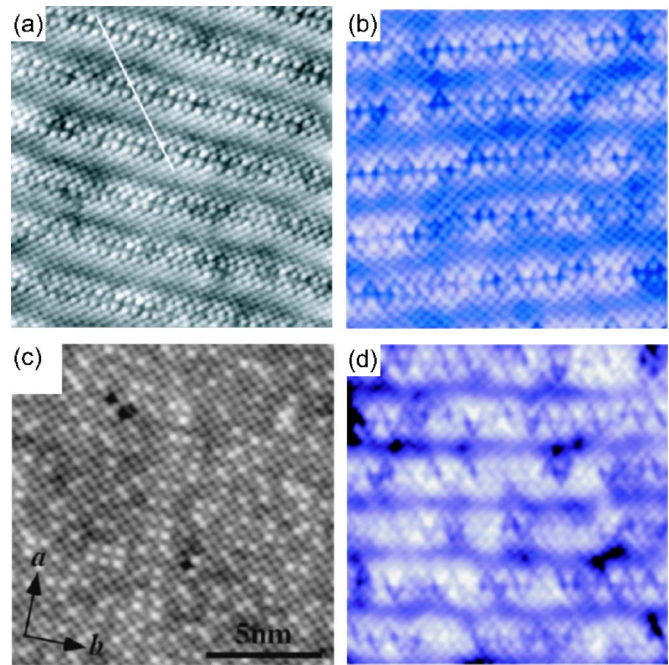

FIG. 6. (Color online) STM images of the BiO surface of Bi-based HTS cuprates. (a) 13.1×13.1 nm^2 area of $Bi_2Sr_2CuO_6$ at 4.6 K (Shan *et al.*, 2003). (b) 15×15 nm^2 area of $Bi_2Sr_2CaCu_2O_8$ at 4.2 K (Pan *et al.*, 2001). (c) Lead-doped $Bi_2Sr_2CaCu_2O_8$ at 4.3 K (Kinoda *et al.*, 2003). The bright lattice sites correspond to lead dopant atoms. Note the absence of supermodulation and dark-atom rows. (d) 15×15 nm^2 area of zinc-doped $Bi_2Sr_2CaCu_2O_8$ at 4.3 K (Pan, Hudson, Lang, *et al.*, 2000).

Cleaving predominantly exposes the BiO layer to the surface. However, other surface terminations have occasionally been observed by STM (Murakami and Aoki, 1995; Pan, Hudson, Ma, and Davis, 1998; Misra *et al.*, 2002a). In the following sections, we discuss STM investigations of the BiO and CuO_2 surfaces in greater detail.

1. BiO surface

The structural characteristics of the BiO surface, as seen by STM, are similar in all parent Bi-based HTS cuprates [Figs. 6(a) and 6(b)]. Distinctive features include nearly commensurate supermodulation along $[\bar{1}10]$ and concomitant dark-atom rows running along the supermodulation ridges. Supermodulation develops throughout bulk BiO layers, and is not a surface effect (Heinrich *et al.*, 1994; Gladyshevskii and Flükiger, 1996). Note that the supermodulation along $[\bar{1}10]$ in Bi2212 is mostly structural. No associated spatial variation of the superconducting gap amplitude has been reported. The dark-atom rows are observed on all pure BiO surfaces except in few instances on Bi2201 (Inoue *et al.*, 1995) and Bi2212 (Shin *et al.*, 1991).

The origin of supermodulation and dark-atom rows is still a matter of debate. Initially interpreted as rows of missing atoms (Kirk *et al.*, 1988), the latter were recently found to be more consistent with depressed rather than

vacant lattice sites. Inoue *et al.* (1994) attributed them to spatial ordering of nonequivalent Bi atoms, whereas Zandbergen *et al.* (1998) ascribed them to extra oxygen in the BiO layers. Supermodulation could result from a structural mismatch among the constituent layers of Bi2212. Based on x-ray refinement, Gladyshevskii *et al.* (2004) proposed an alternative model where it stems from a rotation of the Bi-O trimer in the BiO plane. In this scenario, dark-atom rows reflect additional oxygen atoms necessary to register this rotation to the BiO lattice. Gladyshevskii *et al.* further observed that this additional oxygen site is quenched in lead-doped Bi2212, suppressing both supermodulation and dark-atom rows, consistent with STM topographs of lead-doped Bi2212 [Fig. 6(c)].

The BiO layers contain two atomic species, but atomic-scale STM images reveal only one lattice site. Shih *et al.* (1991) found no dependence on bias polarity or amplitude as would be expected if the BiO layer were an ionic insulator, suggesting that a single atomic species is contributing to the contrast. Strong indications that STM is imaging the Bi lattice come from studies of Pb- (Kinoda *et al.*, 2003), Zn- (Pan, Hudson, Lang, *et al.*, 2000), and Ni- (Hudson *et al.*, 2001) substituted single crystals. In the case of lead doping, images of the BiO surface reveal some brighter lattice sites due to the dopant atoms [Fig. 6(c)]. Lead substitutes for bismuth in the BiO layer; hence the STM imaging contrast shows the bismuth lattice. Zinc and nickel substitute for copper in the CuO_2 layer. Unlike lead dopant atoms, the latter are not directly resolved in topographic images [Fig. 6(d)]. However, they are clearly seen at the bismuth lattice sites in spectroscopic images of the surface (i.e., spatially resolved maps of the local tunneling conductance; see Figs. 18 and 19). Since bismuth and copper lattices are aligned along the [001] direction, the implication is again that STM topographs of the BiO surface do reveal the bismuth lattice. Moreover, the latter results show that tunneling into the BiO surface probes the underlying CuO_2 plane, supporting the idea that the superconducting gap of the CuO_2 layer can be measured by tunneling into the BiO surface.

2. CuO_2 surface

The most comprehensive topographic and spectroscopic STM study of the CuO_2 surface to date was carried out by Misra *et al.* (2002a) on Bi2212 thin films. They clearly resolved the tetragonal lattice of the CuO_2 and BiO (001) surfaces (Fig. 7). Both layers host a supermodulation of similar periodicity with one characteristic difference: the in-plane concomitant lattice modulation is much weaker in CuO_2 layers than in BiO layers (Gladyshevskii and Flükiger, 1996). While the tunneling spectra of the BiO surface were consistent with a *d*-wave superconducting gap [Fig. 7(c)], CuO_2-terminated surfaces showed a wider gap (60 ± 10 meV) with a strongly suppressed conductance near the Fermi energy [Fig. 7(d)]. This U-shaped energy dependence of the CuO_2 tunneling conductance close to E_F [Fig. 7(d)] is unex-
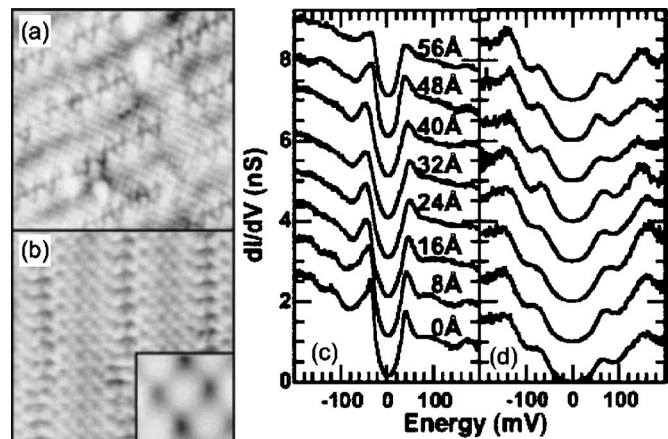

FIG. 7. STM topography and spectroscopy of a cleaved $Bi_2Sr_2CaCu_2O_8$ thin film. (a) 10×10 nm^2 topographic image of a BiO-terminated surface. (b) 6.4×6.4 nm^2 topographic image of a CuO_2-terminated surface (inset 0.8×0.8 nm^2). Tunneling spectra taken at the indicated distances along a straight line (c) on the BiO plane and (d) on the CuO_2 plane. Spectra are offset for clarity, and all data were taken with $V = 200$ mV and $I = 200$ pA. From Misra *et al.*, 2002a.

pected for a *d*-wave superconductor, raising the question of the electronic nature of a bare CuO_2 layer. Kitazawa *et al.* (1996) already noted the tendency of CuO_2 surfaces to yield spectra with a U-shaped energy dependence at low bias (expected for a *s*-wave BCS gap), whereas other surface terminations of HTS cuprates show a V-shaped energy dependence near E_F (expected for a *d*-wave BCS gap).

The electronic structure of the BiO layer is likely to be the same at the surface and in the bulk, because cleaving between adjacent BiO layers does not break any strong bond. Exposing the CuO_2 layer to the surface is significantly more disruptive; hence its structural and electronic properties may be very different from those of the bulk. Misra *et al.* (2002a) ruled out any surface reconstruction to explain the non-*d*-wave CuO_2 spectra, because the measured surface structure [Fig. 7(b)] matches the bulk structure (Heinrich *et al.*, 1994; Gladyshevskii and Flükiger, 1996). The large gap revealed by spectroscopy may signal an insulating CuO_2 surface. But Mirsa *et al.* contend it would have to be a very homogeneous insulator, with an electron-hole-symmetric low-energy DOS and E_F lying exactly halfway between the empty and filled bands [Fig. 7(d)].

Misra *et al.* (2002a) argued that the *s*-wave-looking spectra they measured are consistent with *d*-wave superconductivity in CuO_2 planes, provided the tunneling matrix element is of the anisotropic form $|M_k|^2 \propto (\cos k_x a_0 - \cos k_y b_0)^2$ (see Sec. III.D.2). This particular choice of M_k enables them to reproduce the gap structure and conductance peaks below ± 100 meV. Their fit yields a gap amplitude consistent with a reduced doping, possibly due to oxygen loss and asymmetric doping by the BiO layer underneath: 60 meV is indeed close to the gap measured in highly underdoped, yet superconducting,
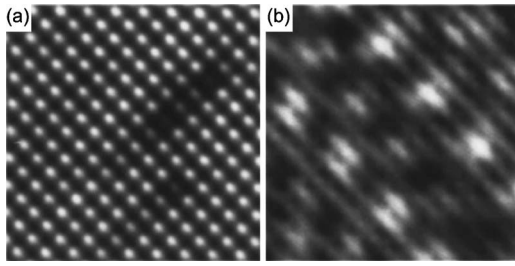
FIG. 8. 5×5 nm^2 STM images of the (a) BaO and (b) CuO chain surfaces of Y123. From Pan *et al.*, 1999.

samples (Zasadzinski *et al.*, 2001). The analysis by Misra *et al.* implies that the bare CuO$_2$ layer at the surface is superconducting, which is an important finding. However, their model only partially reproduces the experimental spectra of CuO$_2$. In particular, it does not account for higher-energy peak structures and does not exclude the possibility that the CuO$_2$ spectra reflect some signature of the pseudogap (Sec. VI). Finally, these authors do not answer the question as to why the M_k of BiO and CuO$_2$ surfaces would be so different, leaving the nature of the CuO$_2$ surface open to further investigations.

B. Surfaces of YBa$_2$Cu$_3$O$_7$

YBa$_2$Cu$_3$O$_7$ (Y123) is the second most studied HTS by STM. Y123 is much less anisotropic than Bi2212 and offers no natural cleaving plane. STM experiments were carried out on as-grown and chemically etched surfaces, as well as on single crystals cleaved at low temperature ($\sim$20 K). Y123 cleaves between BaO and CuO chain layers, and both were imaged with atomic-resolution STM on low-temperature cleaved samples (Edwards *et al.*, 1994; Pan *et al.*, 1999). The problem with cleaved specimens is that STM (Edwards *et al.*, 1992) and ARPES (Campuzano *et al.*, 1990) results degrade if the surfaces are not kept below 70 K, indicating that they are unstable and possibly different from the bulk due to mechanical strain and unbalanced charges.

On the other hand, reproducible temperature-dependent STM spectroscopy was demonstrated on as-grown surfaces of single crystals grown in BaZrO$_3$ crucibles (Maggio-Aprile *et al.*, 2000). These surfaces could sustain repeated thermal cycling between 4 and 300 K. They also allowed the first successful imaging of the Abrikosov vortex lattice in a HTS (Maggio-Aprile *et al.*, 1995). Similar results have been achieved on chemically etched surfaces (Wei, Yeh, *et al.*, 1998; Shibata *et al.*, 2003b). Atomic resolution on as-grown Y123 surfaces appears very difficult to achieve and has been reported only on thin films (Lang *et al.*, 1991; Nantoh *et al.*, 1995). A reliable recipe allowing both atomic-resolution imaging and reproducible spectroscopy over a wide temperature range on Y123 has yet to be found.

The orthorhombic lattice of BaO-terminated low-temperature cleaved surfaces has been clearly resolved by STM [Fig. 8(a)], with a few single-atomic defects at-

tributed to oxygen vacancies (Pan *et al.*, 1999). Similar micrographs were obtained by Edwards *et al.* (1994) who found them to be independent of bias amplitude and polarity, although a systematic energy dependence is not available yet.

CuO-chain-terminated surfaces have been investigated in greater detail. They show a more complex structure with a large charge modulation superimposed on the atomic lattice [Fig. 8(b)]. The copper and oxygen lattices are resolved as oval and faint round features, respectively. In contrast to BaO, STM images of the CuO-chain surface do depend on energy and bias polarity, which led Edwards *et al.* (1994, 1995) to attribute the spatial modulation of the DOS to a charge density wave (CDW). More recently, Derro *et al.* (2002) identified a series of strong dispersive resonances at energies below the superconducting gap $\Delta_p = 25$ meV. In their view, these resonances are hallmarks of a predominantly 1D character of the CuO-chain layer DOS and the charge modulation observed in the topography is more consistent with superconducting quasiparticle scattering than with a CDW. In this scenario, the CuO chains would be superconducting via proximity coupling to the CuO$_2$ planes. Note that the presence of these two superconducting layers could provide an explanation of the multiple-peak structure in Y123 tunneling spectra discussed in Sec. V.A.2.

C. Tip-to-sample distance dependence

The tip-to-sample distance dependence of the tunneling spectra is a key experimental test to appraise the quality of the STM vacuum tunnel junction. If only the states from a single surface layer were contributing to the tunneling process, the spectra should be independent of tip-to-sample distance. On the other hand, if the junction is contaminated or if different decoupled layers were contributing to the tunneling process, one might expect some tip-to-sample distance dependence.

Large tip-to-sample distance dependencies of c-axis imaging and spectroscopy were common features of early STM experiments on HTS cuprates. Only low-resistance tunnel junctions ($R_t \sim$ MΩ), i.e., when the tip is in very close proximity to the surface, allowed measurement of the superconducting gap features on Bi2212 and Y123 (Hasegawa, Nantoh, and Kitazawa, 1991; Hasegawa *et al.*, 1992; Nantoh, Hasegawa, Yamaguchi, *et al.* 1994; Aleszkiewicz *et al.*, 1997). Upon increasing the junction resistance ($R_t \sim$ GΩ) by pulling the tip away from the surface, these superconducting features vanished and the tunneling spectra evolved into semiconductinglike line shapes. Likewise, some groups claimed that topographic imaging of Bi2212 depended on the tip-to-sample distance (Nishiyama, 1996; Oda *et al.*, 1996) the BiO layer being imaged at large and the CuO$_2$ layer at small tip-to-sample distance. More recently, Sugita *et al.* (2000) reported exactly the opposite distance dependence in experiments where the topographic contrast was seen to switch randomly between BiO and CuO$_2$.
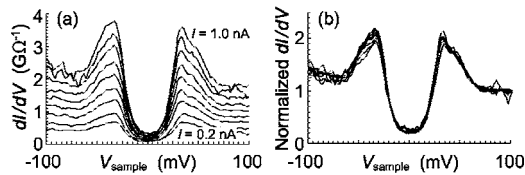
FIG. 9. Ideal STM vacuum tunnel junction between a Au tip and Bi2212 at 4.2 K. (a) Tunneling spectra measured as a function of increasing tip-to-sample distance. The current is changed from $I=1.0$ (short distance, top curve) to 0.2 nA (large distance, bottom curve) in 0.1-nA increments at constant sample voltage $V=0.4$ V. (b) Same data plotted on a normalized conductance scale to emphasize the distance independence. Adapted from Renner and Fischer, 1995.

A better control over tunnel junctions became possible through progress in HTS single-crystal growth and STM instrumentation, and the above distance dependences have not been confirmed on ideal junctions. As shown in Fig. 9, these improvements enabled tip-to-sample distance-independent STM tunneling spectroscopy on Bi2212 (Renner and Fischer, 1994a, 1995) and Y123 (Maggio-Aprille, 1996). Recently, Sakata *et al.* (2003) confirmed this distance independence in the entire range from vacuum tunneling to point contact on Bi2212. The only minute change Sakata *et al.* found was a slight reduction in the gap amplitude at very short electrode spacing, which might result from a change in the local DOS due to the pressure applied by the STM tip.

The best tunnel junctions are not only characterized by tip-to-sample distance-independent STM imaging and spectroscopy; they also yield the largest work function[9] ($\phi > 1$ eV) and tunneling spectra with the sharpest superconducting DOS structures. On Bi2212, two other distinctive spectral features enable ready identification of the best junctions. (i) The background conductance is flat or even slightly decreasing at energies $eV < 500$ meV [see Renner and Fischer (1995), and references therein]. (ii) The conductance peaks at the gap edges are most intense and sharp in spectra with a flat background conductance below ± 500 meV. Smeared coherence peaks and a parabolic background conductance both signal a contaminated tunnel junction. Indeed, the energy dependence of the tunneling probability expected in low-work-function tunnel junctions leads to a background conductance increasing with energy, and quasiparticle scattering causes damping of the coherence peaks.

The degree of quasiparticle scattering and the energy dependence of the background conductance are prone to vary, depending on the quality of the local tunnel junction. As a result, the surface will appear very nonuniform from a spectroscopic point of view, with dI/dV spectra varying from parabolic curves with only a weak

or no gap structure in degraded surface areas to flat characteristics with a very sharp gap structure in clean surface areas. Such inhomogeneities were first observed by Wolf *et al.* (1994) in spatially resolved tunneling spectroscopy of Bi2212. They are strictly related to the (poor) quality of the surface, and are to be clearly distinguished from the inhomogeneities discussed in Secs. V.D and VIII.

D. Summary

The early days of STM spectroscopy on HTS cuprates were plagued by a very wide spread in tunneling line shapes, as pointed out by Kitazawa *et al.* (1996). Under those circumstances, it was extremely challenging to delineate the intrinsic features of the measured local DOS. It appears now that much of the spread in experimental data was a consequence of ill-defined tunnel junctions and sample surfaces. Atomic-resolution STM imaging, although not sufficient to ensure true vacuum tunneling spectroscopy as shown by Renner and Fischer (1995), plays an important part in assessing the surface. The more stringent tests of the junction quality are a reasonably large work function ($\phi \gtrsim 1$ eV) and tunneling spectra that are independent of tip-to-sample distance.

V. LOW-TEMPERATURE TUNNELING SPECTROSCOPY

Since the pioneering experiments of Giaever (1960), electron tunneling spectroscopy has become the technique of choice to probe the superconducting quasiparticle density of states. It is probably the most successful and sensitive way to measure the gap in the electronic excitation spectrum at the Fermi energy, one of the hallmarks of superconductivity [see textbooks by Wolf (1985) and Tinkham (1996)]. Tunneling spectroscopy was instrumental in validating the BCS theory for conventional low-T_c superconductors. Naturally, when superconductivity was discovered at unprecedented high temperatures in copper-oxide perovskites (Bednoz and Müller, 1986), there were great expectations that tunneling experiments would unravel the underlying physics.

The focus of this section is on low-temperature tunneling spectroscopy of HTS cuprates performed by STM in zero external magnetic field. We shall review the differential tunneling conductance spectra dI/dV measured on selected HTS, with the aim of identifying generic features in the electronic DOS related to their superconducting properties. We discuss in particular the gap structure at the Fermi energy, the background conductance, the dip-hump feature above the gap, the zero-bias conductance peak (ZBCP) at the Fermi energy, and the doping dependence and spatial (in)homogeneity of the tunneling spectra.

The overwhelming majority of experiments probe (001) surfaces with the STM tip perpendicular to the CuO_2 planes. Hence, we shall mostly discuss this experimental configuration. Cross-sectional tunneling, i.e., tun-

---

[9]The work function can be estimated from the distance dependence of the tunneling current (Pan, Hudson, and Davis, 1998).
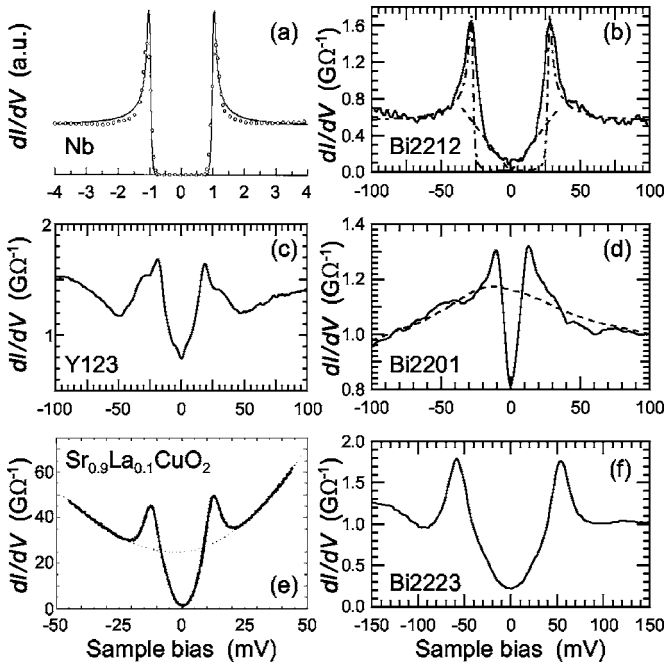
FIG. 10. *c*-axis SIN vacuum tunneling conductance spectra of selected superconductors (single crystals) measured by STM. (a) Nb at 335 mK (circles), BCS fit with $\Delta=1.0$ meV (solid line). From Pan, Hudson, and Davis, 1998. (b) Optimally doped Bi2212 ($T_c=92$ K) at 4.8 K (solid line), *s*-wave BCS fit with $\Delta=27.5$ meV and pair-breaking parameter $\Gamma=0.7$ meV (dash-dotted line), and low-energy V-shaped *d*-wave BCS conductance (dashed line). From Renner and Fischer, 1995. (c) Y123 at 4.2 K. From Maggio-Aprile *et al.*, 1995. (d) Overdoped Bi2201 ($T_c=10$ K) at 2.5 K (solid line) and 82 K (dashed line). Adapted from Kugler *et al.*, 2001. (e) Optimally doped $Sr_{0.9}La_{0.1}CuO_2$ at 4.2 K. Adapted from Yeh *et al.*, 2003. (f) Underdoped Bi2223 ($T_c=111$ K) at 4.2 K. From Kugler *et al.*, 2006.

neling into ($hk0$) surfaces with the STM tip parallel to the CuO_2 planes, is briefly discussed in Sec. V.F.

A. Gap spectroscopy

A series of typical SIN tunneling characteristics measured by STM on selected superconductors at low temperature is presented in Fig. 10. Niobium [Fig. 10(a)] exhibits all the classic features expected for a conventional low-T_c BCS superconductor: (i) a completely developed gap centered on E_F ($\Delta=1.0$ meV) characterized by a U-shaped dI/dV with zero conductivity at E_F and (ii) two symmetric square root singularities at the gap edges. Such spectra are fully described by the BCS theory (Tinkham, 1996). In contrast, tunneling spectra of HTS cuprates deviate in a number of ways from BCS predictions, as described in the following sections.

1. Bi compounds

A characteristic dI/dV spectrum measured on a cleaved Bi2212 single crystal is shown in Fig. 10(b) (Renner and Fischer, 1994a, 1995; DeWilde *et al.*, 1998; Pan *et*

al., 2001). Spectra with similar line shapes were obtained on Bi2223 [Fig. 10(f), Kugler *et al.*, 2006] and Hg-based cuprates (Rossel *et al.*, 1994; Wei, Tsuei, *et al.*, 1998), though the latter exhibit a different (increasing) energy dependence of the background conductance. The prominent low-energy features of the Bi2212 spectra are two large conductance peaks defining a clear gap centered on E_F and a conductance increasing linearly with energy near E_F. For convenience, the superconducting gap is often defined as half the energy separating the two conductance peaks (Δ_p). The gap obtained in this way is somewhat larger than the value Δ calculated from a proper fit of the spectra (Hoogenboom, Berthod, *et al.*, 2003). In HTS's, the reduced gap defined as $2\Delta_p/k_BT_c$ is far in excess of 3.5 or 4.3, the values expected for a weak-coupling *s*-wave or *d*-wave BCS superconductor, respectively (Won and Maki, 1994).

Two of the most striking features of the dI/dV spectra of Bi2212 are the V-shaped energy dependence near E_F and the very large peaks at the gap edges. The V-shaped low-bias conductance [Fig. 10(b)] is indicative of nodes in the gap. This is consistent with the *d*-wave symmetry deduced from tricrystal experiments (Tsuei and Kirtley, 2000) and with the angular dependence observed in ARPES measurements (Damascelli *et al.*, 2003; Campuzano *et al.*, 2004). However, this simple model fails to reproduce the large spectral weight in the conductance peaks at the gap edges. Wei, Tsuei, *et al.* (1998) and Hoogenboom, Berthod, *et al.* (2003) showed that both characteristics can be simulated simultaneously by taking into account the band structure, and especially the van Hove singularity (VHS) at the saddle points at $(\pi,0)$ and $(0,\pi)$ in the Brillouin zone (see Sec. V.B).

The simulated spectral weight in the peaks could also be enhanced by assuming an anisotropic tunneling matrix element, which would filter the tunneling probability in favor of antinodal states at $(\pi,0)$ and suppress the tunneling probability near nodal states along (π,π) (Yusof *et al.*, 1988; Franz and Tešanović, 1999). However, this simple model not only enhances the DOS in the coherence peaks in agreement with experiment; it also reduces the DOS below the gap too much, producing more *s*-wave-looking U-shaped spectra inconsistent with experiments (Hoogenboom, Berthod, *et al.*, 2003).

The tunneling spectra of the three-layer Bi compound $Bi_2Sr_2Ca_2Cu_3O_{10+\delta}$ (Bi2223) look very similar to those of Bi2212, except that all features are shifted to higher energies [Fig. 10(f)]. On the contrary, the single-layer Bi compound $Bi_2Sr_2CuO_6$ (Bi2201) yields substantially different spectra [Fig. 10(d)] with a finite zero-bias conductance and a much larger reduced gap, e.g., $2\Delta_p/k_BT_c \sim 28$ in overdoped Bi2201 (Kugler *et al.*, 2001). Mashima *et al.* (2003) measured similar looking spectra on lead-doped Bi2201. The considerable difference between Bi2201 and Bi2212 may stem from the more pronounced two-dimensional nature of Bi2201. Superconductivity in Bi2201 resides in a single CuO_2 layer, resulting in larger fluctuations effectively reducing T_c. The much wider temperature range of the pseudogap phase in Bi2201
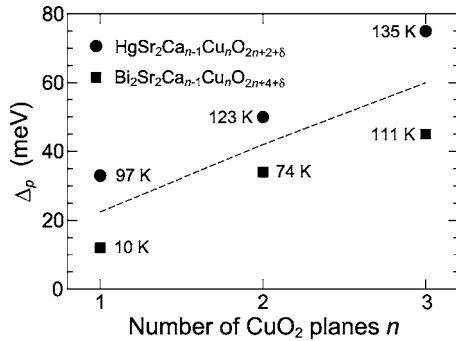
FIG. 11. Gap amplitude Δ_p as a function of the number n of CuO_2 planes in the bismuth and mercury series. Optimally doped $HgSr_2Ca_{n-1}Cu_nO_{2n+2+\delta}$ (circles), gap values from Wei, Tsuei, *et al.* (1998). Slightly overdoped $Bi_2Sr_2Ca_{n-1}Cu_nO_{2n+4+\delta}$ (squares), gap values for $n=1$ from Kugler *et al.* (2001), for $n=2$ from Renner, Revaz, Genoud, *et al.* (1998), and for $n=3$ from Kugler *et al.* (2006). Each compound's T_c is indicated next to the symbol. The dashed line is a guide to the eye.

(see Sec. VI) could be a direct consequence of such fluctuations. The finite zero-bias conductance and broad peaks at the gap edges remain open issues.

The gap amplitude of hole-doped HTS cuprates series appears to increase with the number n of CuO_2 planes per unit cell, at least up to $n=3$ for which tunneling data exist. This dependence is depicted in Fig. 11 for two series with very different gap amplitudes: the bismuth series $Bi_2Sr_2Ca_{n-1}Cu_nO_{2n+4+\delta}$ and the mercury series $HgSr_2Ca_{n-1}Cu_nO_{2n+2+\delta}$. The increase of the gap with n in the Bi compounds is illustrated graphically in Figs. 10(d), 10(b), and 10(f) showing the tunneling spectra for $n=1$, 2, and 3, respectively. (Note that the dependence on n appears accentuated in Fig. 10 due to the spread of doping levels of that Bi series.) A similar behavior is observed for T_c^{max}: it increases with increasing n up to $n=3$ (T_c^{max} decreases upon further increasing n) and can be very different in distinct homogeneous series. Understanding the dependence of the gap and of T_c^{max} on the number of CuO_2 planes may turn out to be one important key to unravel the mechanism of HTS's [see, e.g., Pavarini *et al.* (2001); Chen and Lin (2004)].

2. Y compounds

A characteristic SIN dI/dV spectrum measured on an as-grown, fully oxygenated $YBa_2Cu_3O_7$ (Y123) single crystal ($T_c=91$ K) is shown in Fig. 10(c). The spectrum reveals a number of remarkable differences compared to Bi2212 with similar T_c: (i) a smaller reduced gap (~4.9 in the sample shown here), (ii) a large finite conductance at $V=0$, and (iii) multiple broad coherence peaks at the gap edges (Miller *et al.*, 1993; Maggio-Aprile *et al.*, 1995). The main coherence peaks define a gap of ~20 ± 2 meV, much closer to the value expected for a BCS d-wave superconductor than the gap in the Bi-based cuprates discussed above. Additional structures of interest are weak shoulders flanking the main peaks at higher en-

ergy, and two weak features often developing below the gap at about ±6 meV.

The multiple-peak structure does not correspond to the simple d-wave expectation. Tachiki *et al.* (1990) and Miller *et al.* (1993) ascribed the features inside the gap near ±6 meV to weak proximity-induced superconductivity in the BaO and CuO-chain planes. Yeh *et al.* (2001) identified peaks at ±20 and ±6 meV with a mixed $(d_{x^2-y^2}+s)$-wave gap in the CuO_2 plane. In this scenario, two sets of conductance peaks are indeed expected, one at $\pm(\Delta_d-\Delta_s)$ and the other at $\pm(\Delta_d+\Delta_s)$, with Δ_d and Δ_s the maximum amplitude of the d-wave and s-wave components of the gap, respectively. However, this would imply a strong s-wave admixture in the Y123 ground state, which is opposed by other experiments, like tricrystal experiments (Tsuei and Kirtley, 2000), showing a pure d wave. Thus the exact nature of the Y123 ground state and the corresponding interpretation of the tunneling data need further investigation.

Different ideas have been developed to understand the shoulders outside the main coherence peaks. Such structures have been modeled in terms of the band structure van Hove singularity (Tachiki *et al.*, 1990; Hoogenboom, Berthod, *et al.*, 2003). Similar, though much weaker, shoulders have been measured on Bi2212 and were ascribed to the onset of a strong-coupling effect (Zasadzinski *et al.*, 2003). One aspect of Y123, which certainly complicates the analysis of the spectra, is the presence of CuO chains along with the CuO_2 planes, and a completely satisfactory description has yet to be devised.

Spectra with a line shape similar to those obtained on Y123 were measured on $La_{1.84}Sr_{0.16}CuO_4$ (LSCO) by Kato *et al.* (2003). Like Y123, their background conductance increases with energy, the DOS at E_F does not vanish, and the reduced gap amounts to ~4.8. However, unlike Y123, they do not show any multiple-peak structure.

3. Electron-doped HTS's

Over the past two decades, some consensus has emerged that the gap symmetry in hole-doped HTS's is $d_{x^2-y^2}$. In electron-doped HTS's, a majority of tunneling experiments point at a more conventional s-wave gap, although some do look more consistent with a d-wave symmetry. This controversy in electron-doped HTS's is illustrated in $Nd_{1.85}Ce_{0.15}CuO_{4-y}$ (NCCO), one of the few electron-doped HTS's that has been investigated by STM. Alff *et al.* (1998) and Kashiwaya *et al.* (1998) contend that NCCO is an s-wave superconductor. Their conclusion is based on the absence of a zero-bias conductance peak on surfaces perpendicular to the nodal lines (see Sec. V.F) and on the good fit of the spectra obtained with an anisotropic s-wave BCS model. A different picture emerges from STM studies by Hayashi, Isoshima, *et al.* (1998), who concluded that NCCO is a d-wave superconductor based on the ZBCP that appears in some of their low-resistance tunnel junction spectra.
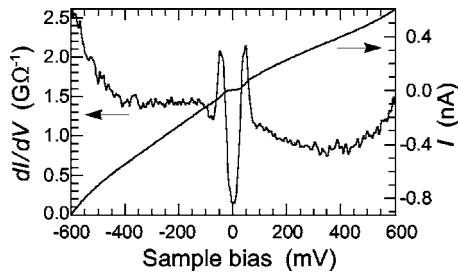
FIG. 12. Large-energy-scale SIN tunneling characteristics of Bi2212 (Renner and Fischer, 1993).

Magnetic and nonmagnetic impurities provide an indirect probe of the gap symmetry (see Sec. V.E). Nonmagnetic impurity scattering has no effect on an *s*-wave superconductor, whereas it will cause pair breaking in a *d*-wave superconductor. Magnetic impurities have the opposite effect and do cause pair breaking in conventional *s*-wave BCS superconductors. The gap measured on $Sr_{0.9}La_{0.1}CuO_2$ [SLCO, Fig. 10(e)], an infinite-layer electron-doped HTS, is in good agreement with an isotropic *s*-wave BCS model (Yeh *et al.* 2002). Yeh *et al.* reported that doping SLCO with nickel, a magnetic impurity, has a large effect on the line shape of the LSCO spectra, whereas doping with Zn, a nonmagnetic impurity, has very little effect as expected for an *s*-wave superconductor. In Bi2212, a *d*-wave hole-doped HTS, the opposite seems to happen, where zinc doping is most detrimental to superconductivity (Hudson *et al.*, 2001)—note that in both compounds the impurity atom is substituting for the copper atom in the CuO_2 plane. Such studies of atomic-scale impurities in HTS's are discussed further in Sec. V.E.

B. Dip-hump structure

Section V.A was devoted to the region of the tunneling conductance curves below the superconducting gap. Here we extend the discussion to include the conductance background at higher energy beyond the gap. Figure 12 shows a typical large-energy-range spectrum of Bi2212 exhibiting a sizable electron-hole asymmetry in the background conductance (see also Sugita *et al.*, 2000). A very similar background was measured on Bi2223 (Kugler *et al.*, 2006). The increasing conductance at high energy beyond 400 meV may be a signature of the valence bands below E_F.

A remarkable dip structure develops outside the superconducting gap on top of a smooth broad maximum in the background conductance near E_F. In early STM experiments, this dip was mostly obscured by an increasing (linear or parabolic) background conductance [see, e.g., Liu *et al.* (1994)]. The dip became clearly apparent in spectra obtained with the best STM junctions, as defined in Sec. IV.C. In Bi2212, the dip is systematically seen at negative sample bias (Renner and Fischer, 1994a, 1995). A symmetric dip is present at positive bias in some exceptional cases (DeWilde *et al.*, 1998; Hudson *et al.*, 1999). The dip structure, often accompanied by a

hump at higher energy, is at the core of a heated debate. One key question is whether it is a band-structure or a strong-coupling effect.

Band-structure effects would be a natural possibility to explain the dip. ARPES spectra, which first showed the same dip feature beyond the gap (Dessau *et al.*, 1991; Hwu *et al.*, 1991), have been interpreted along those lines. However, this interpretation is not widely accepted. Zasadzinski *et al.* (2003) excluded in particular the possibility that the dip is due to a VHS or that it results from a superconducting gap opening in a pseudogap background.

Strong-coupling effects are another possibility to explain the dip. They are known to have similar effects on tunneling spectra in conventional superconductors. Tunnel junctions on lead, for example, reveal some fine structure in the differential conductance above the gap, which was shown to correspond to peaks in the phonon density of states $F(\omega)$. The fine structure was directly linked to the electron-phonon mechanism of superconductivity, and the electron-phonon spectral function $\alpha^2 F(\omega)$ could be quantitatively obtained through inversion of the spectra using strong-coupling Eliashberg theory (Schrieffer *et al.*, 1963; McMillan and Rowell, 1965). This eventuality has been addressed by Zasadzinski *et al.* (2003) to fit a particular symmetric Bi2212 spectrum normalized to an arbitrary state-conserving normal-state background. Using a modified Eliashberg model to account for the *d*-wave symmetry, Zasadzinski *et al.* (2003) self-consistently reproduced the overall shape, position, and magnitude of the dip as well as the superconducting gap structure with a single narrow bosonic mode centered at 36.5 meV.

In the strong-coupling scenario, the dip could be due to a phonon mode (as in low-temperature superconductors) or to a collective electronic mode. A candidate electronic mode was observed by neutron scattering near (π, π) at 41 meV in Y123 (Fong *et al.*, 1995), and subsequently in Bi2212 (Fong *et al.*, 1999). This mode was determined to scale with T_c (He *et al.*, 2001), suggesting a close relation with the superconducting state. Specific models were developed to describe the coupling of electrons to this mode (Eschrig and Norman, 2000). Hoogenboom, Berthod, *et al.* (2003) used this model to calculate the spectra of Bi2212 using doping-dependent band-structure parameters from ARPES, including the bilayer splitting, and the electronic mode measured by neutrons. The result is plotted as the red curve in Fig. 13. Note the importance of the bilayer splitting to obtain the proper background conductance intensity relative to the peaks height. In this model the asymmetry of the dip with respect to E_F is not a consequence of the nature of the mode (e.g., phonon or spin wave) but is due to the presence of the VHS at negative energy.

C. Doping dependence of the superconducting gap

A generic doping phase diagram of HTS's is shown in Fig. 14. Undoped cuprates are antiferromagnetic (AF) Mott insulators with one electron per copper site in the
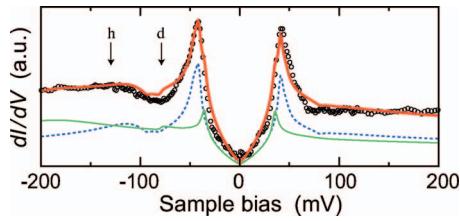
FIG. 13. (Color) Fit of the differential tunneling conductance measured on optimally doped Bi2212. The fit (red line) to be compared with the experimental data (circles) is the sum of the contributions from antibonding (dotted line) and bonding (green line) bands describing the CuO_2 bilayer splitting. Adapted from Hoogenboom, Berthod, *et al.*, 2003.

CuO$_2$ plane. Upon adding either holes or electrons, they eventually become superconducting (SC) and T_c increases to reach a maximum at optimal doping before vanishing again at higher hole or electron concentration.

A series of unusual properties characterize hole-doped cuprates, including a pseudogap, non-Fermi-liquid behavior, and an unusual superconducting state. These properties depend on doping and are most anomalous in underdoped compounds (i.e., at doping below optimal).

In conventional BCS superconductors, Δ is proportional to the superconducting transition temperature T_c and the reduced gap $2\Delta/k_B T_c$ lies in the range 3.5 to 4.3. A surprising result was that, for most HTS compounds, STM tunneling spectroscopy and related methods (planar, break, and point-contact tunnel junctions) as well as ARPES spectroscopy found a very large and doping-dependent reduced gap (Fig. 15). This result reflects the absence of scaling of the superconducting gap with T_c [Fig. 15(b)]. In overdoped Bi2212, the gap decreases with decreasing T_c, as expected. But in underdoped Bi2212, the gap increases with decreasing T_c (Renner, Revaz, Genoud, *et al.*, 1998; Miyakawa *et al.*, 1999). The
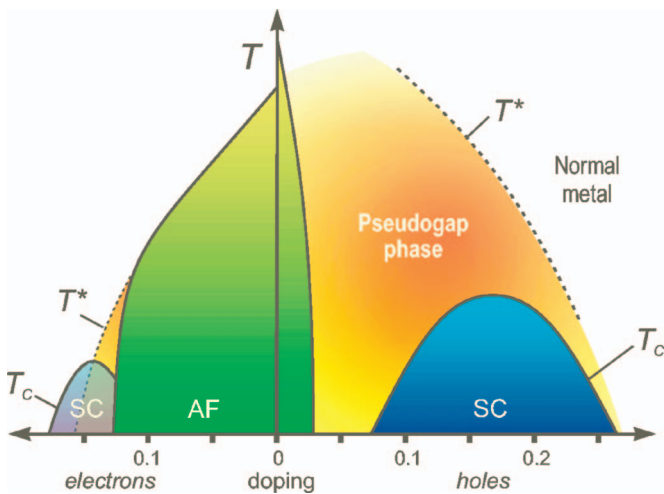

FIG. 14. (Color) Schematic doping phase diagram of electron- and hole-doped high-T_c superconductors showing, in particular, the superconducting (SC) and antiferromagnetic (AF) phases.
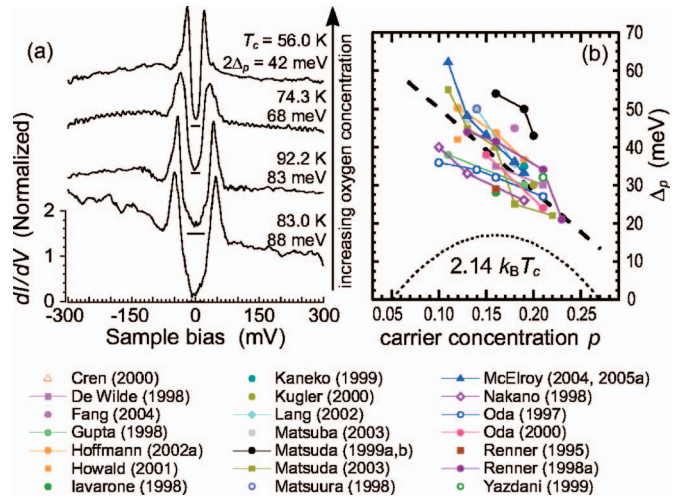

FIG. 15. (Color) Pseudogap in Bi2212. (a) Doping dependence of STM tunneling spectra measured on Bi2212 (Renner, Revaz, Genoud, *et al.*, 1998). (b) Compilation of the gap of Bi2212 measured by various techniques in a wide doping range. The numerical values are listed in Appendix B. The dashed line is a linar fit of the average gap at a given doping. Note the absence of scaling between the gap and T_c.

reduced gap defined in the standard way ranges from 4.3 to values as high as 28 (Kugler *et al.*, 2001). This wide range suggests that T_c, the temperature where phase coherence and a macroscopic superconducting state are established, is not the appropriate energy scale to describe the gap. Replacing T_c by T^*, the temperature where the pseudogap appears, enables one to recover a constant reduced gap with a more conventional value close to 4.3 (Kugler *et al.*, 2001; Dipasupil *et al.*, 2002; Nakano *et al.*, 2003) as expected for a d-wave BCS superconductor (see Sec. VI). Other spectroscopic features also show a characteristic doping dependence in Bi2212. The dip-hump feature discussed in Sec. V.B becomes weaker and shifts closer to the coherence peaks in underdoped and over-doped compounds (Zasadzinski *et al.*, 2001). The background conductance shows a systematic evolution, becoming gradually more asymmetric with decreasing hole concentration [Fig. 15(a)]. Likewise, coherence peaks are most asymmetric in highly underdoped crystals (Miyakawa *et al.*, 1999). The change in the background conductance can be partly explained in terms of the VHS shifting away from E_F in underdoped Bi2212 (Hoogenboom, Berthod, *et al.*, 2003). However, the more pronounced asymmetry observed in heavily underdoped samples has been ascribed to strong-correlation effects (Rantner and Wen, 2000; Anderson and Ong, 2006). The smeared coherence peaks at the gap edges in underdoped Bi2212 may be a consequence of the very short quasiparticle lifetime due to the proximity of a Mott insulator.

The doping dependence of the gap of Y123 is much less documented than Bi2212. Deutscher (1999) and Yeh *et al.* (2001) reported that, unlike that in Bi2212, the gap in Y123 does scale with T_c as a function of doping and the reduced gap does not reach as high values as in
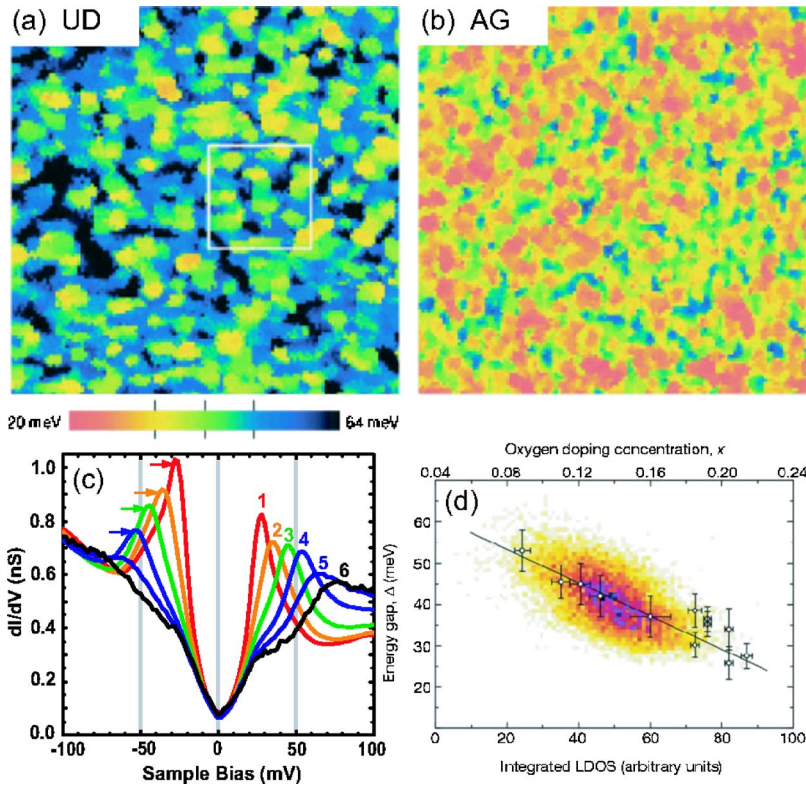
FIG. 16. (Color online) 56×56 nm^2 maps of the spatial gap distribution in (a) underdoped and (b) as-grown Bi2212 single crystals. Adapted from Lang *et al.*, 2002. (c) Range of tunneling conductance spectra measured on inhomogeneous superconducting Bi2212. From McElroy, Lee, Hoffmann, *et al.*, 2005. (d) Scatter plot of the superconducting gap versus the integrated local DOS in optimally doped Bi2212. From Pan *et al.*, 2001.

Bi2212. The term $2\Delta_p/k_B T_c$ remains much closer to the value for conventional superconductors, ranging from 7.8 (underdoped) to 4.5 (overdoped). Kohen *et al.* (2000) and Yeh *et al.* (2003) reported another interesting observation in Y123: namely, that the symmetry of the gap is changing from pure d wave to $(d+s)$ wave or s wave above optimal doping (see discussion in Sec. V.A.2). Vobornik *et al.* (1999) claimed to have observed similar crossover from a d-wave to a less anisotropic gap in overdoped Bi2212 in ARPES experiments. However, this result is in contradiction with STM spectroscopy, which shows the same linear energy dependence of the conductance near E_F throughout the entire superconducting range (Renner, Revaz, Genoud, *et al.*, 1998; Miyakawa *et al.*, 1999).

D. Spatial gap (in)homogeneity

The question of spatial homogeneity of the superconducting gap has stirred up a lot of interest. This ongoing excitement is driven by models where electronic phase separation is at the core of the high superconducting transition temperature (Phillips *et al.*, 2003). Two types of spatial inhomogeneities of the local DOS emerge from STS studies of Bi2212: (i) spatial inhomogeneity of the superconducting gap amplitude and (ii) spatial inhomogeneity of the low-energy DOS, deep inside the gap. The latter is seen as a $\sim 4a_0 \times 4a_0$ periodic electronic modulation, where a_0 is the unit-cell lattice parameter (Hoffman, Hudson, *et al.*, 2002; Howald, Eisaki, Kaneko, Greven, and Kapitulnik, 2003). Recently, a similar electronically modulated phase was also found to develop in the pseudogap state of Bi2212 above T_c (Vershinin,

Misra, Ono, *et al.*, 2004) as well as in superconducting and nonsuperconducting $Ca_{2-x}Na_xCuO_2Cl_2$ (Hanaguri *et al.*, 2004). These DOS modulations appear intimately linked to the HTS state and are the focus of Sec. VIII. Here we shall discuss the notorious spatial inhomogeneities of the gap amplitude observed in Bi2212.

Inhomogeneous superconductivity in Bi2212 was reported in a number of STM studies (Cren *et al.*, 2000; Howald *et al.*, 2001; Pan *et al.*, 2001; Lang *et al.*, 2002; Kinoda *et al.*, 2003). Real-space STS maps of the local superconducting gap shown in Figs. 16(a) and 16(b) reveal a network of nanometer-scale islands, on average 3–5 nm wide, with different gap amplitudes.[10]

The key question is to what extent this inhomogeneity is an intrinsic phenomenon at the core of high-temperature superconductivity. By intrinsic we mean an electronic effect, possibly related to the mechanism for HTS's, taking place in an otherwise homogeneous system. Electronic phase separation would be one candidate phenomenon (Phillips *et al.*, 2003). This is in contrast to an extrinsic origin of the spectral inhomogeneities, by which we mean a phenomenon unrelated to HTS's, resulting from stoichiometric inhomogeneities such as the distribution of atoms and dopants. Howald *et al.* (2001) argued strongly in favor of an intrinsic inhomogeneity. They pointed out that the boundaries between domains are always of the order of the coherence length and that there was no obvious correlation with

---

[10]Degraded or contaminated surfaces also lead to spatial variations of the tunneling spectra, but of a very different kind (see Sec. VI.B.2).

structural inhomogeneities of the sample. Their conclusion was that this disorder represents a phase separation phenomenon into "good and bad superconducting regions." Such an interpretation has also been put forward by Pan *et al.* (2001) and Lang *et al.* (2002). On the contrary, Renner and Fischer (1994b) noted the existence of such inhomogeneities and concluded that they are related to chemical inhomogeneities. They further found that homogeneous tunneling spectra can be obtained, and they demonstrated atomic resolution under these conditions (Renner and Fischer, 1995). Hoogenboom, Kadowaki, *et al.* (2003) showed that homogeneous samples could be obtained by adequate annealing, at least in the overdoped case. They concluded that inhomogeneity is most likely due to inhomogeneous oxygen distribution and that it is not an essential part of the mechanism for HTS's. Thus, in recent years, there has been a controversy about the interpretation of these inhomogeneities. Although this question is not definitively settled, we are of the opinion that there is more experimental evidence for the extrinsic scenario. In the following, we shall develop further arguments on which this statement is based.

The first piece of evidence comes from a series of experiments showing reproducible spectra with little spread in gap amplitude in Bi2212, Bi2223, Y123 [Figs. 17(b)–17(d)], and $NdBa_2Cu_3O_{7-\delta}$ (Nishiyama *et al.*, 2002) single crystals. These measurements were made in conditions where concurrent atomic resolution and/or STS vortex-core imaging could be achieved, indicating that, if present, changes in the spectral signature, even over subnanometer distances, could be detected. Such distances are much shorter than the typical size of the domains seen in inhomogeneous samples [Figs. 16(a) and 16(b)], and the observed homogeneity cannot be ascribed to a broad STM tip.

A second piece of evidence showing that inhomogeneous superconductivity is not essential for a high T_c comes from STM studies by Matsuba, Sakata, Mochiku, *et al.* (2003). They observed that the spread in gap amplitude can be very different in distinct regions on a given Bi2212 surface, although the average gap values, and possibly T_c, are the same. In another systematic study of slightly overdoped Bi2212, Hoogenboom, Kadowaki, *et al.* (2003) demonstrated that spatial gap inhomogeneities as shown in Figs. 16(a), 16(b), and 17(a) were intimately associated with a broad superconducting transition, as measured by ac susceptibility on the same samples. Conversely, single crystals with narrow superconducting transitions ($\Delta T_c < 0.5$ K) yield very homogeneous tunneling spectroscopy as shown in Fig. 17(b). This correlation between a wide gap distribution and the ac-susceptibility transition width was also observed in Bi2223 (Kugler *et al.*, 2006) and suggests that nanometer-length-scale gap inhomogeneities stem from extrinsic stoichiometric disorder rather than intrinsic electronic phase separation.

A very recent study provides further compelling experimental evidence that the gap inhomogeneity is indeed an extrinsic stoichiometric effect, as inferred from
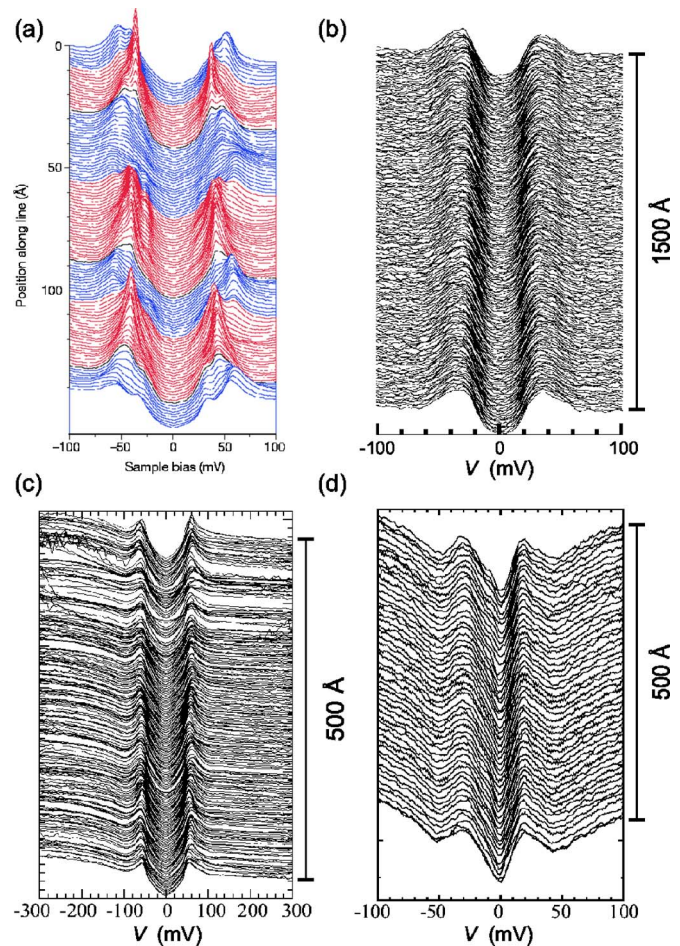

FIG. 17. (Color online) Spatially resolved STM tunneling characteristics measured along different traces on (a) Bi2212 (Lang *et al.*, 2002), (b) Bi2212 (adapted from Renner, Revaz, Genoud, *et al.*, 1998), (c) Bi2223 (Kugler *et al.*, 2006), and (d) Y123 (Maggio-Aprile, 1996). Note the high degree of homogeneity in (b)–(d).

the above experiments. Combining high-resolution topographic and spectroscopic STM maps, McElroy, Lee, Slezak, *et al.* (2005) captured the direct correlation between the gap amplitude and oxygen impurity distributions in real space. This result is in agreement with the spread of spectra measured on inhomogeneous samples (McElroy, Lee, Hoffmann, *et al.*, 2005), whose line shapes vary from typical for optimally doped samples [Fig. 16(c), spectrum 1] to typical for heavily underdoped samples [Fig. 16(c), spectrum 6]. Note, however, that the detailed relation between the local gap and the local oxygen impurity distribution remains unclear and requires further investigations.

In summary, spatial inhomogeneities in the gap amplitude appear to be driven by a property which transition metal perovskite oxides share with all oxides: namely, their propensity to high concentration of defects, especially oxygen inhomogeneities. Note that lead impurities and disorder in the Sr and Ca layers were found to have no effect on the gap inhomogeneity (Kinoda *et al.*, 2003). These results all point at oxygen disorder as the main

cause for inhomogeneities found by spectroscopy. Generally, as-grown samples tend to be inhomogeneous and this tendency increases as doping is reduced. However, these inhomogeneities are not consistent with simple charge segregation in a perfect lattice. Special postsynthesis treatments allow one to make more homogeneous samples with equally high T_c, as has been clearly demonstrated in overdoped Bi2212 (Hoogenboom, Kadowaki, *et al.*, 2003). Most importantly, the experimental evidence is that an inhomogeneous gap distribution is not a prerequisite for the occurrence of high-temperature superconductivity, since there is no correlation between such a distribution and the value of T_c. Note that the oxygen concentration and distribution, however, are probably not the only differences between samples from different sources and batches. Therefore a detailed comparison between other sample parameters has to be taken into account as well.

E. STM on impurities

Impurities in superconductors have been a subject of research since the BCS theory was established. Whereas nonmagnetic impurities were found to have little or no effect on T_c, magnetic impurities turned out to suppress superconductivity. Indeed, for *s*-wave superconductors the Anderson (1959) theorem states that nonmagnetic impurity scattering does not reduce T_c, whereas Abrikosov and Gor'kov (1960) showed how magnetic impurities reduce T_c to zero through exchange scattering at impurity concentrations of the order of 1%. Later on Yu (1965), Shiba (1968), and Rusinov (1969) independently found that magnetic impurity can induce quasiparticle subgap bound states. The first direct observation of such behavior by STM was reported by Yazdani *et al.* (1997) on a Nb surface with Mn, Gd, or Ag adatoms. Ag, believed to be nonmagnetic, has no effect on the superconducting *s*-wave state. However, when Mn or Gd are deposited on the surface of Nb the zero-bias conductance is enhanced when tunneling through magnetic Mn and Gd. The spatial extension of the impurity effect is about 10 Å, and the resulting spectra were found to be asymmetric.

In a *d*-wave superconductor Anderson's theorem does not hold and it is expected that nonmagnetic impurities have a profound effect on the superconducting properties. This has been investigated by several groups (Byers *et al.*, 1993; Lee, 1993; Balatsky *et al.*, 1995). These theories predict local signatures of *d*-wave pairing and variations in the LDOS around the impurities. A review of these theories has been given by Balatsky *et al.* (2006).

The first attempts to study impurities in HTS by STM were carried out by Yazdani *et al.* (1999) and by Hudson *et al.* (1999). The former studied Bi2212 surfaces onto which nanoscale Au dots were deposited from the STM gold tip. It was found that strong zero-bias enhancements occurred in dI/dV when the tip was placed just above these particles, demonstrating the existence of a strong resonance as expected for a *d*-wave supercon-
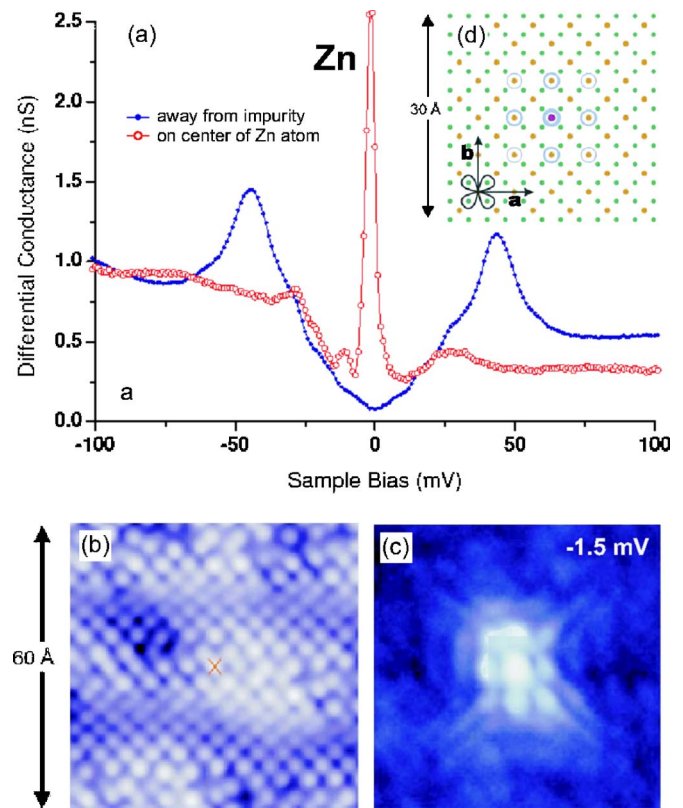

FIG. 18. (Color online) Spectroscopy above a Zn atom in $Bi_2Sr_2Ca(Cu_{1-x}Zn_x)_2O_{8+\delta}$ with $x=0.6\%$ and $T_c=84$ K. (a) Spectra taken at the center and away from the Zn impurity, (b) 60×60 Å^2 topography, and (c) conductance map at -1.5 meV [logarithmic color (gray) scale]. (d) 30×30 Å^2 representation of the square CuO_2 lattice lying below the BiO surface layer. The Zn atom is at the center and the conductance maxima observed in (c) are indicated by circles. Adapted from Pan, Hudson, Lang, *et al.*, 2000 and Balatsky *et al.*, 2006.

ductor. In the latter paper an undoped Bi2212 crystal was studied. Their approach was to make zero-bias conductance maps similar to those of Yazdani *et al.*. These maps showed nanoscale areas with an unusually high zero-bias conductance. Analyzing these unveiled a zero-bias anomaly corresponding to what would be expected from scattering of a *d*-wave superconductor on an impurity. However, the nature of these impurities was not identified in this work.

Following this, Pan, Hudson, Lang, *et al.* (2000) investigated Zn-doped Bi2212. They found an intense quasiparticle scattering resonance at -1.5 meV at many sites on the surface of the sample. Since Zn substitutes for Cu, two layers below the surface it is not seen in topography. However, the effect of the resonant scattering can be seen at low energies. The density of such sites corresponds to about one-third of the nominal concentration of Zn atoms, and it is therefore reasonable to assume that strong zero-bias sites reflect the effect of Zn doping. Figure 18(a) shows spectra away from the impurity and on top of it, the latter displaying a strong zero-bias anomaly coincident with a strong suppression of superconductivity within a 15 Å radius of the scattering sites.
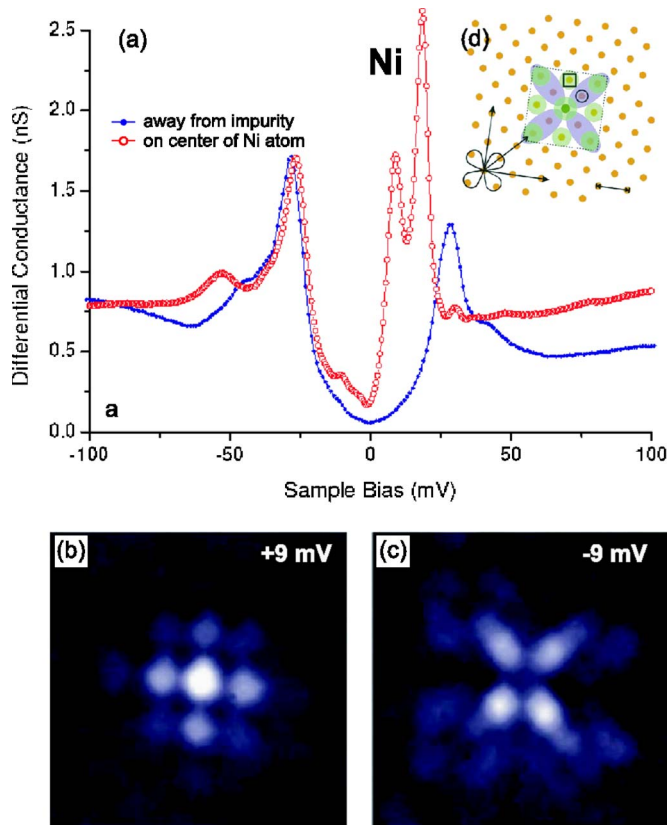
FIG. 19. (Color online) Spectroscopy above a Ni atom in $Bi_2Sr_2Ca(Cu_{1-x}Ni_x)_2O_{8+\delta}$ with $x \approx 0.2\%$ and $T_c = 85$ K. (a) Spectra taken at the center and away from the Ni impurity. (b) (c) 35×35 Å^2 conductance maps at positive (+9 mV) and negative (−9 mV) bias. (d) Position of the Ni atom (center) with respect to the Cu atoms in the invisible CuO$_2$ plane, and schematics of the $d_{x^2-y^2}$ order parameter. Adapted from Hudson *et al.*, 2001 and Balatsky *et al.*, 2006.

Imaging the spatial dependence of the quasiparticle density of states in the vicinity of the impurity atoms directly reveals the fourfold symmetric quasiparticle "cloud" aligned with nodes of the *d*-wave superconducting gap [Figs. 18(b)–18(d)]. Whether this structure reflects the symmetry of the superconducting state or the symmetry of the atomic lattice remains to be determined.

Particularly interesting in this context is a comparison of the effect of magnetic and nonmagnetic impurities substituted on equivalent Cu sites. In comparison to Zn impurities, magnetic Ni impurities lead to very different behavior. This was studied by Hudson *et al.* (2001). At each Ni site they observed two *d*-wave impurity states of apparently opposite spin polarization, whose existence indicates that Ni retains a magnetic moment in the superconducting state [Fig. 19(a)]. However, analysis of impurity-state energies shows that quasiparticle scattering at Ni is predominantly nonmagnetic. The spatial distribution of the conductance maxima around the impurity is strongly asymmetric with respect to the Fermi level [Figs. 19(b) and 19(c)]. Furthermore, they show that the superconducting energy gap is unimpaired at Ni.

This is in strong contrast to the effects of nonmagnetic Zn impurities, which locally destroy superconductivity.

Motivated by STM observations, several microscopic calculations of the electronic structure near Zn or Ni impurities have been reported. Most of these calculations are based on the BCS *d*-wave theory, and they differ mainly in the model employed for the impurity and treatment of the superconducting order parameter modification around the impurity site. In short, impurity potentials in a BCS *d*-wave state induce resonances, either below or above the Fermi energy depending upon the sign of the potential. In the unitary limit the resonance approaches the Fermi energy. The measured LDOS around Zn impurities, however, turns out to be more difficult to understand in this class of models. Indeed, for strong pointlike impurities the spectral weight is expelled from the impurity to neighboring sites and the LDOS at the impurity site is nearly zero, in contrast to experiment. Various solutions to this problem have been put forward. Zhu *et al.* (2000), Zhu and Ting (2001a), and Martin *et al.* (2002) invoked an anisotropic tunneling matrix element, which would filter the tunnel electrons in such a way that the current measured on top of the impurity site in effect originates from neighboring sites. Other authors claimed that correlation effects and the formation of a local moment at the Zn site are important (Polkovnikov *et al.*, 2001). Recently Tang and Flatté (2004) were able to give a fairly complete account of the experimental Zn impurity LDOS by assuming that the Zn potential has a finite spatial extension and by including a modification of the pairing potential and hopping energies in the neighborhood of the Zn site. Which one of these interpretations of the STM data is the right one is still unclear.

F. Cross-sectional tunneling

Most published STM experiments were carried out with the STM tip positioned perpendicular to the perovskite (001) surface. In this *c*-axis tunneling configuration, tunneling samples an angular average over the *ab*-plane density of states (see Sec. III). Here we briefly review the few attempts to do cross-sectional tunneling, i.e., tunneling into an arbitrary plane parallel to the [001] direction with the STM tip perpendicular to the [001] direction. This geometry is attractive for several reasons. It should enable a direct probe of the alternate stacking of insulating and superconducting layers along [001]. It further should allow the $d_{x^2-y^2}$ symmetry of the gap in the CuO$_2$ sheets to be probed by measuring the gap amplitude as a function of the ($hk0$) surface orientation and by detecting the ZBCP expected on (110) and ($\bar{1}10$) surfaces.[11]

Cross-sectional tunneling is a very challenging endeavor, primarily due to the difficulty in preparing a suit-

---

[11]The main theoretical expectations for the electronic structure of superconductors near surfaces or interfaces have been reviewed by Löfwander *et al.* (2001) and Deutscher (2005).
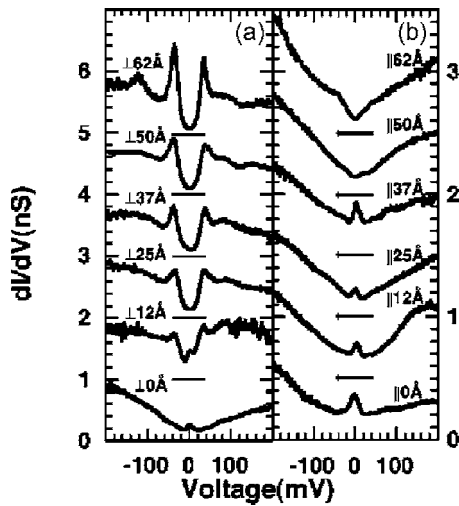
FIG. 20. STM tunneling spectra measured relative to a $[\bar{1}10]$ step edge (45° boundary) on Bi2212 at 4.2 K. (a) Differential conductance spectra measured at increasing distances in the direction perpendicular to the step edge. (b) Differential conductance spectra measured along the step edge. The ZBCP is measured only for tunnel junctions close to the step edge. From Misra *et al.*, 2002b.
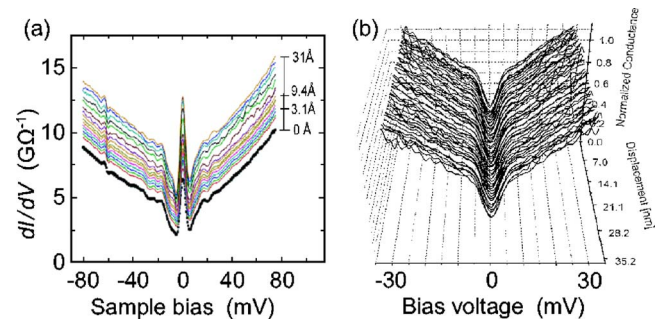

FIG. 21. (Color online) Spatially resolved cross-sectional STM tunneling spectroscopy at 4.2 K. (a) 31-nm trace (running parallel to [001]) on Y123 showing the presence of a ZBCP on the (110) surface of a hole-doped HTS. Adapted from Yeh *et al.*, 2001. (b) 35-nm trace on NCCO showing the systematic absence of the ZBCP on the (110) surface of an electron-doped HTS. Adapted from Kashiwaya *et al.*, 1998.

able surface for STM. The first experiments were performed on Bi2212, resulting in topographic images with atomic-scale resolution of the (100) surface (Hasegawa and Kitazawa, 1990; Hasegawa, Nantoh, Motohira, *et al.*, 1991). Hasegawa *et al.* also found spectroscopic signatures of the alternate stacking along [001] of gapped BiO layers and metallic CuO_2 layers.

The potential to gather experimental evidence on the $d_{x^2-y^2}$ symmetry of the superconducting gap has compelled several groups to attempt cross-sectional tunneling experiments. Suzuki *et al.* (1999c) cut thin Bi2212 single crystals along different $(hk0)$ planes and probed exposed surfaces by STM. The (110) surface revealed a conductance peak at E_F. All other $(hk0)$ surfaces were gapped, with the largest gap on the (100) surface. This is precisely what is expected for a $d_{x^2-y^2}$ gap in the (001) plane. Kane and Ng (1996) did a similar experiment, tunneling into $(hk0)$ edges of a Bi2212 single crystal using a wire aligned parallel to the c axis as the "tip" electrode. These experiments yield a very different result: all surfaces show a gapped spectrum (no ZBCP), and the largest gap is measured on (110) surfaces. This angular dependence of the gap suggests d_{xy} symmetry. However, the absence of any ZBCP makes this experiment inconclusive.

Misra *et al.* (2002b) circumvented the difficulty of preparing cross-sectional surfaces by measuring tunneling characteristics along a $[\bar{1}10]$-oriented step edge of a Bi2212 thin film. The step should give rise to a ZBCP in a superconductor with a $d_{x^2-y^2}$ gap in the (001) plane (Hu, 1994). Indeed, they do find a clear signature of a conductance peak at E_F in the vicinity of the step (Fig. 20). Another interesting result reported by Misra *et al.* (2002b) is the absence of a ZBCP near a 90° twin bound-

ary in Bi2212, indicating that such crystallographic defects are not a strong perturbation for the superconducting state—unlike in Y123, where STM measurements in a magnetic field show that defects strongly perturb the superconducting condensate (Maggio-Aprile *et al.*, 1997).

In Y123, Yeh *et al.* (2001) were able to measure the ZBCP as a function of position along the (110) surface of an optimally doped single crystal [Fig. 21(a)]. The same experiment along the (100) surface showed a large gap at E_F, in agreement with $d_{x^2-y^2}$ symmetry. Y123 can be grown as [110]-oriented thin films, thus offering an alternative approach to measuring the ZBCP. Yeh *et al.* (2001) measured the expected ZBCP on such films, but could not achieve atomic-resolution imaging. Conversely, Nantoh *et al.* (1995) achieved atomic-resolution imaging of [110]-oriented thin films, but failed to observe a ZBCP.

Tanaka *et al.* (1995) measured spatially homogeneous and tip-to-sample distance-independent tunneling spectra on the (100) surface of $La_{1.85}Sr_{0.15}CuO_4$ (La214). However, the spectra show a ZBCP, which is not consistent with $d_{x^2-y^2}$ symmetry, but indicates d_{xy} symmetry. Tanaka *et al.* (1994) also found a d_{xy} gap by cross-sectional spectroscopy in Y123. Introducing momentum-dependent tunneling currents to take account of the shape of the electron wave function of surface oxygen atoms for the evaluation of tunneling matrix elements, Tanaka *et al.* (1995) argued that they can reconcile their data with a $d_{x^2-y^2}$ symmetry of the gap.

The ZBCP appears to be a characteristic property of (110) and $(\bar{1}10)$ surfaces of hole-doped HTS's, in agreement with the d-wave symmetry of the gap. Most STM experiments favor s-wave superconductivity in electron-doped HTS's. One argument is the absence of a ZBCP on (110) surfaces (Alff *et al.*, 1998; Kashiwaya *et al.*, 1998) as shown for $Nd_{1.85}Ce_{0.15}CuO_{4-y}$ (NCCO) in Fig. 21(b). Hayashi, Isoshima, *et al.* (1998) measured a ZBCP on the (100) surface of NCCO, suggesting a d_{xy} symmetry. However, this result seems less systematic, as the

ZBCP is observed in only some of their low-resistance junctions. The relation of these results to other experiments showing *d*-wave symmetry needs further clarification.

The ZBCP has been more extensively investigated using planar and point-contact tunnel junctions, including the influence of disorder and magnetic field [see, e.g., Aprili *et al.* (1998, 1999)]. A very comprehensive discussion of probing the ZBCP by tunneling can be found in two recent reviews by Kashiwaya and Tanaka (2000) and Deutscher (2005).

G. Summary

The very unusual nature of tunneling spectra measured on HTS's was recognized from the first successful tunneling experiments and caught immediate attention. Most striking were the unconventional line shape in hole-doped cuprates, with a finite density of states in the gap, and the large energy scale of the characteristic spectral features. The low-energy line shape has since been explained in terms of the *d*-wave symmetry of the gap. Higher-energy spectral features above the gap are still a matter of discussion—although some good theoretical fits have been worked out—in particular, the asymmetric and doping-dependent background and the dip-hump-feature.

The energy scale of the gap feature in HTS's is way off the expectations of the conventional theory for superconductivity. This is in particular the case for the bismuth compounds (Bi2201, Bi2212, Bi2223). In these materials the gap depends on the doping and number of CuO_2 planes in the unit cell and grows with reducing hole concentration and increasing number of planes. This leads in certain cases to exceptionally high values of $2\Delta_p/k_B T_c$. This surprising behavior has to be viewed in relation to the properties of the pseudogap, to be discussed in the next section.

Spatial inhomogeneities of the superconducting gap have stirred up considerable interest, fueled in part by models where phase separation plays a key role for high-temperature superconductivity. However, experimental evidence strongly suggests that such inhomogeneities are an extrinsic effect, stemming from stoichiometric variations. Most importantly, they are correlated with the superconducting transition width, but not with the maximum value of the bulk transition temperature. Magnetic and nonmagnetic atomic impurities intentionally introduced into CuO_2 planes result in a particular kind of local inhomogeneity, providing an original local test of the pairing state.

VI. PSEUDOGAP

Many experimental techniques provided evidence for an unconventional normal state common to all HTS's and characterized by the opening of a gap in the electronic excitation spectrum at a temperature T^* above the critical temperature T_c, the so-called pseudogap (PG).

This observation initiated an intense debate about its origin, since the answer to this question may turn out to be essential for the understanding of high-T_c superconductivity [for a review see Timusk and Statt (1999)].

The various theoretical interpretations of the pseudogap phenomenon may be roughly classified in two groups. (i) The pseudogap is the manifestation of some order, static or fluctuating, generally of magnetic origin, but unrelated to and/or in competition with the superconducting order.[12] (ii) The pseudogap is the precursor of the superconducting gap, and reflects pair fluctuations above T_c.[13] At present, a definitive answer is still lacking, although the STS results favor the latter, as we shall see, or more generally a situation where both phenomena have the same origin.

Closely related to this fundamental issue is the understanding of the HTS's doping phase diagram, schemati-

---

[12]Most of these theories view the superconducting state of the cuprates as a consequence of doping a Mott insulator. Lee *et al.* (2006) give a comprehensive review of this type of approach. In the resonating valence bond (RVB) theory Anderson (1987) argued that the ground state of a doped antiferromagnet would be a liquid of singlet spin pairs. In this framework the pseudogap appears as the spin gap associated with the breaking of the RVB singlets (Paramekanti *et al.*, 2001; Anderson *et al.*, 2004). Several authors have considered the possibility that doping the cuprates has the effect of weakening some order present in the parent compound. The pseudogap would thus be a consequence of this order, which progressively disappears upon doping as superconductivity sets in, and would vanish at a quantum critical point (QCP) presumably below the superconducting dome. This (possibly dynamical) order could be the AFM order itself (Kampf and Schrieffer, 1990), a state of microscopic orbital currents known as the staggered-flux state (Affleck and Marston, 1988) or *d*-density-wave (DDW) state (Schulz, 1989; Wen and Lee, 1996; Varma, 1997; Chakravarty *et al.*, 2001), a stripe state in which the doped holes order into one-dimensional patterns [Zaanen and Gunnarsson (1989); Emery *et al.* (1990); White and Scalapino (1998); the field was recently reviewed by Kivelson *et al.* (2003) and Carlson *et al.* (2004)], or a spin-density-wave (SDW) and/or charge-density-wave (CDW) state (Chubukov *et al.*, 1996; Varlamov *et al.*, 1997; Vojta and Sachdev, 1999). In some of these theories the two orders appear as two faces of the same coin (Zhang, 1997) or they turn out to be dual to one another (Franz and Tešanović, 2001; Wang, 2004).

[13]The short coherence length of cuprate superconductors suggests that they lie somewhere between the BCS limit of very large momentum-space pairs and the opposite case of small real-space pairs undergoing a Bose-Einstein condensation (BEC) [see the review of Chen *et al.* (2005)]. In this picture the pseudogap is the binding energy of preformed pairs above T_c (Geshkenbein *et al.*, 1997). The BCS-BEC crossover scenario has been studied within the boson-fermion (Ranninger *et al.*, 1995) and attractive Hubbard models (Moreo *et al.*, 1992; Randeria *et al.*, 1992; Micnas *et al.*, 1995). Other approaches emphasize the weak phase stiffness in the underdoped cuprates resulting from the low superfluid density, which would lead to a suppression of T_c by phase fluctuations (Emery and Kivelson, 1995; Schmalian *et al.*, 1997; Franz and Millis, 1998; Giovannini and Berthod, 2001; Lammert and Rokhsar, 2001; Eckl *et al.*, 2002).

cally shown in Fig. 14. How does the pseudogap vary with doping, temperature, and magnetic field? How does the pseudogap scale with T_c and the superconducting gap? Is there a universal HTS doping phase diagram?

In this section we review the key STS results related to the pseudogap under different experimental conditions. In Sec. VI.A we describe the T dependence of the LDOS of Bi2212, Bi2201, and Y123 and analyze the scaling relations between the pseudogap and superconducting gap. In Sec. VI.B we address the observation of the pseudogap at low temperatures inside vortex cores and on disordered surfaces. In Sec. VI.C we discuss the doping phase diagram that results from tunneling experiments reviewed here and finally, in Sec. VI.D, we highlight the key results of this section. The connection between the pseudogap and recently reported experiments revealing spatial modulations in the LDOS is discussed separately in Sec. VIII.

A. Temperature dependence of the local DOS

By the end of the 1980s bulk techniques already revealed unconventional normal-state behavior above T_c, but it took about a decade to obtain sufficient sample and surface quality to evidence the PG spectral signature directly in the DOS using ARPES (Ding *et al.*, 1996; Loeser *et al.*, 1996) and STS (Renner, Revaz, Genoud, *et al.*, 1998).

Measuring the T dependence of the LDOS by STM is a challenge. The difficulty is to prevent the tip from shifting relative to the sample when the temperature is changed, due to uncompensated thermal expansion coefficients in the experimental setup. If the tip does shift, as is usually the case, variations in the $I(V)$ characteristics may be due not only to temperature but also to the different tunneling locations, especially if the spectroscopic properties are not homogeneous over sufficiently large areas as discussed in Sec. V. Not surprisingly, there are only a few relevant T-dependent STM studies of HTS's. The first successful STM experiments were obtained on Bi2212 (Renner, Revaz, Genoud, *et al.*, 1998; Matsuda *et al.*, 1999b), followed by Y123 (Maggio-Aprile *et al.*, 2000) and Bi2201 (Kugler *et al.*, 2001).

1. Case of Bi2212

Historically, the first tunneling results revealing the PG were reported on Bi2212 by Tao *et al.* (1997) on planar junctions and by Renner, Revaz, Genoud, *et al.* (1998) using a STM junction. These experiments showed unambiguously that HTS's do not follow what the BCS theory predicts, namely, that the superconducting gap closes at T_c. In this theory, indeed, both the pairing and phase coherence are lost simultaneously at T_c. The origin of this behavior is illustrated by the reduced gap value $2\Delta/k_B T_c = 3.5$ for an s-wave BCS superconductor, indicating that, at the mean-field critical temperature T_c, thermal fluctuations are strong enough to overcome the pairing energy 2Δ. In the case of underdoped (UD) Bi2212, reduced gap values as high as 20 have been re-
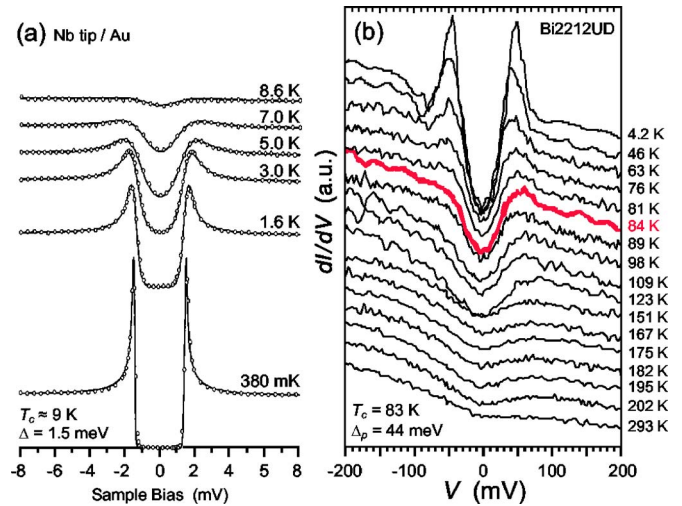

FIG. 22. (Color online) T dependences of the DOS measured by STM. (a) Junction between a gold sample and a niobium tip with $T_c \approx 9$ K, $\Delta_p = 1.5$ meV. Adapted from Pan, Hudson, and Davis, 1998. (b) Junction between an iridium tip and UD Bi2212 with $T_c = 83$ K, $\Delta_p = 44$ meV, and T^* near room temperature. Adapted from Renner, Revaz, Genoud, *et al.*, 1998.

ported (Miyakawa *et al.*, 1999), providing a strong hint that the T dependence of the superconducting gap of HTS's might be very different from the BCS mean-field behavior.

Figure 22 illustrates the T dependence of quasiparticle DOS of niobium (Pan, Hudson, and Davis, 1998),[14] a conventional BCS superconductor, and of UD Bi2212 (Renner, Revaz, Genoud, *et al.*, 1998). The most striking difference from Nb is the existence in Bi2212 of a clear pseudogap at T_c. The pseudogap has basically the same amplitude as the superconducting gap. Both appear to be essentially T independent, seemingly filling up rather than closing with increasing temperature (Tao *et al.*, 1997) except for a slight tendency of the pseudogap to increase upon approaching T^* (see Fig. 26, below). We point out that, although it is well known that in Nb the gap is closing, this is not obvious when looking at Fig. 22(a). The superconducting gap of Nb is of the order of 1.5 meV and $T_c \approx 9$ K. Thermal smearing therefore prevents one from following the coherence peaks in the DOS up to T_c. In contrast, in the case of UD Bi2212 shown in Fig. 22(b), the gap magnitude is about 44 meV for $T_c = 83$ K. Hence $\Delta_p \gg k_B T_c$ and thermal smearing effects relative to Δ_p are much weaker. If the T dependence of the gap were BCS-like, one should thus clearly see it in Fig. 22(b). This is not the case.

The observation that in Bi2212 the gap magnitude is to first approximation T independent rather than following a BCS-like dependence is highlighted in Fig. 23. Here the 4.2-K data of Fig. 22(b) are fitted by a d-wave

---

[14]Note the different gap amplitude compared to Fig. 10(a) for the same experimental configuration, which Pan, Hudson, and Davis (1998) tentatively ascribe to the detailed geometry, structure, and composition of the Nb tip apex.
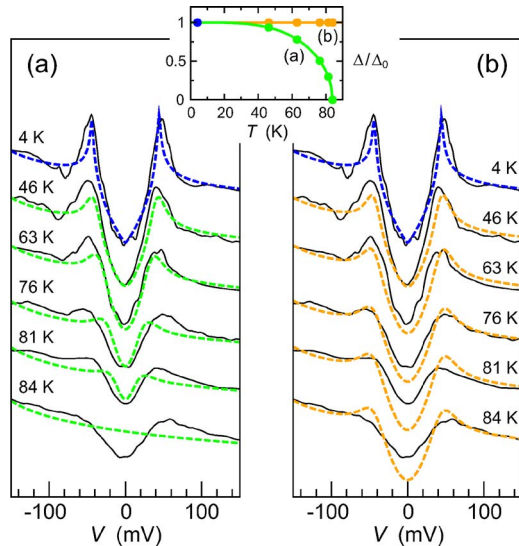
FIG. 23. (Color online) T dependence of the superconducting gap for $T < T_c$. The 4.2 K experimental data [Renner, Revaz, Genoud, *et al.* (1998); see also Fig. 22(b)] are fitted by a *d*-wave function (4 K, dashed line), which is then used to recalculate the spectra at each temperature corresponding to the experimental data, assuming two different gap T dependences: (a) a BCS *d*-wave T dependence and (b) a constant gap magnitude.
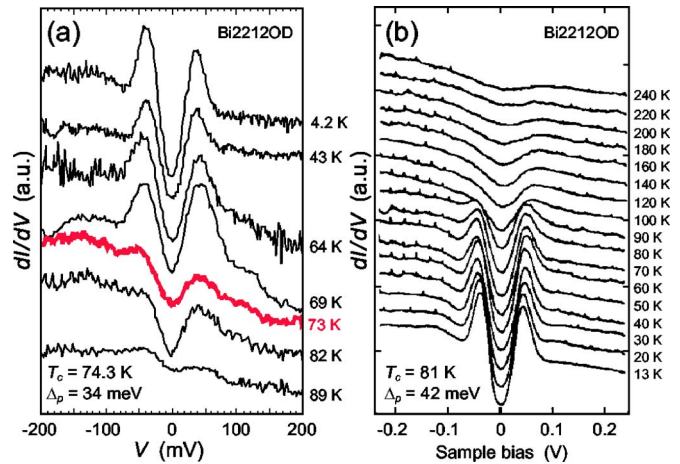

FIG. 24. (Color online) Tunneling spectra vs temperature in overdoped (OD) Bi2212. (a) Strongly OD sample with T_c = 74.3 K and Δ_p = 34 meV. Adapted from Renner, Revaz, Genoud, *et al.*, 1998. (b) Slightly OD sample with T_c=81 K and Δ_p=42 meV. Adapted from Matsuda *et al.*, 1999a. The tunnel resistances are of the order of 1 GΩ.

BCS DOS (dashed curve at 4 K). The asymmetric background is generated by pushing the van Hove singularity of the tight-binding dispersion down to −200 meV. Subsequently, the spectrum is recalculated at each temperature corresponding to the experimental data of Fig. 22(b) up to T=84 K ≈ T_c by assuming two different T dependences for the gap: (i) a BCS *d*-wave T dependence which simulates a closing gap [Fig. 23(a)] and (ii) a T-independent gap [Fig. 23(b)]. This latter simulation reproduces much better the T behavior of the gap magnitude than the BCS case. A more careful look at the data [Fig. 22(b)] reveals other key features which are generic for the T dependence of the DOS in Bi2212.

First, by raising the temperature, the coherence-peak intensity is rapidly reduced at the bulk T_c. The coherence peak at negative bias, as well as the dip-hump feature, is suppressed and a reduced peak shifting to a slightly higher energy remains at positive bias. Suppression of the coherence peaks at T=T_c, clearly observed in Figs. 22(b), 24(a), and 25(a), is strong evidence that in Bi2212 T_c at the surface is identical to the one of the bulk.[15] We note, however, that in some cases, and predominantly in underdoped samples which are more prone to inhomogeneous oxygen distributions (see Sec. V), observation of this typical PG signature does not always coincide with the bulk T_c (Matsuda *et al.*, 1999a, 1999b). As mentioned earlier, a possible explanation

could be that, due to thermal drift and sample inhomogeneity, the tip probes regions with different doping levels as the temperature is changed. Conversely, a T-independent gap magnitude, as observed in Fig. 22(b), proves a high level of homogeneity and demonstrates that the local doping level is not changing with temperature. This point is reinforced by the finding that the asymmetric background conductance does not change with temperature [Fig. 22(b)]. The argument is based on the observation that the slope of the background varies with doping (Kugler *et al.*, 2006), possibly as a consequence of band-structure effects (Hoogenboom, Berthod, *et al.*, 2003) and/or strong-correlation effects (Rantner and Wen, 2000; Anderson and Ong, 2006). For a discussion of the background conductance, see also Sec. V.C.

Second, on crossing T_c, the superconducting spectra evolve continuously into the pseudogap with a gap magnitude that is to first approximation constant. It is clear from Figs. 22(b) and 24 that the pseudogap also does not change much with temperature except by a general broadening of the gap edges due to thermal smearing at high temperatures. The pseudogap is thus filling up— hence the zero-bias conductance increases monotonically with temperature as reported first by Tao *et al.* (1997)—and smoothly vanishes at a crossover temperature T^*, which appears to be about room temperature in the data shown in Fig. 22 on UD Bi2212 (see Table II).

A third remarkable property is illustrated in Fig. 24: The pseudogap is not only bound to the underdoped regime, but also exists in overdoped samples (Renner, Revaz, Genoud, *et al.*, 1998; Matsuda *et al.*, 1999a, 1999b). The main difference from the underdoped case is that the gap and pseudogap magnitudes are smaller and that the pseudogap seems to vanish more quickly with increasing temperature. Indeed, the PG temperature for UD Bi2212 is about room temperature [Figs.
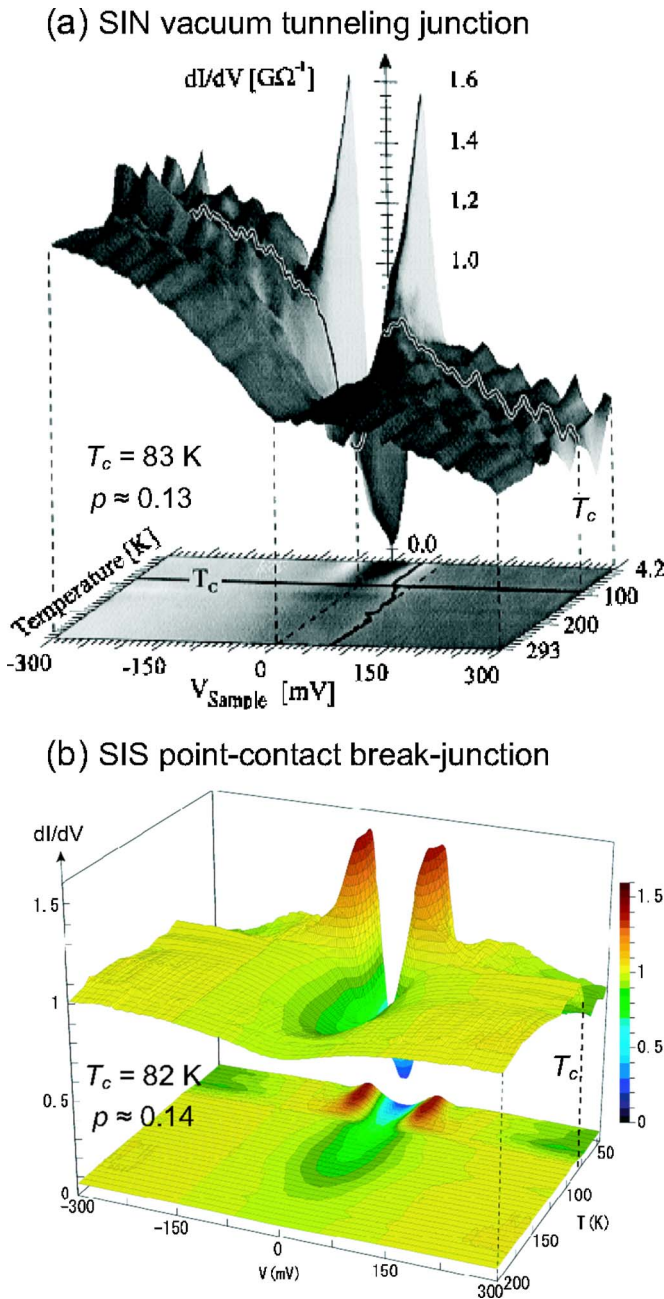
---

[15]This is true under the assumption that coherence peaks are indeed due to superconductivity. This fact is generally accepted and has furthermore been demonstrated in details by ARPES (Feng *et al.*, 2000).

(a) SIN vacuum tunneling junction

$T_c = 83$ K
$p \approx 0.13$

(b) SIS point-contact break-junction

$T_c = 82$ K
$p \approx 0.14$

FIG. 25. (Color online) T dependence of the DOS of Bi2212 for two different junction types and tunneling techniques. (a) SIN vacuum tunneling using STM, $T_c = 83$ K, $\Delta_p = 44$ meV, $T^* \approx 300$ K, and $R_t = 0.1$–1 GΩ. From Renner, Revaz, Genoud, *et al.*, 1998. (b) SIS junction using PC-BJT, $T_c = 82$ K, $\Delta_p \approx 27$ meV, $T^* \approx 180$ K, and $R_t = 10$–100 kΩ; From Dipasupil *et al.*, 2002.

22(b) and 25(a)]. In overdoped samples, with correspondingly smaller gaps, T^* is smaller but well above T_c [Fig. 24(a)]. These results indicate that the PG magnitude and PG temperature scale with the superconducting gap Δ_p in Bi2212. This key observation is discussed in Sec. VI.A.5.

Recently Vershinin, Misra, Abe, *et al.* (2004) and Vershinin, Misra, Ono, *et al.* (2004) succeeded in studying the spatial dependence of the tunneling conductance in the PG state above T_c on Bi2212. They observed spectra consistent with the generic PG signature described above. Investigating conductance maps at low energies, they also found small variations in the LDOS with an energy-independent incommensurate periodicity. The origin of these modulations and their connection to the PG state are discussed in Sec. VIII.

STM junctions are generally of the SIN type, whereas techniques like point-contact break-junction tunneling (PC-BJT) and intrinsic Josephson junction tunneling (IJJT) provide SIS tunneling barriers. In the following we briefly comment on the main findings of those techniques and compare them to STM vacuum tunneling.

In the case of PC-BJT, a tip is driven into the sample surface. By slightly reducing the pressure applied by the crashed tip it is possible to pick up a cleaved crystal piece, thus providing a SIS vacuum tunnel junction with typical tunnel resistances of 10–100 kΩ (Ozyuzer *et al.*, 2000; Dipasupil *et al.*, 2002). In the case of IJJT, the Bi-based cuprate crystal is considered as a stack of multiple Josephson junctions formed between superconducting CuO$_2$ planes separated by insulating BiO layers. Driving a current along the *c* axis of small crystal mesas provides intrinsic SIS junctions without any vacuum barrier and with typical tunnel resistances below 10 Ω per junction (Kleiner *et al.*, 1992; Suzuki *et al.*, 1999c; Yurgens *et al.*, 1999; Krasnov *et al.*, 2000).

In Fig. 25 we show results reported by Dipasupil *et al.* (2002) on Bi2212 SIS junctions using PC-BJT and compare them to the STM data by Renner, Revaz, Genoud, *et al.* (1988) on a Bi2212 SIN junction. The spectral features at low temperatures, like the dip hump and the characteristic *d*-wave V-shaped DOS, as well as the overall T dependence, including the observation of the pseudogap on overdoped samples, and the scaling behavior between Δ_p and T^*, are remarkably consistent. However, various studies by other groups showed that strong discrepancies exist among data acquired with the PC-BJT technique: data reported by Miyakawa *et al.* (1998) did not show any pseudogap on optimally doped Bi2212, and results by Ozyuzer *et al.* (2002) on underdoped Bi2212 with $T_c = 77$ K showed PG-like spectra that vanish already at about 80 K. The origin of these diverging results is most likely the ill-defined junction geometry and the difficult junction control under variable temperatures.

Over recent years IJJT in Bi2212 (Suzuki *et al.*, 1999c; Krasnov *et al.*, 2000; Heim *et al.*, 2002) and Bi2201 (Yurgens *et al.*, 2003) mesas have attracted considerable attention. These studies revealed a double-gap structure in the DOS: a strongly peaked gap developing on top of a much broader excitation gap, which were identified as the superconducting gap and the pseudogap, respectively. The sharply peaked gap shows a BCS-like T dependence and closes at T_c, whereas the broad hump is almost T independent and visible even below T_c (Krasnov *et al.*, 2000; Yurgens *et al.*, 2003). The authors of these studies claimed to distinguish between and simultaneously observe both the superconducting gap and the

TABLE II. Low-T gap amplitude Δ_p and PG temperature T^* as obtained by tunneling experiments. References are classified from underdoped to overdoped for each compound.[a]

Compound	T_c (K)	Δ_p (meV)	T^* (K)	$2\Delta_p/k_B T_c$	$2\Delta_p/k_B T^*$	Reference
Bi2212[b]	60 UD	36 ± 2	217 ± 9	13.9	3.8	Oda *et al.* (1997)
Bi2212[c]	77 UD	40	200 ± 8	12.1	4.6	Dipasupil *et al.* (2002)
Bi2212[c]	82 UD	36	180 ± 8	10.2	4.6	Dipasupil *et al.* (2002)
Bi2212	83 UD	44 ± 2	~290	12.3	3.5	Renner, Revaz, Genoud, *et al.* (1998)
Bi2212	90 OP	54 ± 3	~300	13.9	4.2	Matsuda *et al.* (1999b)
Bi2212[b]	88 OP	32 ± 2	142 ± 9	8.4	5.2	Oda *et al.* (1997)
Bi2212[d]	87 ?	36 ± 1	130 ± 20	9.6	6.4	Tao *et al.* (1997)
Bi2212	84 OD	50 ± 4	~270	13.8	4.3	Matsuda *et al.* (1999b)
Bi2212[c]	82 OD	25	120 ± 8	7.1	4.8	Dipasupil *et al.* (2002)
Bi2212	81 OD	43 ± 2	~220	12.3	4.5	Matsuda *et al.* (1999b)
Bi2212[b]	81 OD	27 ± 2	104 ± 9	7.7	6.0	Oda *et al.* (1997)
Bi2201	<4 UD	16 ± 3	105 ± 15		3.5	Kugler (2001)
Bi2201	10 OD	12 ± 3	68 ± 2	28	4.1	Kugler *et al.* (2001)
Y123	92 OP	20 ± 1	92	5	5	Maggio-Aprile *et al.* (2000)
Nd123	95 OP	30	95	7.3	7.3	Nishiyama *et al.* (2002)
La214[b]	~40 UD	~16	82 ± 15	9.3	4.5	Nakano *et al.* (1998)
La214[b]	~40 OD	~10	53 ± 10	5.8	4.4	Nakano *et al.* (1998)

[a]The identification as underdoped or overdoped is the one given by the authors.
[b]T^* is determined by in-plane resistivity measurements.
[c]SIS point-contact break junction.
[d]Pb-Bi2212 planar junction.

pseudogap, and concluded that their origins are different. These results appear to be in strong contradiction with STM results. A possible explanation is that the tunneling regime in IJJT is radically different from that in STM, since the tunneling resistance R_t in IJJT is typically below 10 Ω, whereas for STM $R_t \sim 0.1$–1 GΩ. Heating effects might thus play an important role in IJJT. Indeed, very recently it was demonstrated that the spectral features attributed to the pseudogap and to the superconducting gap are artifacts of Joule heating in the mesas (Yurgens *et al.*, 2004; Zavaritsky, 2004a, 2004b). Hence, the interpretation of IJJT experiments needs to be carefully reconsidered.

2. Case of Bi2201

The single-CuO_2-layer $Bi_2Sr_2CuO_{6+\delta}$ for long stayed in the shadow, having a much lower T_c and being more difficult to grow with reasonable homogeneity than Bi2212. However, with the need to explore how far the behavior of Bi2212 is generic for the Bi-compound family and, in extension, for HTS cuprates, much interest was recently rekindled in Bi2201.

Kugler *et al.* (2001) reported the first STS study on Bi2201, which revealed low-temperature spectra with well-developed coherence peaks at $\Delta_p \approx \pm 12$ meV. This is a remarkable result, since for a T_c of only 10 K the gap magnitude is extremely large. It is by a factor of 7 larger than the BCS d-wave prediction $\Delta_{BCS} = 2.14 k_B T_c$

$= 1.8$ meV. This further leads to a very high reduced gap $2\Delta_p/k_B T_c \approx 28$, which is even more notable since the investigated sample was overdoped. Based on the observations collected on Bi2212 and assuming that Bi2201 behaves similarly, one would expect a PG state extending over an extremely wide T range above T_c.

Figure 26 reproduces the T dependence of the DOS obtained by Kugler *et al.* (2001) on a slightly overdoped sample. The spectral features are less sharp than in Bi2212 and show a slight scattering, thus requiring averaging over a large number of spectra to extract the general behavior. In spite of that, the data clearly show that the pseudogap exists also on the overdoped side and that its magnitude is comparable to the superconducting gap. Furthermore, it is obvious that the gap magnitude is to first approximation T independent. The overall DOS evolution is thus similar to what has been observed in Bi2212 [Figs. 22(b), 24, and 25], although Bi2201 has a much lower T_c and a smaller superconducting gap.

The T interval of the PG state is extremely large compared to the superconducting one, as illustrated in Fig. 26(b). There is a factor of 7 between T^* and T_c, the same as between Δ_p and Δ_{BCS}. T^* thus scales with Δ_p. This important observation is confirmed in a strongly underdoped sample, although the uncertainty on T^* is much larger due to sample inhomogeneity (see Table II).

Based on these data, Kugler *et al.* (2001) drew a tentative doping phase diagram for Bi2201 [Fig. 26(c)], il-
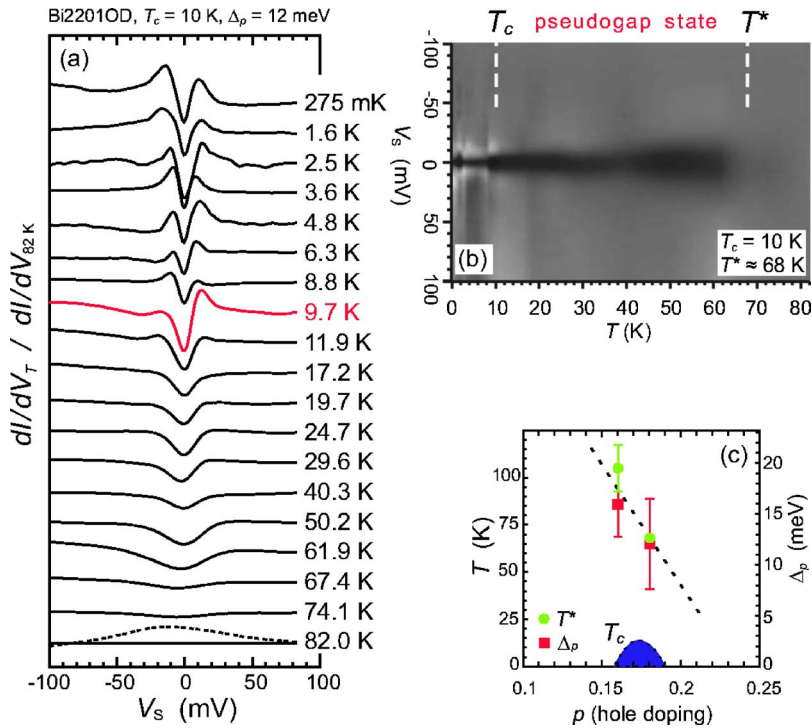
FIG. 26. (Color online) Psendogap in Bi2201. (a) T dependence of the DOS in Bi2201. (b) Top-view representation of (a). (c) Doping phase diagram showing the values of T_c, Δ_p, and T^* from Table II. The doping level p was determined as described by Ando *et al.* (2000). From Kugler *et al.*, 2001.

lustrating that the PG phase extends significantly over the superconducting dome. This is particularly obvious in the overdoped regime and highlights that in this compound T_c is strongly suppressed. For pure Bi2201, T_c^{max} is about 13 K (Gorina *et al.*, 1998; Vedneev *et al.*, 1999). The reasons for such a low T_c relative to the gap Δ_p are most probably disorder and strong phase fluctuations. Whether this anomalous loss of phase coherence is a hallmark of single-layer compounds remains an open issue. Preliminary results on La-doped Bi2201 [slightly underdoped (Kugler, 2000)] showed gap magnitudes Δ_p comparable to that in pure Bi2201, but for a T_c as high as 29 K ($T_c = 36$ K; Ando *et al.*, 2000). This suggests that La doping does not change the pairing energy but rather favors phase coherence. It yields a reduced gap of the order of 10, which is consistent with Bi2212, and restores the superconducting phase accordingly to the generic phase diagram shown in Fig. 14, where the PG state is less dominant on the overdoped side. These findings point out that in the case of HTS's, the relation between Δ_p and T^* is much more robust than the relation between Δ_p and T_c (see Sec. VI.A.5).

3. Case of Y123 and Nd123

We finally turn to the T dependence of compounds having both CuO_2 planes and CuO chains, in particular Y123 and Nd123. Figure 27(a) shows the results obtained by Maggio-Aprile *et al.* (2000) on optimally doped Y123. The coherence peak position, hence the superconducting gap, remains constant with rising temperature, which is consistent with Bi-based compounds. In contrast, the gap progressively fills up and eventually closes at the bulk T_c, demonstrating that there is no signature of any pseudogap above the bulk T_c in optimally doped

Y123. Very similar results were reported on Nd123 (Nishiyama *et al.*, 2002) as shown in Fig. 27(b). These observations are consistent with results from other techniques [see review by Timusk and Statt (1999)]. Thus in spite of the fact that Y(Nd)123 and Bi2212 have the same T_c, they display very different behavior with respect to the pseudogap. A possible key for understanding this difference is that Y(Nd)123 is much less aniso-
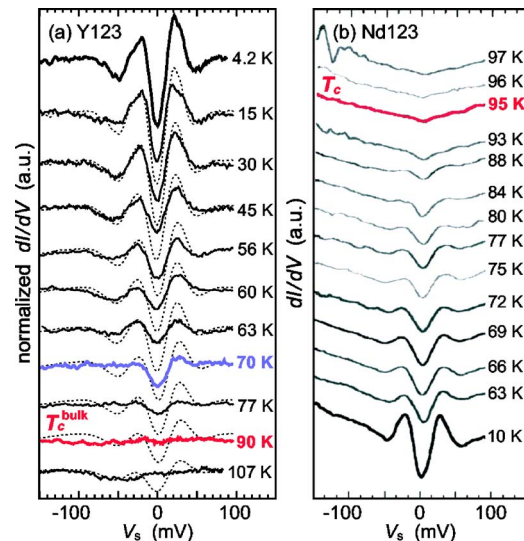

FIG. 27. (Color online) Temperature evolution in Y123. (a) T dependence of optimally doped Y123 ($T_c = 92$ K, $\Delta_p = 20$ meV). The spectra (solid lines) are normalized to the background conductance taken at $V > 100$ mV and extrapolated to $V = 0$. Dotted spectra correspond to the 4.2-K spectrum thermally smeared to the different temperatures. From Maggio-Aprile *et al.*, 2000. (b) T dependence of Nd123 ($T_c = 95$ K, $\Delta_p = 30$ meV). Adapted from Nishiyama *et al.*, 2002.

tropic and appears to be much closer to the BCS limit than Bi2212 (Junod *et al.*, 1999). Furthermore, the reduced gap values for optimally doped Y123 (~5) and Nd123 (~7) are closer to the *d*-wave BCS ratio (~4.3). The consequence is that Y(Nd)123 is less affected by superconducting fluctuations than Bi2212, thus possibly explaining the absence of a pseudogap. Another major difference comes from the CuO chains. How far these chains could prevent the existence of a pseudogap remains to be elucidated.

Besides these differences, Fig. 27(a) reveals other interesting aspects. A clear dip-hump feature is observed at about ±50 meV. This structure looks similar to what is seen in Bi2212 (see Sec. V.B), and it consistently disappears as *T* approaches T_c. Maggio-Aprile *et al.* (2000) showed that this disappearance is not due to thermal smearing, suggesting that the dip is related to the superconducting state. In fact, it turns out that the dip disappears at 70 K where the spectral line shape strongly resembles the Bi2212 spectrum at $T = T_c$ (Figs. 22 and 24). This could indicate that at the surface of Y123 the coherent superconducting state disappears at about 70 K and that above it a PG state exists up to 90 K. The explanation would be that the surface T_c is different from the bulk T_c in Y123 due to a higher effective anisotropy at the surface (Meingast *et al.*, 2001). However, this interpretation remains speculative since the gap signal above 70 K is too weak to make a decisive statement. A discussion of the doping phase diagram of Y123 is presented in Sec. VI.C.

4. Case of electron-doped cuprates

A crucial question for understanding the microscopic mechanism of HTS's is to what extent electron-doped cuprates $R_{2-x}Ce_xCuO_{4-y}$ (*R*CCO; *R*=rare earth) are similar to hole-doped HTS's. The specific issue of the existence of the pseudogap has been investigated using various tunneling techniques, although only very few reports exist. In Fig. 28(a) we reproduce STS data obtained on optimally doped NCCO single crystals by Hayashi, Ueda, *et al.* (1998). These results were confirmed by grain-boundary junction tunneling (GBJT) on optimally doped NCCO and PCCO thin films by Kleefisch *et al.* (2001) [Fig. 28(b)]. The general behavior is very similar to that of Y123 or Nd123, with the main conclusion that no pseudogap is observed at optimal doping.

In contrast, when driving the superconductor into the normal state by applying a magnetic field, a clear PG spectrum appears which has the same magnitude as the superconducting gap at zero field (Biswas *et al.*, 2001; Kleefisch *et al.*, 2001). This is consistent with what is observed in Bi2212 vortex cores (Sec. VI.B.1). Alff *et al.* (2003) investigated how this pseudogap evolves with doping and determined T^*. They observed that T^* has a similar doping dependence to that of the hole-doped copper oxides, but with the important difference that $T^* < T_c$ in the investigated doping range. The authors concluded that in electron-doped cuprates the PG phase coexists and competes with superconductivity and mentioned the possible existence of a quantum critical point.

5. Scaling properties: Pseudogap versus superconducting gap

An important step toward understanding the PG origin is to search for relations between the gap and pseudogap magnitudes, as well as between T_c and T^*. The superconductors described in this section are an ideal stage for such an analysis. Bi2212 acts as a template, whereas Bi2201 and Y123 allow one to test if scaling behaviors are generic. Bi2201 presents the advantage of having a crystal structure similar to the Bi2212 but radically different superconducting parameters T_c and Δ_p, whereas Y123 and Bi2212 have comparable T_c's but different crystal structures.

Figure 29(a) compares the low-*T* superconducting DOS and the PG spectrum measured slightly above T_c in Bi2212 and Bi2201. The superconducting gap clearly increases with underdoping (see also Fig. 15), and the pseudogap behaves exactly the same in both compounds. Moreover, the relative amplitude of these two gaps is nearly the same in both compounds, independent of doping as shown in Fig. 29(b) (Kugler *et al.*, 2001). This consistency is remarkable since the energy scale given by Δ_p varies by about 400%. Whether the scaling between the pseudogap and superconducting gap observed in Bi cuprates also applies to Y123 remains to be seen. This question may be answered by investigating the DOS *T* dependence of underdoped samples, where other techniques have suggested that a pseudogap exists [see review by Timusk and Statt (1999)].
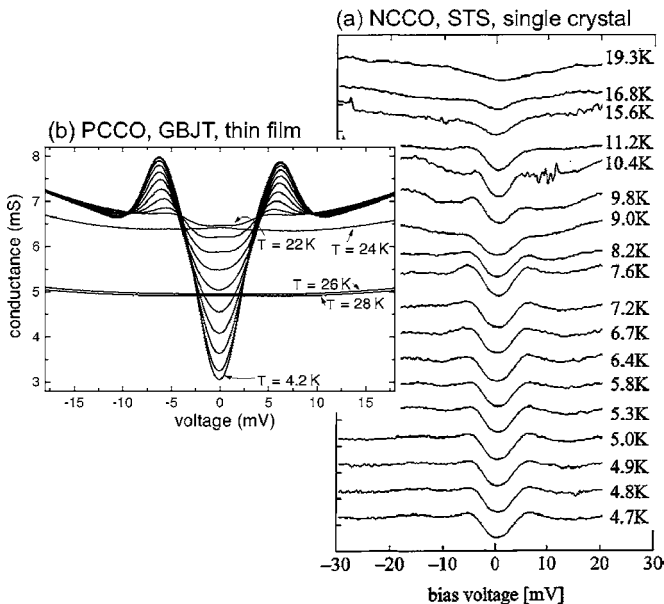

FIG. 28. Temperature evolution in electron-doped cuprates. (a) *T* dependence by STS of a $Nd_{1.85}Ce_{0.15}CuO_4$ single crystal (optimally doped, $T_c=20.5$ K, $\Delta_p \approx 4.5$ meV). The tip is parallel to the [110] direction. From Hayashi, Ueda, *et al.*, 1998. (b) *T* dependence by grain-boundary junction tunneling (GBJT) on a $Pr_{1.85}Ce_{0.15}CuO_4$ thin film (optimally doped, $T_c \approx 24$ K, $\Delta_p =3.1$ meV). Note that these junctions are of the SIS type and in plane. From Kleefisch *et al.*, 2001.
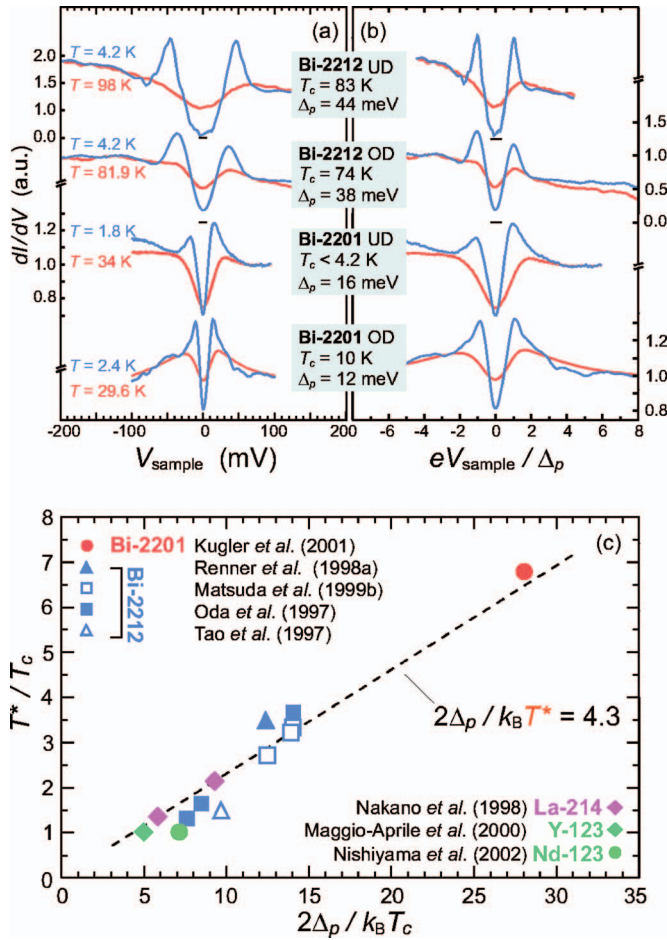
FIG. 29. (Color) Scaling relations. (a) Comparison of the pseudogap and superconducting gap for Bi2212 and Bi2201. (b) Same data with energy rescaled by Δ_p. (c) T^*/T_c as a function of $2\Delta_p/k_BT_c$ for various cuprates investigated by tunneling spectroscopy. Dashed line corresponds to the mean-field d-wave relation $2\Delta_p/k_BT^*=4.3$, where T_c is replaced by T^*. See Table II for detailed superconducting parameters. Adapted from Kugler *et al.*, 2001.

The existence of a scaling relation between Δ_p and T^* was first noticed by Oda *et al.* (1997) in Bi2212 and by Nakano *et al.* (1998) in La214.[16] As shown in Fig. 29(c), the same scaling law also holds for Bi2201 (Kugler *et al.*, 2001), although $2\Delta_p/k_BT_c$ is 2-3 times larger. Optimally doped Y123, where $T^* \lesssim T_c$ (Maggio-Aprile *et al.*, 2000), also fits into the picture. This consistency among various compounds is strong evidence that the scaling is robust. Moreover, the graph reveals that $2\Delta_p/k_BT^* \approx 4.3$, which corresponds to the BCS d-wave relation with T^* playing the role of T_c. This finding clearly supports the idea that T^* is the mean-field BCS temperature and reflects the interaction energy leading to superconductivity.

---

[16]In both cases the T^* values were determined by in-plane resistivity measurements.
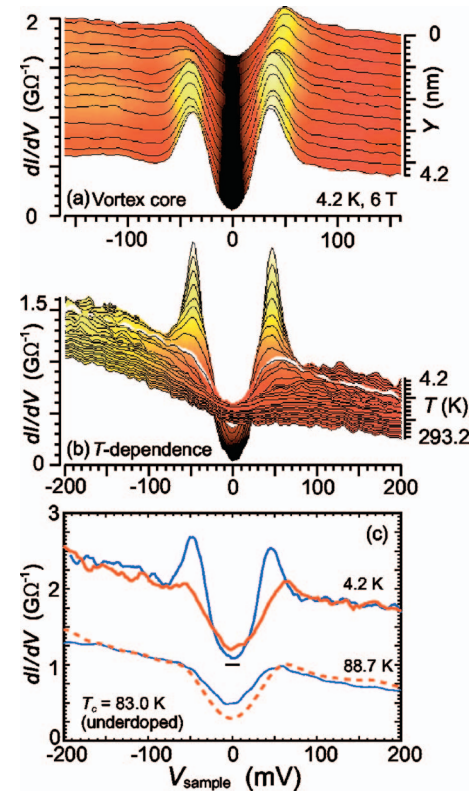

FIG. 30. (Color) Comparison of the pseudogap measured above T_c and the LDOS inside the vortex core of Bi2212. (a) Spatial evolution of the LDOS when moving the tip from the center ($Y=0$) to the periphery of the vortex core ($Y=4.2$ nm) at 4.2 K and 6 T (Bi2212 OD; Renner, Revaz, Kadowaki, *et al.*, 1998). (b) T dependence of the DOS. The pseudogap measured at $T \approx T_c = 83$ K is highlighted in white (Bi2212 UD). Adapted from Renner, Revaz, Genoud, *et al.*, 1998. (c) Top: superconducting gap (blue) measured between vortices at 4.2 K and 6 T compared to a vortex-core spectrum (red). Bottom: pseudogap measured on the same sample in zero field at $T=88.7$ K $> T_c$ (solid line), compared to the vortex-core spectrum numerically smeared to 88.7 K (dashed red) (Bi2212 UD). Adapted from Renner, Revaz, Kadowaki, *et al.*, 1998.

B. Pseudogap at low temperatures

Various STS studies demonstrated that the characteristic PG signature not only is observed above T_c, but also occurs at low temperatures inside vortex cores (Renner, Revaz, Kadowaki, *et al.*, 1998) and on strongly disordered surfaces (Cren *et al.*, 2000; McElroy *et al.*, 2004).

1. Pseudogap inside vortex cores

The spatial dependence of the LDOS at low temperatures and in magnetic fields has been investigated by different groups on Bi2212 (Renner, Revaz, Kadowaki, *et al.*, 1998; Hoogenboom, Renner, *et al.*, 2000; Pan, Hudson, Gupta, *et al.* 2000) and Y123 (Maggio-Aprile *et al.*, 1995, 1997; Shibata *et al.*, 2003b), and revealed the unconventional spectral signature of vortex cores in these compounds, as discussed in detail in Sec. VII.

Here we focus on the relation between vortex-core spectra observed on Bi2212 and the pseudogap above T_c.

Renner, Revaz, Kadowaki, *et al.* (1998) measured the evolution of the spectra when the tip is moved across a vortex core (VC) on a Bi2212 surface [Fig. 30(a)]. Outside the VC the spectra do not depend on tip position and present well-defined coherence peaks and the characteristic dip hump. Moving into the VC the coherence peak at negative bias is suppressed over a typical distance of 10 Å, whereas the peak at $+\Delta_p$ is reduced and shifts to slightly higher energy. This behavior is strikingly similar to the T dependence of the DOS when crossing T_c, as illustrated in Fig. 30. In Fig. 30(c) the VC spectrum is numerically smeared to the temperature where the pseudogap is measured, showing again the similarity of both line shapes. From this Renner, Revaz, Kadowaki, *et al.* (1998) conclude that the LDOS measured at the vortex center is the normal-state PG signature and that the spectrum measured above T_c is essentially the thermally smeared low-T LDOS. This implies that the PG magnitude, like the superconducting gap (Fig. 23), is T independent. Furthermore, as shown in Fig. 30(c), the VC gap magnitude is to first approximation equal to the superconducting gap measured just outside the core. Renner, Revaz, Kadowaki, *et al.* (1998) also showed that these findings are doping independent and therefore consistently obey the scaling properties derived for the pseudogap measured above T_c (Fig. 29).

The correspondence between the normal-state pseudogap and the vortex-core spectra, as well as the doping and T dependence of the spectra reviewed, respectively, in Sec. V and VI.A, has important consequences and raises crucial questions with respect to the origin of the pseudogap.

Does the superconducting state develop on top of a gapped conductance background originating from an independent PG state, similar to the charge-density-wave gap observed in dichalcogenides [see, e.g, Wang *et al.* (1990); Coleman *et al.* (1992)]? If the pseudogap were to have an origin different from superconductivity, then the normal-state gap would not necessarily need to have the same amplitude as the superconducting gap. This scenario could explain why the pseudogap is observed in vortex cores, but is difficult to reconcile with the fact that the two gaps scale with each other as the doping is changed.

An important question related to the correspondence between the pseudogap and the vortex core is whether the PG state between T^* and T_c is due to fluctuating vortices. Thermal transport experiments by Wang *et al.* (2001) support this idea. They found an anomalous Nernst signal above T_c in La214 and Bi2201, which they attributed to vortexlike excitations. They pointed out that this regime penetrates deep into the PG phase and appears predominantly in underdoped samples. They interpreted these results in terms of strong fluctuations between the PG state and the d-wave superconducting phase (Emery and Kivelson, 1995; Norman *et al.*, 1998; Franz and Tešanović, 2001; Lee and Wen, 2001). These

vortexlike excitations could be electronic excitations specific to the PG state or, as suggested by tunneling data (Renner, Revaz, Kadowaki, *et al.*, 1998, Fig. 30), they could be Abrikosov vortices of the superconducting condensate formed in the normal state by phase fluctuations. In the latter scenario the pseudogap would have the same origin as superconductivity, raising the interesting question of its magnetic field dependence.

The field dependence of the pseudogap above T_c has not yet been investigated systematically by STS.[17] However, Hoogenboom, Renner, *et al.* (2000) showed on Bi2212 at 4.2 K that the energy of the core states and the superconducting gap in between cores scale and are field independent, at least at moderate fields up to 6 T (Sec. VII). The PG state under fields as high as 60 T has been investigated by c-axis transport measurements in Bi2212 by Krusin-Elbaum *et al.* (2003). These experiments showed that above ~ 20 T the c-axis resistivity, which is believed to be proportional to the Fermi-level DOS, increases notably, indicating that the pseudogap is filling up with increasing field. Krusin-Elbaum *et al.* also determined the pseudogap closing field H_{PG}, which for an overdoped sample extrapolates to about 90 T at T_c $=67$ K. Remarkably, H_{PG} scales with T^* as $g\mu_B H_{\mathrm{PG}}$ $\approx k_B T^*$, and hence with Δ_p (Sec. VI.A.5). These results fit well into a picture where the PG state is formed of incoherent pairs, that eventually break at the depairing field H_{PG}.

In this context, we mention grain-boundary junction tunneling experiments performed on the electron-doped cuprates NCCO and PCCO (Biswas *et al.*, 2001; Kleefisch *et al.*, 2001). The suppression of superconductivity by a strong magnetic field results in a PG-like spectrum at H_{c2} (see also Sec. VI.A.4). Kleefisch *et al.* (2001) also demonstrated that the pseudogap closes at a field corresponding to the Clogston paramagnetic limit (Clogston, 1962; Yang and Sondhi, 1998).

2. Pseudogap on disordered surfaces

Over the past years many studies focused on spatial variations of the LDOS at the nanometer scale under the influence of disorder. Here we discuss the local observation of the pseudogap at low temperatures and zero magnetic field in Bi2212 thin films (Cren *et al.*, 2000) which have a high degree of structural disorder, in UD Bi2212 single crystals (Howald *et al.*, 2001), where disorder has been introduced intentionally by local damage, and in inhomogeneous samples, where disorder is

---

[17]Ng and Gupta (2000) investigated Bi2212 using PC-BJT. No field dependence of the pseudogap was observed up to 1.1 T; Krasnov *et al.* (2001) investigated Bi2212 mesas by IJJT. The spectral signature they attributed to the pseudogap is invariant at least up to 14 T. Note, however, that this structure has been attributed to an artifact of Joule heating in the mesas (see Sec. VI.A.1). Anagawa *et al.* (2003) performed similar investigations up to 9 T. They observe that both the pseudogap structure and superconducting gap are essentially field independent.
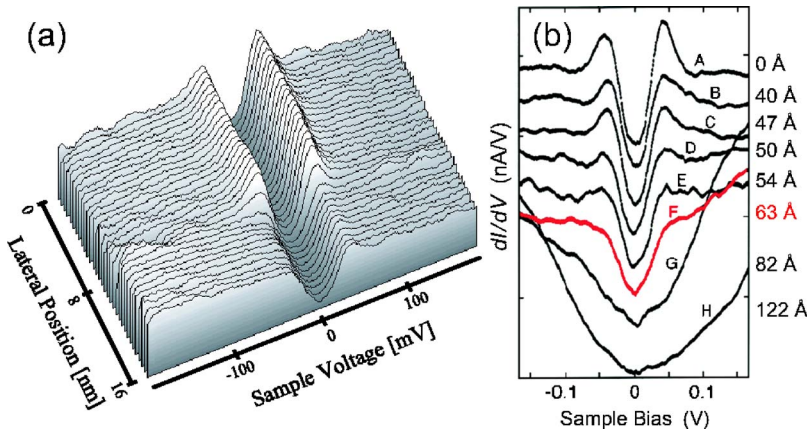
FIG. 31. (Color online) Pseudogap on disordered Bi2212 surfaces. (a) LDOS as a function of tip position on a Bi2212 300-Å-thick film at 4.2 K. Spectra were acquired every 5 Å. From Cren *et al.*, 2000. (b) LDOS evolution through a locally damaged Bi2212 region. The values on the right indicate the distance of each spectrum relative to spectrum *A*. Adapted from Howald *et al.*, 2001.

presumably due to a local variation in oxygen concentration (McElory *et al.*, 2004).

Figure 31(a) shows the evolution of the LDOS as the tip is moved out of a superconducting region on a Bi2212 thin film (Cren *et al.*, 2000): a gap with well-defined coherence peaks abruptly changes into a spectrum with the same gap magnitude and which is identical to the one observed at $T > T_c$ and in vortex cores. Moving further away from this pseudogapped zone, the spectra finally become semiconductorlike [not shown in Fig. 31(a)], indicating that strong disorder is indeed present. The gap-pseudogap transition occurs over roughly 10 Å, consistently with the spectral evolution across a vortex core [Fig. 30(a) and Sec. VII]. This characteristic length is of the order of ξ and sets the scale for the loss of superconducting phase coherence. Similar results were obtained on Pb-doped Bi2212 single crystals (Cren *et al.*, 2001) and on an intentionally "damaged" Bi2212 single crystal (Howald *et al.*, 2001), as shown in Fig. 31(b) (spectrum *F*). These experiments show that in strongly disordered samples superconducting and pseudogapped regions can locally coexist.

Many other experiments on native and generally UD Bi2212 surfaces also demonstrated patches with variable superconducting characteristics (Howald *et al.*, 2001; Pan *et al.*, 2001; Lang *et al.*, 2002; Kinoda *et al.*, 2003; Matsuda *et al.*, 2003; McElroy *et al.*, 2004). However, as illustrated in Fig. 32(b), these results show a central difference: instead of presenting a constant gap magnitude when crossing the limits of a patch, the coherence peaks shift to considerably higher energies; they gradually broaden and decrease in intensity to eventually end up in a PG-like DOS. This behavior is characteristic for local variations of the oxygen content, as demonstrated by Pan *et al.* (2001) [Fig. 16(d)]. In terms of the doping phase diagram, these experiments show, on a local scale, how the DOS evolves when the doping level is reduced [Fig. 32(c)]. This is in clear contrast with the observations by Cren *et al.* (2000), who found that the gap magnitude remains constant. These authors interpreted their results using a theoretical model by Huscroft and Scalettar (1998). It shows that in the presence of strong disorder the phase coherence is lost, while the pairing am-

plitude, which manifests itself as the pseudogap, is not necessarily suppressed.

The systematic study of microscopic inhomogeneities in the LDOS at different dopings on Bi2212 by McElroy *et al.* (2004) revealed that the total area showing regions with large gap values increases with underdoping. For strongly underdoped samples, regions appear where coherence peaks are absent. The authors claim that in those regions all spectra are identical to each other and that no changes are observed on further underdoping. Instead, the total area covered by such regions increases. McElory *et al.* (2004) therefore concluded that they observed a limiting class of spectra and identified it as the zero-temperature pseudogap (ZTPG). Similar spectra were observed by Hanaguri *et al.* (2004) on heavily underdoped and even nonsuperconducting $Ca_{2-x}Na_xCuO_2Cl_2$. As illustrated in Fig. 33(c), these spectra have a V-shaped gap with a broad peak at positive bias and resemble the PG spectrum described earlier, but for an extremely underdoped region, since the peak at positive bias is around 150 mV. It is suggested
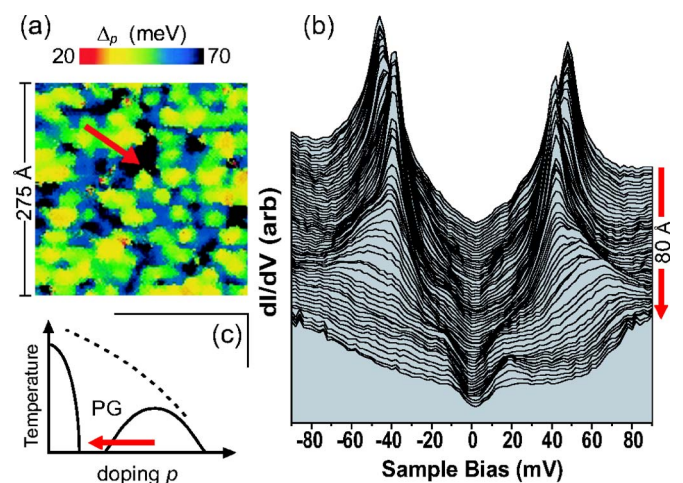

FIG. 32. (Color online) Gap inhomogeneities in Bi2212. (a) Gap map at 4.2 K and zero field acquired on a Bi2212 sample which on average is underdoped. The arrow indicates the location of the 80-Å trace shown in (b). Adapted from McElroy *et al.*, 2004. (c) Hypothesis on the local doping variation along the spectral trace.
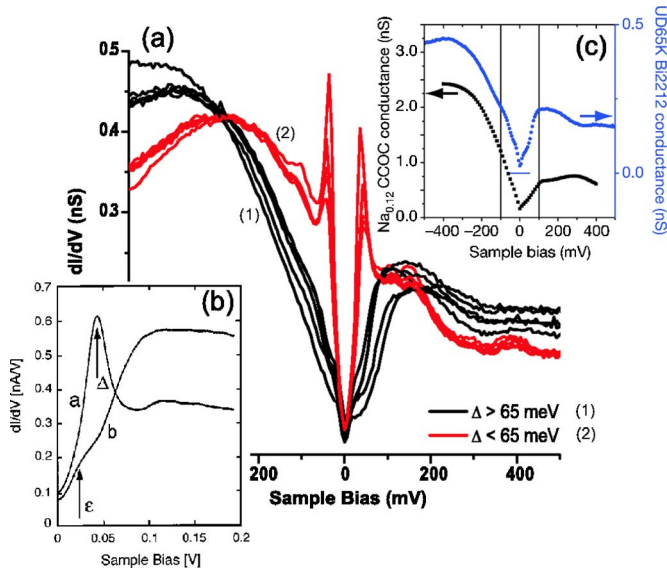
FIG. 33. (Color online) Low-energy coherence. (a) Representative spectra from nanoscale Bi2212 regions exhibiting coherence peaks (labeled 2) and from regions exhibiting the ZTPG (labeled 1) acquired at 4.2 K. From McElroy, Lee, Hoffmann, *et al.*, 2005. (b) Comparison of the positive-bias LDOS of a ZTPG and a superconducting region in Bi2212. From Howald *et al.*, 2001. (c) Comparison between spatially averaged tunneling conductance spectra on heavily UD $Ca_{2-x}Na_xCuO_2Cl_2$ (bottom curve) and equivalently UD Bi2212 (top curve). From Hanaguri *et al.*, 2004.

that these spectra characterize the DOS between the superconducting dome and antiferromagnetic phase (Hanaguri *et al.* 2004). In contrast to the T dependence of the DOS (Sec. VI.A.5) where the pseudogap and superconducting gap have the same magnitude, we emphasize that in the case described in Fig. 33(a) the ZTPG does not scale with the superconducting spectrum since it does not correspond to the same doping level: the superconducting spectra are typical of optimally or slightly underdoped regions, whereas the ZTPG spectra correspond to extremely underdoped regions. This aspect is clearly seen in Fig. 32.

These observations suggest that there exist two types of disorder that have distinct spectral signatures: (i) disorder that does not change the local doping level; hence the gap magnitudes are the same in both the superconducting and pseudogap regions; and (ii) disorder due to a locally varying oxygen concentration; hence the observed pseudogap will correspond to an extremely underdoped sample.

As first pointed out by Howald *et al.* (2001) and later by McElory, Lee, Hoffmann, *et al.* (2005), the low-energy features of the spectra shown in Figs. 33(a) and 33(b) coincide up to roughly 20 meV, above which a kink occurs in the ZTPG. This might indicate that the so-called ZTPG has two components: a first component originating from the nodal points with coherent d-wave quasiparticles at energies below the kink and a second one at higher energies with incoherent quasiparticles predominantly from the antinodal points, yielding the
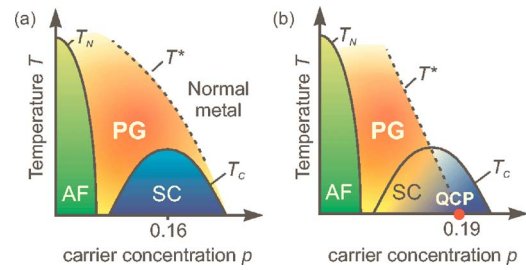

FIG. 34. (Color online) Two scenarios for the hole-doped HTS phase diagram. (a) T^* merges with T_c on the overdoped side. (b) T^* crosses the superconducting dome (SC) and falls to zero at a quantum critical point (QCP). T_N is the Néel temperature for the antiferromagnetic (AF) state.

pseudogapped envelope due to the reduced quasiparticle lifetime. Other interpretations in terms of phase separation between "good" and "bad" superconducting regions have also been proposed (Howald *et al.*, 2001; Lang *et al.*, 2002). The issue of two-component behavior is discussed in more detail in Sec. VIII in relation to the spatial modulations of the LDOS.

C. Doping phase diagram

Conventional BCS superconductors are characterized by their T_c, which is closely related to the pairing energy Δ via the coupling constant $2\Delta/k_BT_c \approx 3.5$. The phase diagram of HTS's, is much more complex (Fig. 14). The superconducting gap seems to be unrelated to T_c and a new state—the PG state—appears above T_c as discussed in the previous sections. Although it is generally accepted that the pseudogap is intimately related to the occurrence of high T_c, there is currently no consensus as to its nature [see reviews by Timusk and Statt (1999); Philips *et al.* (2003)]. Two alternative phase diagrams, depicted in Fig. 34, are generally proposed. Either T^* merges with T_c on the overdoped side or T^* crosses the superconducting dome and possibly falls to zero at a QCP.

Different scenarios can be associated with different phase diagrams. For instance, if the pseudogap were the signature of a phase-disordered d-wave superconductor, a phase diagram like the one shown in Fig. 34(a) would naturally result, although in this scenario the T^* line could also cross the superconducting dome. In the scenario that the pseudogap were a phenomenon different and largely independent of superconductivity, like a charge-density wave, it has been proposed that the dome results from competition of two phenomena: the pseudogap winning out at low doping and superconductivity at higher doping. In such a scenario it is expected that T^* would fall below T_c roughly at optimal doping and end in a QCP hidden below the dome as shown in Fig. 34(b). If this were the correct explanation, the phase diagram shown in Fig. 34(b) should be a universal phase diagram. It was in fact for a long time assumed that the pseudogap was associated with the underdoped region of the phase diagram, since this seems to be the case for
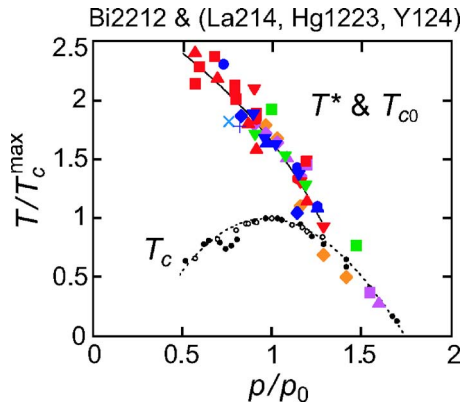
FIG. 35. (Color online) Doping phase diagrams of various hole-doped HTS cuprates. From Nakano *et al.*, 1998.

Y123. However, STS has clearly shown that for Bi2212 (Renner, Revaz, Genoud, *et al.*, 1998) and Bi2201 (Kugler *et al.*, 2001) a pseudogap exists also in overdoped samples and that the phase diagram for these compounds is of the type shown in Fig. 34(a). Therefore STS has ruled out the phase diagram in Fig. 34(b) as a universal phase diagram for HTS materials.

Although the phase diagram has not yet been investigated systematically by tunneling spectroscopy, results obtained so far and discussed in this section already allow one to draw some conclusions for Bi2212 and Bi2201: (i) the superconducting gap and pseudogap are T independent, (ii) they have the same amplitude, (iii) the PG temperature T^* increases monotonically when the compound is underdoped and scales with Δ_p, and (iv) the pseudogap clearly exists in the overdoped region. These results obtained by STS—a method which probes directly the quasiparticle DOS—give strong support to the scenario depicted in Fig. 34(a). This picture is corroborated by ARPES [see review by Damascelli *et al.* (2003), p. 520] and by various bulk techniques for several other cuprates (La214, Y124, Hg1223, and Tl2201), as shown in Fig. 35. There are compounds, however, which deviate from the diagram of Fig. 34(a). In Bi2201 phase fluctuations seem to suppress T_c even in the strongly overdoped region [Fig. 26(c)]. In the case of Y123 (Sec. VI.A.3) the superconducting gap scales with T_c (Yeh *et al.*, 2001). Furthermore, STS data at optimal doping do not reveal any clear pseudogap (Maggio-Aprile *et al.*, 2000), suggesting that the T^* line is shifted toward the underdoped side. This is consistent with early NMR experiments (Alloul *et al.*, 1989; Warren *et al.*, 1989) and with a recent high-resolution dilatometry study by Meingast *et al.* (2001). These authors showed that phase fluctuations dramatically suppress T_c from its mean-field value T_c^{MF} in UD Y123, whereas for overdoped samples $T_c \approx T_c^{MF}$. Thus T_c^{MF} exhibits a similar doping dependence as T^*, suggesting that the pseudogap in Y123 is due to phase-incoherent Cooper pairs. Particularly interesting in this regard are recent thermal conductivity measurements of Sutherland *et al.* (2005), which indicate the presence of d-wave-like nodal fermions even outside

the superconducting dome of Fig. 34(a). The presence of such nodal excitations provides strong support for the picture of the pseudogap as a superconducting ground state disordered by strong quantum phase fluctuations which nonetheless maintains a robust d-wave pairing amplitude (Franz and Tešanović, 2001). In contrast, results obtained using other bulk techniques like transport, heat capacity, and infrared spectroscopy tend to favor the QCP scenario (see, e.g., Tallon and Loram, 2001). No consensus has yet been reached on this debate, which involves the nontrivial question of what each experimental technique is effectively attributing to the pseudogap and how these characteristics are related to each other.

From the point of view of tunneling, which gives the most direct access to the pseudogap, the results discussed here for hole-doped cuprates give strong support to the idea that the pseudogap is a precursor of the superconducting gap, reflecting fluctuating or noncoherent pairs. However, in the case of electron-doped HTS's more investigations are needed to reach a general view. The data available at present have been interpreted in terms of a QCP scenario (Alff *et al.*, 2003) as briefly mentioned in Sec. VI.A.4.

D. Summary

Scanning tunneling spectroscopy allowed us to directly visualize the existence of a pseudogap in the high-temperature DOS of Bi2212 and Bi2201. As the temperature is raised from $T < T_c$ the superconducting gap Δ_p remains constant and smoothly evolves into a pseudogap across T_c. Coherence peaks are abruptly reduced at T_c, giving rise to a generic PG spectrum. Above T_c, the pseudogap is gradually filling up and remains essentially constant, with an apparent tendency to increase at higher temperature before vanishing at the crossover temperature T^*.

The generic PG spectrum measured at T_c in Bi2212 presents the following hallmarks: (i) the pseudogap and superconducting gap have a comparable magnitude and scale with each other as a function of doping, (ii) the coherence peak at negative bias is completely suppressed, (iii) the coherence peak at positive bias is reduced and shifts to slightly higher energies, and (iv) the zero-bias conductance is increased. Furthermore, (v) this PG spectrum is observed on both underdoped and overdoped samples and (vi) the PG temperature T^* scales with Δ_p for all doping levels. These characteristics are common to Bi2212 and Bi2201 in spite of their radically different superconducting parameters. Furthermore, the PG signature is also observed at low temperatures in vortex cores and on disordered samples, where phase coherence is reduced or suppressed. Finally, it appears that for several HTS cuprates the values of T^* and Δ_p measured by STS roughly obey the d-wave BCS scaling law $2\Delta_p/k_B T^* = 4.3$, consistent with other experimental techniques.

VII. IMAGING OF VORTEX-MATTER AND -CORE STRUCTURE BY STS

A vortex-state study provides direct access to the fundamental properties of superconductors. The electronic structure of vortex cores, as well as the interaction between the flux lines, is intimately connected with the nature and behavior of charge carriers. STS offers unique capabilities for investigating these properties. STS provides a way to detect the individual flux lines and visualize the vortex distribution in real space, as well as the structure of cores. In addition, the probe can access electronic excitations within cores, revealing important and often unexpected properties of superconducting pairing states.

Ten years after the theoretical prediction of type-II superconductivity by Abrikosov (1957), real-space imaging of vortices was achieved using Bitter decoration in lead (Essmann and Träuble, 1967). Various techniques of vortex imaging in real space have been developed since then, all relying on the magnetic field generated by flux lines and hence restricted to relatively low fields. In the case of extreme type-II superconductors like HTS's, where the penetration depth λ amounts to hundreds of nanometers, the magnetic imaging contrast starts to be damped at fields not exceeding H_{c1} by very much.

A breakthrough occurred when Hess *et al.* (1989) used STS to map the vortex lattice of $NbSe_2$ by detecting systematic spatial variations of the tunneling conductance. Since the latter occur over distances of the order of the coherence length ξ around the vortex center, this technique can in principle be used up to fields where cores start to overlap, i.e., H_{c2}. In practice, because of the cores small size, the relatively slow sampling, and the limited field of view of the instrument, vortex imaging by STS should be considered as a complementary tool to other vortex-mapping techniques, especially at very low fields or in the case of vortex-dynamics studies.

This section will start with a brief overview of vortex-matter studies by STS. The focus will then be on the specific electronic signature of vortex cores. One of the most important observations is that vortex cores in Bi2212 exhibit pseudogaplike spectra, revealing the non-BCS character of superconductivity in this compound. The existence of low-energy discrete states in both Y123 and Bi2212 is another surprising property of the cores. The properties of vortices in conventional BCS superconductors will also be presented, in order to establish comparisons with the electronic signatures found in HTS's.

A. Vortex-matter imaging by STS

STS imaging of vortices relies on the fact that their cores affect the quasiparticle excitation spectra. Images are usually obtained by mapping the tunneling conductance in real space at a particular bias voltage (see Sec. II). The imaging contrast depends upon the chosen bias voltage, since spatial variations of the tunneling conductance close to the vortex are usually energy dependent.
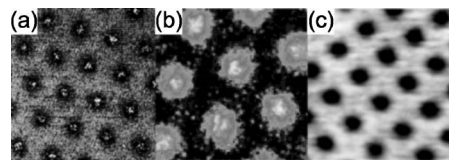

FIG. 36. STS images of ordered vortex lattices in conventional superconductors. (a) 400×400 nm^2 hexagonal lattice in $NbSe_2$ ($T=1.3$ K, $H=0.3$ T). From Renner *et al.*, 1991. (b) 250×250 nm^2 hexagonal lattice in MgB_2 ($T=2$ K, $H=0.2$ T). From Eskildsen *et al.*, 2002. (c) 170×170 nm^2 square lattice in $LuNi_2B_2C$ ($T=4.2$ K, $H=1.5$ T). From DeWilde, Iavarone, Welp, Metlushko, Koshelev, Aranson, Crabtree, Gammel, *et al.*, 1997. The mapping energy was Δ_p for (a) and (c) and 0 for (b), explaining the inverted contrast.

Consequently, the visual aspect of vortex cores in the images depends on the mapping energy. The performance of the technique is also inherently related to the quality of the sample surfaces, since spectroscopic signatures of superconductivity are easily affected by a nonadequate surface layer (Sec. IV). Inhomogeneities like structural defects, chemical adsorbates, impurities, or electronic inhomogeneities will generally perturb the detection of individual vortices.

Vortex imaging by STS finds an obvious interest in the study of the spatial distribution of flux lines. Most conventional superconductors have an isotropic BCS order parameter, and when pinning is not effective, vortices are arranged in a regular lattice. When pinning is more relevant, vortex lattices become disordered. The STS observation of flux lines on BCS compounds confirms these expectations. In addition, STS imaging provides information on the shape of the cores. Both pieces of information give direct access to the anisotropy of the superconducting state.

Because obtaining surfaces with homogeneous electronic characteristics is difficult, vortex imaging by STS has been achieved on only a few materials, essentially conventional superconductors. The degradable surfaces and very small coherence lengths of HTS's imply that their superconducting spectral characteristics may be affected by the nature of the topmost layer. Technological developments allowing the synthesis of large and ultrapure single crystals largely contributed to recent breakthroughs in spectroscopic studies and vortex imaging of some HTS's.

1. NbSe$_2$ and other conventional superconductors

With easily cleavable planes and a reasonably high T_c (7.2 K), $NbSe_2$ is an ideal candidate for vortex studies using STS. The first experiments of Hess *et al.* were followed by many other studies (Renner *et al.*, 1991; Behler *et al.*, 1994).

The standard way to detect vortices in $NbSe_2$ is to map the conductance measured at the energy of the coherence peaks. An example is shown in Fig. 36(a) revealing vortices arranged into a perfect hexagonal lattice with a lattice parameter of ~90 nm. The expected inter-

vortex spacing is $a_\Delta = (2\Phi_0/\sqrt{3}H)^{1/2} = 48.9/\sqrt{H(\mathrm{T})}$ nm, yielding $a_\Delta = 89$ nm for $H = 0.3$ T. Since the magnetic profile of a single flux line in Fig. 36(a) extends over about one-quarter of the total image, techniques sensitive to the magnetic field would be, with the same conditions, incapable of distinguishing individual vortices. The vortex cores look isotropic with an apparent radius of 15–20 nm, larger than the coherence length of $NbSe_2$, estimated to be 7.7 nm from critical field anisotropy measurements (de Trey *et al.*, 1973).

The relatively long acquisition times do not preclude vortex dynamics studies by STS, provided that the flux line motion is sufficiently slow. Renner (1993) observed vortices with an elongated shape due to slow motion of the lattice during the line by line scanning of the tip. After some time, this motion stopped and the vortex cores appeared perfectly isotropic. More recently, much faster vortex imaging was achieved by controlling the tip position, without interrupting the feedback loop, using a voltage close to the gap energy rather than the commonly used biases in the CITS technique (Troyanovski *et al.*, 1999, 2002).

Disordered lattices in irradiated $NbSe_2$ samples illustrated the pinning of vortices by columnar defects (Behler *et al.*, 1994). This observation was helped by the fact that the coherence length in $NbSe_2$ is much larger than the size of the defects. When the cores and defects have similar sizes, the spectroscopic signatures of the cores may be masked by defects and thus difficult to distinguish [see, e.g., Zn-doped Bi2212 by Pan, Hudson, Gupta, *et al.* (2000)].

A hexagonal vortex lattice was also seen in MgB_2 single crystals, as shown in Fig. 36(b) (Eskildsen *et al.*, 2002). The expected vortex spacing of 109 nm is readily verified in the image. More surprisingly, DeWilde, Iavarone, Welp, Metlushko, Koshelev, Aranson, Crabtree, and Canfield (1997) found a square vortex lattice in the borocarbide $LuNi_2B_2C$ [Fig. 36(c)] at a field of 1.5 T. The expected spacing for a square lattice, $a_\square = (\Phi_0/H)^{12} = 45.5/\sqrt{H(\mathrm{T})}$ nm, is again respected (37 nm at 1.5 T). The square symmetry was explained using a Ginzburg-Landau theoretical approach, considering a fourfold perturbation term in the free energy arising from the underlying tetragonal structure of the crystal (DeWilde, Iavarone, Welp, Metlushko, Koshelev, Aranson, Crabtree, Gammel, *et al.*, 1997). A transition from a distorted hexagonal lattice at low fields to a square lattice at high fields was predicted and experimentally confirmed by small-angle neutron scattering (Eskildsen *et al.*, 1997). Later this transition was directly observed by STS in another borocarbide compound YNi_2B_2C (Sakata *et al.*, 2000) and in the cubic $A15$ compound V_3Si (Sosolik *et al.*, 2003).

2. High-temperature superconductors Y123 and Bi2212

The behavior of vortices in HTS cuprates differs radically from what is observed in BCS superconductors. At first sight, high T_c's and large superconducting gaps make them ideal compounds for STS, since for most of
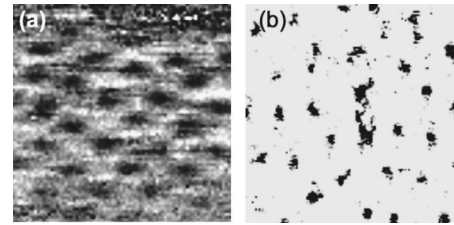

FIG. 37. 100×100 nm^2 STS images of (a) a slightly disordered oblique lattice in Y123 (from Maggio-Aprile *et al.*, 1995) and (b) a disordered vortex distribution in Bi2212 (from Hoogenboom *et al.*, 2001). Both images were acquired at $T = 4.2$ K and $H = 6$ T. The contrast is defined by the conductance measured at the gap energy (20 meV for Y123 and 30 meV for Bi2212) normalized by the zero-bias conductance.

them the electronic characteristics can be probed at 4.2 K or above and the characteristic DOS features are situated at relatively high energies. But because of difficulties in preparing surfaces with sufficient homogeneity, the study of vortices by STS remained a considerable challenge. Up to now, imaging of vortices has been possible only in Y123 and Bi2212. The very small coherence length in these materials has two direct observable implications. First, the vortex cores are tiny in comparison to conventional superconductors and thus difficult to localize. Second, the vortices are easily pinned by defects. As a consequence, at the relatively high fields that are suitable for STS, flux-line lattices show no perfect order in HTS's.

Examples of vortices imaged with STS in a 6-T field in both Y123 and Bi2212 are presented in Fig. 37. In Y123 the vortices arrange in a slightly disordered oblique lattice [Fig. 37(a)]. In Bi2212 they are more disordered [Fig. 37(b)]. Note that the entire scan range of Fig. 37 fits into a single vortex core of Fig. 36(b), graphically illustrating the small size of the cores in HTS's.

a. Y123

Y123 was the first nonconventional superconductor whose vortex lattice could be investigated by STS, and this was achieved by Maggio-Aprile *et al.* (1995) on as-grown surfaces. Since then, two other groups reported the STS observation of flux lines in Y123, either on as-grown surfaces (Hubler *et al.*, 1998) or on chemically etched surfaces (Shibata *et al.*, 2003b). Figure 38(a) shows an image acquired in optimally doped Y123 ($T_c = 92$ K). The observed vortex density matches the 6 T applied field. The lattice shows a local oblique symmetry, with an angle of about 77°. Vortex cores reveal an apparent radius of about 5 nm, but systematically present an elliptical shape with an axis ratio of about 1.5 [see Fig. 38(a)]. Maggio-Aprile *et al.* (1995) noticed that this distortion is independent of scanning direction and not related to any flux-line motion, and they ascribed it to the *ab*-plane anisotropy of Y123.

In the framework of an anisotropic Ginzburg-Landau model, the observed oblique lattice in Y123 can be interpreted as a square lattice distorted by an anisotropy
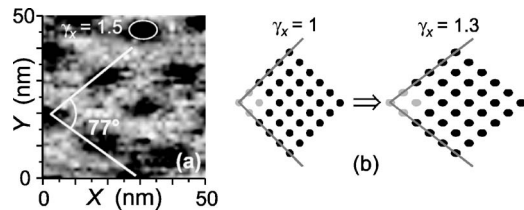
FIG. 38. Oblique vortex lattice in Y123. (a) 50×50 nm^2 STS image of vortices in Y123. The primitive vectors of the oblique lattice form an angle of 77°, and the cores present an elliptic distortion of about 1.5 ratio. (b) Schematic diagram showing the formation of an oblique lattice, starting from a square lattice distorted by an anisotropy factor of 1.3. Adapted from Renner *et al.*, 1996.

factor of ~1.3 or as a hexagonal lattice distorted by an anisotropy factor of ~2.2. Since it is expected that the anisotropy controlling the distortion of the lattice is also responsible for the intrinsic distortion of the cores, the observed value of ~1.5 for the latter led Renner *et al.* (1996) to conclude that the lattice corresponds to a deformed square lattice as illustrated in Fig. 38(b). Similar anisotropy factors have been derived from penetration depth measurements in Y123 (Zhang *et al.*, 1994). At analogous magnetic fields, neutron scattering measurements showed similar distortions (Keimer *et al.*, 1994). More recent neutron scattering investigations evidenced a continuous transition from a distorted hexagonal to a nearly perfect square lattice at high fields (Brown *et al.*, 2004). Square vortex lattices can be expected in a number of situations where a fourfold perturbation field acts. In particular, a square lattice was predicted for *d*-wave superconductors (Won and Maki, 1995; Affleck *et al.*, 1997). It is not yet clear whether the tendency to order into a square lattice at high field is due to the *d*-wave symmetry of the order parameter or to other factors. On the other hand, Bitter decoration measurements at low fields revealed a regular (Gammel *et al.*, 1987; Vinnikov *et al.*, 1988; Dolan, Chandrashekhar, *et al.*, 1989) or slightly distorted (Dolan, Holteberg, *et al.*, 1989) hexagonal lattice, as expected at low vortex density.

The disorder observed in the vortex lattice underlines the influence of strong pinning in compounds with small coherence lengths. In Y123, a substantial vortex creep is observed after switching on the magnetic field, with flux lines continuously moving for a couple of days. The influence of twin boundaries on pinning in Y123 single crystals has stimulated various debates and investigations (Gammel *et al.*, 1992; Vlasko-Vlasov *et al.*, 1994; Welp *et al.*, 1994; Crabtree *et al.*, 1996; Herbsommer *et al.*, 2000). STS measurements demonstrate that the twin boundaries act as very efficient barriers, blocking the movements of flux lines perpendicular to the twin plane. This phenomenon is illustrated in Fig. 39(a), which shows vortices mapped out in a field of 3 T on both sides of a twin boundary (Maggio-Aprile *et al.*, 1997), seen as the dark line running along the [110] direction. Vortices are found on both sides with the same average density. The anisotropic shape of the cores is rotated by 90° be-
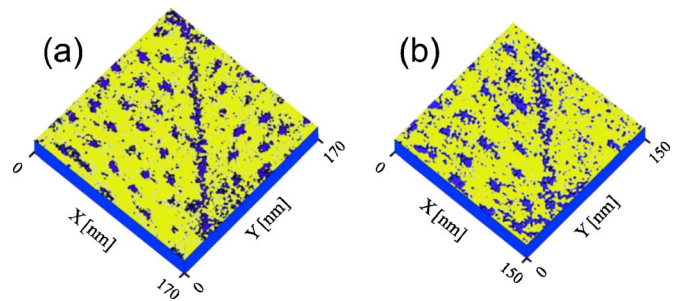

FIG. 39. (Color online) STS observation of a twin boundary in Y123. (a) 170×170 nm^2 image at $H = 3$ T; the flux lines are distributed on both sides of the boundary with an equal density. (b) After reducing the field to 1.5 T, the flux lines pile up on the left domain and reach a density corresponding to about 2.5 T. From Maggio-Aprile *et al.*, 1997.

tween the two domains, demonstrating that the dark line separates two regions with inverted *a* and *b* crystallographic axes. The field was then reduced to 1.5 T, and a piling up of flux lines on the left side of the twin boundary was observed, corresponding to a field of 2.5 T, substantially higher than the applied field. The right side showed a vortex-free region extending over more than 100 nm [Fig. 39(b)]. The gradients of the magnetic field could be directly measured from the flux-line distribution and allowed the authors to estimate a current density close to the depairing current limit for Y123 (~3 $\times 10^8$ A/cm^2). The dark line on the twin boundary was attributed to trapped vortices, too densely packed or mobile to be resolved.

b. Bi2212

In Bi2212, the quasiparticle spectra taken outside and inside the vortex cores show rather small differences (see Fig. 30). Renner, Revaz, Kadowaki, *et al.* (1998) imaged for the first time vortices in overdoped Bi2212 using negative energies. As seen in Fig. 40(a) the cores in Bi2212 are tiny, consistent with a coherence length of the order of a few atomic unit cells. They usually exhibit irregular shapes (see Sec. VII.C.2).

In the STS images, vortices are distributed in a totally disordered manner, but with an average density matching the 6-T field (Renner, Revaz, Kadowaki, *et al.*, 1998). This can be understood since Bi2212, unlike Y123, has a nearly two-dimensional electronic structure and vortices
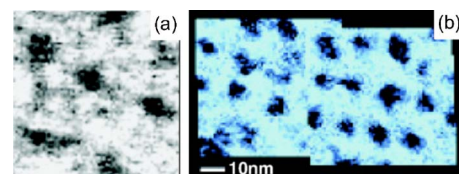

FIG. 40. (Color online) STS images of vortices in Bi2212. (a) 40×40 nm^2 image of vortex cores in overdoped Bi2212 at $H = 6$ T. From Renner, Revaz, Kadowaki, *et al.*, 1998. (b) Ordered phase at $H = 8$ T, revealing a nearly square symmetry. From Matsuba, Sakata, Kosugi, *et al.*, 2003.
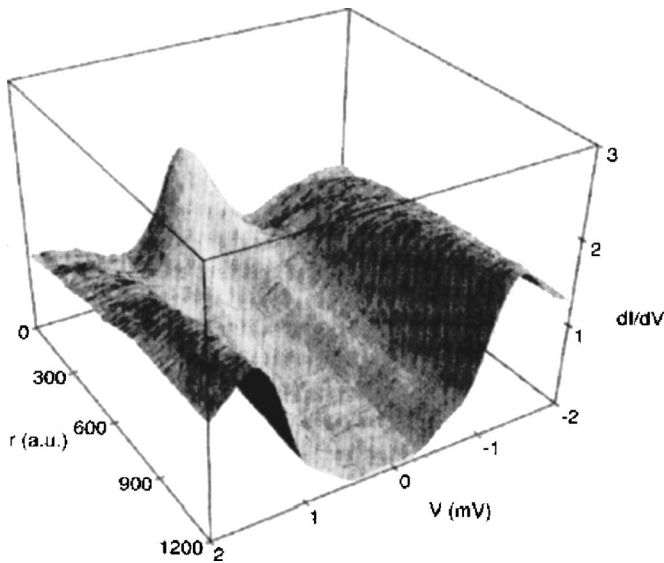
FIG. 41. Conductance spectra acquired at $T=0.3$ K, $H=0.05$ T along a 50-nm path leading from the center ($r=0$) to the outside ($r=1200$) of a vortex core in NbSe$_2$ (Hess *et al.*, 1990). The splitting of the zero-bias peak into one electron and one hole branch shows the presence of many bound states in the core (see text). From Gygi and Schlüter, 1991.

are therefore constituted of a stack of 2D elements (pancakes), weakly coupled between adjacent layers, and easily pinned by any kind of inhomogeneity. The observed disordered lattice fits into the commonly accepted vortex phase diagram for Bi2212, where the low-temperature high-field region is associated with a disordered vortex solid. At very low fields an ordered Bragg glass phase appears, which is difficult to probe with STS because of the large intervortex distances. At 8 T, however, Matsuba, Sakata, Kosugi, *et al.* (2003) observed a short-range ordered phase in Bi2212, presenting a nearly square symmetry almost aligned with the crystallographic *ab* directions [Fig. 40(b)].
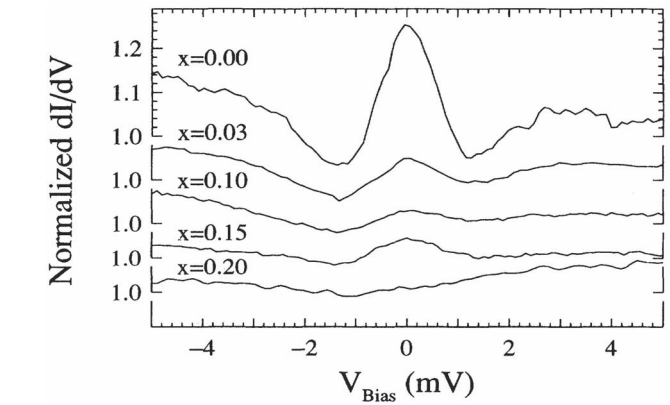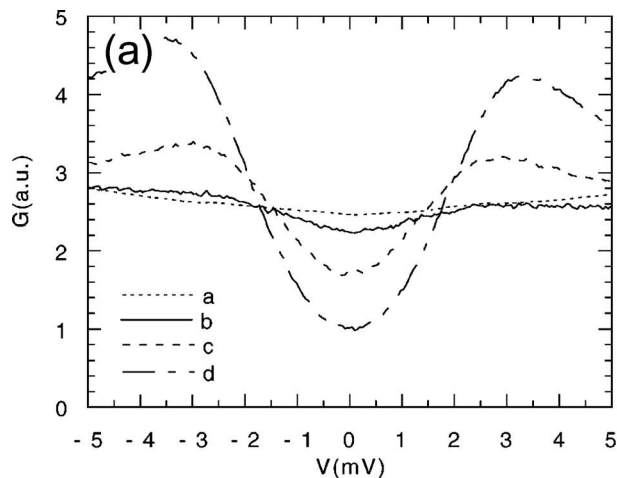

FIG. 42. Tunneling conductance spectra acquired at the vortex-core center of Nb$_{1-x}$Ta$_x$Se$_2$ at $T=1.3$ K and $H=0.3$ T for different impurity dopings x. For $x=0$ (clean limit), bound states are observed as a broad ZBCP, which progressively vanishes for larger amounts of impurities (Renner *et al.*, 1991).

B. Electronic structure of the cores

1. BCS superconductors

In 1964 Caroli, de Gennes, and Matricon provided an approximate analytical solution of the Bogoliubov–de Gennes equations for an isolated vortex in a clean *s*-wave superconductor. They predicted the existence of electronic states bound to the vortex at energies below the superconducting gap. These bound states form a discrete spectrum with a typical interlevel spacing Δ^2/E_F. For most superconductors, this spacing is so small that detection of individual bound states is hampered by the finite temperature and impurity scattering. In NbSe$_2$, Δ^2/E_F is typically ~ 0.05–0.5 K, and so far it has not been possible to resolve an ideal discrete spectrum. Instead, a strong zero-bias conductance peak (ZBCP) is observed, understood as the continuous envelope of a set of low-energy states.
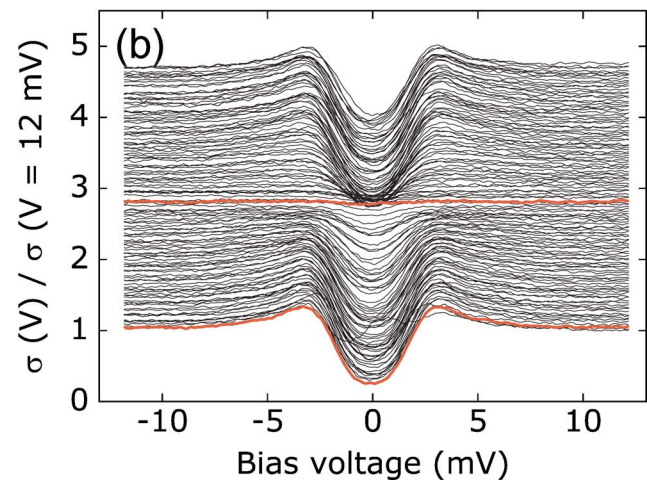

FIG. 43. (Color online) Examples of missing zero-bias peak in the vortex cores of conventional BCS superconductors. (a) Spectra acquired at 47 nm (dashed line) to the center of the core (dotted line) in LuNi$_2$B$_2$C at $T=4.2$ K and $H=1.5$ T. From DeWilde, Iavarone, Welp, Metlushko, Koshelev, Aranson, Crabtree, and Canfield, 1997. (b) 250-nm-long spectroscopic trace crossing a single vortex core in MgB$_2$ at $T=2$ K and $H=0.2$ T. From Eskildsen *et al.*, 2002.
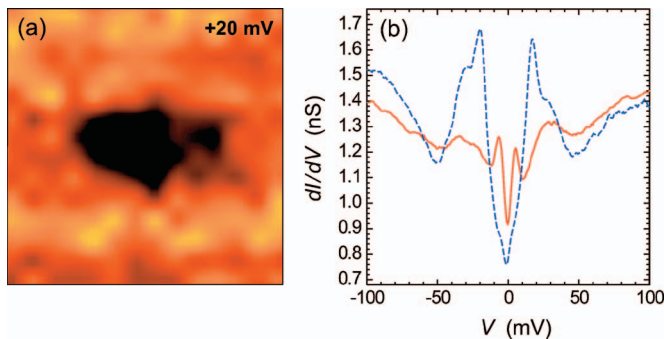
FIG. 44. (Color) Core states in Y123. (a) 20×20 nm^2 conductance map acquired at +20 mV, showing a detailed view of a vortex core ($T=4.2$ K, $H=6$ T). (b) Conductance spectra acquired at the center (red) and at about 20 nm from the center of the vortex core (dashed blue). The low-energy core states are located at about ±5.5 meV. Adapted from Maggio-Aprile *et al.*, 1995.

Hess *et al.* (1989) studied vortex cores by STS in pure NbSe$_2$ single crystals at $T=1.85$ K and observed features in agreement with theoretical expectations (Shore *et al.*, 1989). The progressive splitting of the ZBCP at a distance r from the center provided another verification of the BCS predictions for vortex cores in *s*-wave superconductors (Fig. 41). This splitting reflects the presence of many core states with different angular momenta μ. The lowest-lying state $\left(\mu=\frac{1}{2}\right)$ has energy $E_{1/2}=\frac{1}{2}\Delta^2/E_F \approx 0$ and maximum probability at $r=0$, giving rise to the ZBCP at the vortex center. The energy of higher-angular-momentum vortex states departs from zero as $E_\mu=\mu\Delta^2/E_F$ at low μ (Caroli *et al.*, 1964), and these states have maximum amplitude at a distance $r=r_\mu \approx |\mu|/k_F$ from the core center. In the LDOS, these latter states show up as one electron branch ($E_\mu>0$) and one hole branch ($E_\mu<0$) at energy E_μ and position r_μ. With increasing $|\mu|$, the electron and hole branches approach the gap edges at $\pm\Delta$ and merge asymptotically with the continuum of scattering states with energies $|E|>\Delta$. Thus the superconducting spectrum is eventually recovered outside the core, at $r=(5-10)\xi$. These observations were successfully described by a complete numerical solution of the Bogoliubov–de Gennes equations for an isolated *s*-wave vortex (Gygi and Schlüter, 1990b, 1991).

In dirty superconductors, quasiparticle scattering mixes states with different angular momenta and the zero-bias peak transforms into a quasinormal (flat) DOS spectrum when the quasiparticle mean free path is smaller than the coherence length. This effect was observed by STS in Ta-doped NbSe$_2$ (Renner *et al.*, 1991), as shown in Fig. 42. The spectra were acquired in different Nb$_{1-x}$Ta$_x$Se$_2$ samples, each doped with a specific amount of tantalum. As seen in the figure, the low-energy spectra taken at the core center progressively lose the pronounced zero-bias feature and for dopings $x>0.15$ show a nearly constant conductance reminiscent of the normal-state DOS.
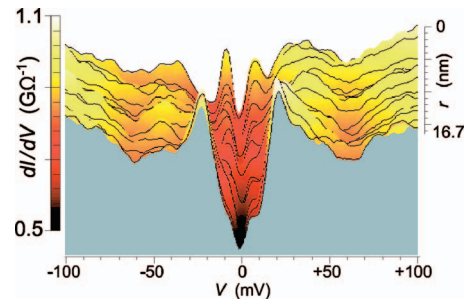

FIG. 45. (Color) Conductance spectra taken along a 16.7-nm path into a vortex core in Y123 at $T=4.2$ K and $H=6$ T. Together with the vanishing of the 20-mV coherence peaks, a pair of low-energy peaks emerges when the tip approaches the center of the vortex core ($r=0$). From Renner, Revaz, Kadowaki, *et al.*, 1998.

DeWilde, Iavarone, Welp, Metlushko, Koshelev, Aranson, Crabtree, and Canfield (1997) reported similar vortex-core spectra for LuNi$_2$B$_2$C [Fig. 43(a)], with a nearly constant tunneling conductance. Recently Nishimori *et al.* (2004) reported the observation of a zero-bias peak in pure samples of this compound. In the two-band superconductor MgB$_2$, the vortex-core spectra acquired on the (001) surface show also a totally flat conductance [Eskildsen *et al.*, 2002, Fig. 43(b)]. This observation is more surprising, since the mean free path in MgB$_2$ is believed to be much larger than the superconducting coherence length. The absence of a zero-bias peak was attributed to the fact that the π band is predominantly probed in this geometry. Since this band becomes superconducting through coupling with the σ band, the presence of a flux line, suppressing the superconducting character of the σ band, also affects the π band, which becomes metallic, with an energy-independent DOS (Eskildsen *et al.*, 2002).

2. High-temperature superconductors

a. Y123

The predictions and experimental confirmations of core bound states in BCS *s*-wave superconductors raised important questions when exotic properties of HTS's were uncovered. Among these, the question of the elec-
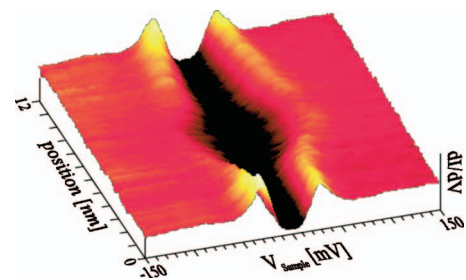

FIG. 46. (Color) Conductance spectra taken along a 12-nm path across a vortex core in overdoped Bi2212 ($T_c=77$ K) at $T=2.6$ K and $H=6$ T. The spectra acquired at the center of the core reveal a pseudogaplike shape similar to the one observed above T_c. From Kugler, 2000.
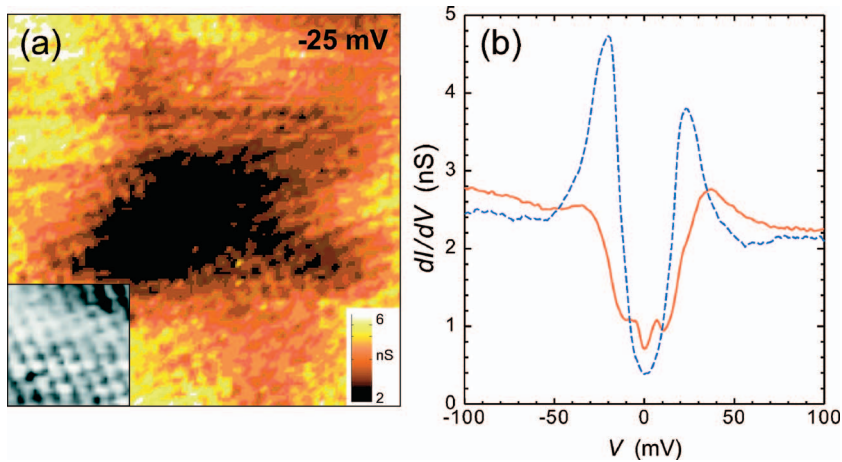
FIG. 47. (Color) Core states in Bi2212. (a) 8.7×8.7 nm^2 conductance map of a vortex core in Bi2212, acquired at -25 mV and 6 T. Inset: The simultaneously acquired topography at the same scale. (b) Spectra taken close to the core center with two peaks at ± 6 meV corresponding to a pair of core states (red) and outside the vortex core (blue). Adapted from Levy *et al.*, 2005.

tronic signature of vortex cores in HTS's was at the time completely open. The first answers came from measurements on optimally doped Y123 single crystals by Maggio-Aprile *et al.* (1995). Figure 44(a) shows a tunneling conductance map of a vortex recorded at an energy close to the positive coherence peak and illustrates the suppression of the latter in the core region. The most striking observation comes from the conductance spectrum at the core center [Fig. 44(b)]. Contrary to the case of conventional superconductors, the core spectra in Y123 reveal neither any broad zero-bias feature nor a flat conductance. Instead, a pair of low-energy peaks clearly emerging above the conductance background is observed at an energy of about ± 5.5 meV. While both coherence peaks near ± 20 meV disappear inside the core, a broad feature of reduced intensity persists at slightly higher energies (30–40 meV).

The observation of isolated core states at finite energy in Y123 appeared contradictory in various respects. On the one hand, attempts to interpret the observed bound states like classical BCS *s*-wave localized states failed for two reasons: first, it would imply an unusually small Fermi energy ($E_F \sim 36$ meV); second, there is a complete absence of energy dispersion at different positions within the core (Fig. 45). When the tip starts entering the core ($r = 16.7$ nm), the 20-meV coherence peaks progressively vanish and low-energy core states develop while the tip approaches the core center ($r = 0$). The energy at which core states are observed does not vary, indicating that only one pair of localized states exists below the gap. Note that a weak low-energy structure persists in the spectra outside the vortex cores [see spectrum at $r = 16.7$ nm in Fig. 45 and the dashed spectrum in Fig. 44(b)]. A similar structure also exists in the absence of a magnetic field (see Sec. V). Although the energy of this structure observed outside the cores is approximately the same as the core state energy, the question of its origin and the relation it has with the core state is still open.
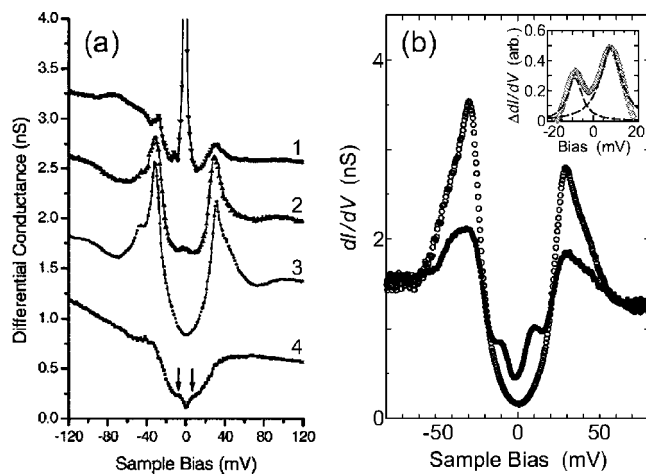

FIG. 48. STS measurements of vortex-core states in Bi2212. (a) Tunneling spectra acquired in various sites of Zn-doped Bi2212 samples, reflecting strong (1) and weak (2) impurity scattering resonances, defect-free superconducting (3), and vortex-core (4) spectra. In the latter case, arrows indicate the position of low-energy core states. Adapted from Pan, Hudson, Gupta, *et al.*, 2000. (b) Tunneling spectra taken in a vortex core showing localized states at ± 9 meV (solid circles) and outside a vortex core (open circles). From Matsuba, Sakata, Kosugi, *et al.*, 2003.

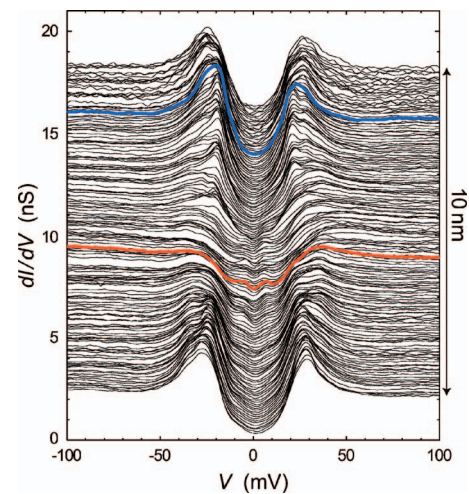FIG. 49. (Color) 10-nm-long spectroscopic trace across a vortex in overdoped Bi2212, at $T = 1.8$ K and $H = 6$ T. Core-state peaks lie at ± 6 meV, and their position does not change across the vortex (Levy, 2005).

On the other hand, this observation does not fit with the *d*-wave character of cuprate compounds. Following the observation of anomalous core spectra in Y123, an important effort was dedicated to calculating the quasiparticle spectra in vortex cores of *d*-wave superconductors, where the presence of nodes in the order parameter changes the properties of low-energy excitations. Based on the Bogoliubov–de Gennes (Soininen *et al.*, 1994; Wang and MacDonald, 1995; Morita *et al.*, 1997b; Franz and Tešanović, 1998; Yasui and Kita, 1999) or Eilenberger (Ichioka *et al.*, 1996, 1999) equations, it was shown that the vortex-core energy spectrum is continuous rather than discrete and that quasiparticles in the core are not exponentially localized as in *s*-wave superconductors. The theoretical LDOS at the center of the core shows a broad peak at zero energy.

Therefore the observation of discrete states at finite energy is in contradiction with the *d*-wave BCS picture. A possible magnetic origin of these states has been ruled out because (i) the Zeeman splitting can be estimated to be about 10 times smaller than the measured energy of the states and (ii) the peak energy position was found to be independent of the applied magnetic field. Finite-energy core states in Y123 were confirmed in more recent STS studies by Shibata *et al.* (2003b). Infrared absorption measurements (Karraï *et al.*, 1992) also clearly identified the existence of low-energy quasiparticle excitations, in quantitative agreement with all STS observations.

b. Bi2212

Vortex-core spectroscopy in Bi2212 provided new insights into the debate concerning the origin of the pseudogap, starting with the STS measurements of Renner, Revaz, Kadowaki, *et al.* (1998) on both underdoped and overdoped Bi2212 single crystals. The evolution of the spectra across a vortex core in overdoped Bi2212 is shown in Fig. 46. When entering the core, the spectra evolve in the same way as when the temperature is raised above T_c: the coherence peak at negative energy vanishes over a very small distance, the coherence peak at positive energy is reduced and shifts to slightly higher energies, and the dip-hump features disappear. The observation of such pseudogaplike spectra in the cores of Bi2212 is discussed in Sec. VI.

While the first vortex-core investigations in Bi2212 focused on pseudogap aspects, Hoogenboom, Renner *et al.* (2000) and Pan, Hudson, Gupta, *et al.* (2000) showed that weak low-energy structures were also present in vortex-core spectra. Figure 47(a) shows a spectroscopic image, mapped out at −25 meV, of a vortex core in slightly overdoped Bi2212. The full conductance spectra taken inside and outside the core are shown in Fig. 47(b). Contrary to Y123, where peaks clearly emerge in the core center, core states appear in Bi2212 as weak peaks in an overall pseudogaplike spectrum. For slightly overdoped Bi2212, the energy of these states is of the order of ±6 meV. A slight increase of the zero-bias con-

ductance is also systematically measured in the core center.

Various studies reported the observation of such states in Bi2212. Pan, Hudson, Gupta, *et al.* (2000) observed that vortices sitting away from impurity sites show core spectra with the low-energy gapped structure, as indicated with arrows in the bottom curve of Fig. 48(a). These spectra are compared with the ones acquired on strong or weak impurities shown in the top two curves of Fig. 48(a), where vortices are likely to be pinned. As a consequence, they deduce that the pair of localized states reflects an intrinsic character of the vortex cores. The systematic presence of core states in Bi2212 at different oxygen dopings was also reported by Matsuba, Sakata, Kosugi, *et al.* (2003), as shown in Fig. 48(b). They observed an asymmetry of the peak heights, which they attributed to positively charged vortices.

Hoogenboom, Renner, *et al.* (2000) investigated various samples where a large number of vortices showed the low-energy structures, measured at an energy independent of the position within the core, as shown in Fig. 49. We stress that later investigations (Levy *et al.*, 2005) showed that the intensity of the core-state peaks depends on the precise measurement position within the core (see Sec. VIII.C).

Low-energy core states observed in both Y123 and Bi2212 raise two important questions. Are the core states observed in Y123 and Bi2212 of the same origin? And how can these core states be understood within the framework of a *d*-wave symmetry of the order parameter? In order to answer the first point, detailed core spectra studies were carried out in both Y123 and Bi2212. One first notes that the spectra acquired in both Y123 and Bi2212 cores present a similar shape. In addition, although they are much more pronounced in Y123, the low-energy structures behave similarly in both types of compounds: they do not disperse when measured at various distances from the center of the core (Figs. 45 and 49) and they are magnetic field independent (Maggio-Aprile *et al.*, 1995; Hoogenboom *et al.*, 2001). The most striking fact comes from the scaling between the energy of the core state E_{core} and the superconducting gap amplitude Δ_p, as shown in Fig. 50. The correlation found between E_{core} and Δ_p for Y123 (optimal doping) and Bi2212 (various dopings) strongly suggests that the core states in the two compounds have a common origin. Moreover, since this correlation is linear (with a slope of about 0.3), the interpretation of these bound states as Caroli, de Gennes, and Matricon states of an *s*-wave superconductor with a large gap to Fermi energy ratio can be ruled out, as one would expect a Δ_p^2 dependence.

Many theoretical studies were undertaken in order to explain the observed electronic signatures of vortex cores in HTS. The absence of a large ZBCP at the vortex center in Y123 and Bi2212 has been tentatively attributed to an anisotropic tunneling matrix element (Wu *et al.*, 2000). The general belief, however, is that the qualitative difference between vortex-core spectra measured by STM in HTS's and spectra expected for a
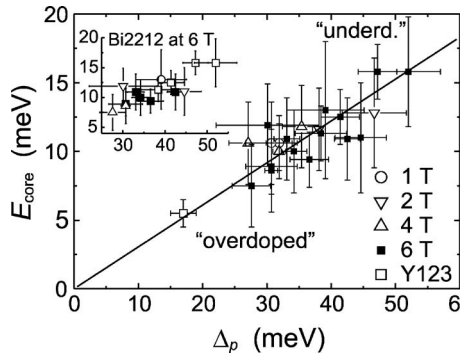
FIG. 50. Energy of vortex-core states E_{core} as a function of the superconducting gap Δ_p. Shown are Bi2212 single crystals of various dopings and optimally doped Y123 at different magnetic fields. The solid line, with a slope of 0.3, is a linear fit to all Bi2212 data points. Inset: Data for Bi2212 samples with different T_c, at a fixed field of 6 T (Hoogenboom, Renner, *et al.*, 2000).

d-wave BCS superconductor (Soininen *et al.*, 1994; Wang and MacDonald, 1995; Franz and Tešanović, 1998) reflects an intrinsic property of the superconducting ground state, which distinguishes this state from a pure BCS ground state and is presumably related to the anomalous normal (pseudogap) phase. Franz and Tešanović (1998) showed that the admixture of a small magnetic-field-induced complex component with d_{xy} symmetry (Laughlin, 1998) leads to a splitting of the ZBCP due to the suppression of *d*-wave gap nodes; as noted by the authors, this interpretation would imply a strong field dependence of the vortex-core spectra, in contradiction with the observation in Bi2212 (see Fig. 50). The effect of an antiferromagnetic order nucleated at the vortex core was investigated within the SO(5) theory (Arovas *et al.*, 1997; Andersen *et al.*, 2000) and the Bogoliubov–de Gennes mean-field framework (Zhu and Ting, 2001b). Both approaches lead to a suppression of the ZBCP at the core center; in the latter model, two symmetric core-state peaks are found when on-site repulsion is sufficiently large. Some calculations based on the *t-J* model have predicted a splitting of the ZBCP at low doping due to the formation of an *s*-wave component in the order parameter (Himeda *et al.*, 1997; Han and Lee, 2000; Tsuchiura *et al.*, 2003). A similar conclusion was reached by Chen and Ting (2002) who investigated the formation of spin- and charge-density waves around the vortex and their effect on the spectrum in the core. The structure of the vortex was also studied within the staggered-flux (Kishine *et al.*, 2001) or *d*-density-wave (Maśka and Mierzejewski, 2003) scenarios of the pseudogap. This model is able to explain the absence of ZBCP in the core, but does not seem to account for the formation of core states. Good qualitative agreement with the experimental spectra was obtained by Berthod and Giovannini (2001) using a model where short-range incoherent pair correlations coexist with long-range superconductivity in the vortex state. This model correctly reproduced the measured expo-
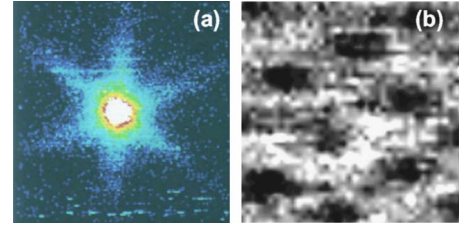

FIG. 51. (Color online) Vortex-core shapes. (a) 150×150 nm^2 zero-bias conductance map taken at $H = 500$ G and $T = 0.3$ K, revealing the sixfold shape of a vortex core in NbSe$_2$. From Hess *et al.*, 1990. (b) 50×50 nm^2 spectroscopic image of flux lines in Y123, at $H = 6$ T and $T = 4.2$ K. From Maggio-Aprile, 1996.

nential decay of the LDOS at the energy of core states (Pan, Hudson, Gupta, *et al.*, 2000), as well as the increase of the core-state energy with increasing gap Δ_p.

C. Shape of the vortex cores

The size and shape of the vortex cores mapped out by STS depend directly on how the mapping contrast is defined in the images. Since the superconducting coherence peaks at Δ_p disappear in the core, the bias $eV = \Delta_p$ is routinely selected as the mapping energy. In *s*-wave superconductors, the decay length of localized states increases to several ξ as their energy approaches the gap edge. As a consequence, vortex cores imaged at $eV = \Delta_p$ always appear larger than expected from the coherence length (Gygi and Schlüter, 1991; see Fig. 41). This is clearly the case in all spectroscopic images of flux lines presented in Sec. VII.A. Volodin *et al.* (1997) studied the core size in NbSe$_2$ as a function of the bias imaging voltage and indeed found that the apparent core size is reduced when the selected bias voltage decreases.

1. Intrinsic shape of vortices

In NbSe$_2$, detailed measurements performed at 0.3 K allowed Hess *et al.* (1990) to resolve fine structures in the imaged cores, revealing star-shaped patterns with sixfold symmetry [Fig. 51(a)]. Theoretical studies based on the Bogoliubov–de Gennes formalism and using a sixfold perturbation term were able to explain the shape of the objects (Gygi and Schlüter, 1990a). The fact that the pattern orientation depends on the mapping energy was elucidated later by Hayashi *et al.* (1996), considering an anisotropic *s*-wave pairing with a hexagonal symmetry.

In *d*-wave BCS superconductors the anisotropic order parameter leads to a fourfold anisotropy of the low-energy LDOS around vortices. The LDOS is larger in the direction of the nodes where the spatial decay of core states is slower (Morita *et al.*, 1997a; Franz and Tešanović, 1998). In the microscopic Bogoliubov–de Gennes calculations this LDOS anisotropy is weak, but can be as large as ~10% close to the core center (Morita *et al.*, 1997a; Berthod and Giovannini, 2001) and should be accessible experimentally in clean samples. The Eilenberger formalism leads to a more complex and

somewhat stronger fourfold anisotropy (Schophol and Maki, 1995; Ichioka *et al.*, 1996). Both semiclassical (Franz and Tešanović, 1999) and microscopic (Berthod and Giovannini, 2001) calculations showed that self-energy effects can reduce the anisotropy considerably. Although the scope and conclusions of these studies differ, a common prediction is that a weak but characteristic fourfold LDOS anisotropy around vortices should be observed in the conductance maps of *d*-wave superconductors. Up to now, such an observation has never been firmly reported by STS in high-T_c cuprates. There could be several reasons for this. The effect is expected to be very weak, the fourfold features being only a slight deviation from a completely isotropic signal. Then, in the case of mixed-symmetry models (e.g., Franz and Tešanović, 1998), additional components may damp the fourfold character of the spectroscopic signatures. Added to this comes the fact that the coherence length in HTS's is extremely short: in Y123 the spectra return to superconducting over a distance of 6–8 nm [Fig. 44(a)], while in Bi2212 this distance drops to less than 2 nm [Fig. 47(a)], suggesting that ξ for this material is 3–4 times smaller than in Y123. Kugler (2000) performed a quantitative fit of the zero-bias conductance profile across a vortex core, within the framework of a *d*-wave symmetry model (Franz and Tešanović, 1999). The fitting parameters lead to a value for ξ of the order of 1 nm. These short characteristic lengths imply stringent experimental requirements on spatial resolution and make the electronic signatures very sensitive to inhomogeneities. Accurate analysis of the conductance images have been performed for both Y123 and Bi2212. Although certain vortices mapped by STS appear with a square shape, the observations report mostly irregular patterns (Hoogenboom, Kugler, *et al.*, 2000). For Bi2212, the cores present no apparent specific symmetry. For Y123, the cores show an overall elliptical shape [Fig. 51(b)] attributed to the *ab*-plane anisotropy of the carrier effective mass (Sec. VII.A.2.a). The observation of the weak LDOS anisotropy around the vortex cores remains a considerable challenge for future STS studies. It largely depends on the availability of samples with an extremely high degree of homogeneity.

2. Irregular shapes of vortices in Bi2212

In Bi2212, images reveal that the vortices often present very irregular shapes and are in some cases even split into several subcomponents, as shown in Fig. 52(a) (Hoogenboom, Kugler, *et al.*, 2000). The full pattern (in black in the zero-bias conductance map) extends over an area of about 25 nm^2, and in this particular case three subcomponents separated by about 3 nm each can be distinguished. As seen in the spectroscopic trace shown in Fig. 52(b), in between these core elements the spectra return to the full superconducting characteristics.

The possibility of vortices occupying neighboring sites may be ruled out for two reasons. Since the expected distance between vortices at 6 T is of the order of 20 nm, a considerable energy would have to be spent to
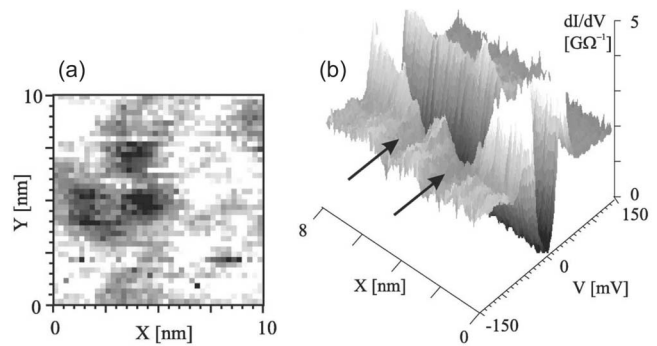

FIG. 52. Split vortex in Bi2212. (a) 10×10 nm^2 zero-bias conductance map acquired in Bi2212 ($T = 4.2$ K, $H = 6$ T). The whole core pattern is formed by split subcomponents belonging to one single flux line. (b) 8-nm trace through such a core, illustrating how the spectra recover the superconducting characteristics between two elements, whose positions are marked by arrows. From Hoogenboom, Kugler, *et al.* 2000.

place the flux lines only 3 nm apart. Moreover, images showing a large number of flux lines ensure that a pattern like the one observed in Fig. 52(a) accounts for only one vortex and that small subcomponents must belong to the same flux line. The irregular shape of the vortex cores certainly results from doping inhomogeneities. The latter are currently the subject of an intense debate concerning the role they play in the fine electronic structure of HTS's (see Sec. V). Since ξ is so small in Bi2212, the superconductor adapts to these inhomogeneities even at short length scales.

The results reported by Hoogenboom, Kugler, *et al.* (2000) were interpreted as follows. Figure 52(a) would correspond to a situation where a vortex hops back and forth between three pinning sites. This could be either thermally activated motion or quantum tunneling of vortices. Estimates of the tunneling barriers calculated from the positions of the subcomponents combined with measurements at 4.2 and 2.5 K gave evidence for the quantum tunneling scenario. Measurements at lower temperatures have to be carried out in order to reach definitive conclusions. Hoogenboom, Kugler, *et al.* also observed a slow shift of weight between the different substructures as a function of time and concluded that the vortex creep proceeds by this mode rather than by a slow motion of the vortices themselves.

It should be pointed out that the vortex-core subcomponents presented in this section are different and should be distinguished from the electronic modulations seen by Hoffman, Hudson, *et al.* (2002) and Levy *et al.* (2005) in the vortex core. In the case of the core subcomponents presented above, the sizes of the structures and distances separating them are larger. Moreover, the conductance spectra acquired between these components present the full superconducting characteristics. The electronic modulations are spatial periodic variations in the low-energy part of the conductance spectra, all observed within the pseudogap spectra characteristic of one single vortex core. That point will be discussed in Sec. VIII.C.
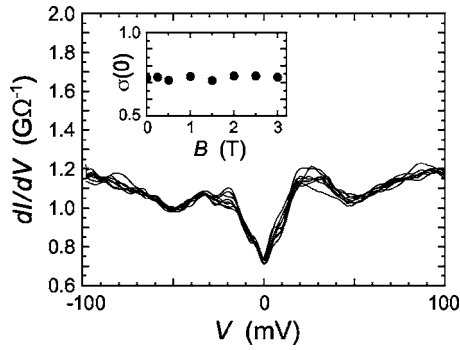
FIG. 53. Conductance spectra acquired between vortices in Y123 at $T=4.2$ K under fields ranging from 0 to 3 T. Inset: The zero-bias tunneling conductance as a function of the applied field (Maggio-Aprile *et al.*, 1995).

D. Field dependence of the spectra

Although STS is not sensitive to the phase of the order parameter, it can reveal electronic features which are a direct consequence of the order parameter symmetry. In the case of the $d_{x^2-y^2}$-wave symmetry, the presence of nodes in the gap function gives rise to low-energy nodal quasiparticles with a linear DOS at the Fermi energy [see the critical discussion by Hussey (2002)]. With a magnetic field applied parallel to the [001] direction, the superfluid screening currents flow within the *ab* planes around the vortices with a velocity $\mathbf{v}_s(\mathbf{r}) \propto 1/r$. Volovik (1993) suggested that the superfluid velocity would locally shift the quasiparticle energies by an amount $\delta E_{\mathbf{k}} = \mathbf{v}_s(\mathbf{r}) \cdot \mathbf{k}$, the so-called Doppler shift. He showed that this leads to a $1/r$ behavior of the LDOS outside the core and to an increase of the zero-energy total DOS proportional to $\sqrt{H}$. This behavior of the total DOS was also found in microscopic calculations (Wang and MacDonald, 1995). Up to now, the only known possible experimental confirmation of this prediction was provided by specific heat measurements on optimally doped Y123 by Moler *et al.* (1994), who found that the magnetic field dependence followed quite precisely the $\sqrt{H}$ law. In principle, this effect should also be directly measurable by tunneling spectroscopy through integration of the zero-bias LDOS over the unit cell of the vortex lattice. In Bi2212, the conductance spectra acquired at zero field are similar to the ones acquired at 6 T in between the vortex cores, with no noticeable evolution of the zero-bias conductance. The zero-bias conductance has also been locally measured in optimally doped Y123 by Maggio-Aprille *et al.* (1995) and appeared to be field independent up to 3 T (Fig. 53). However, since Y123 presents spectra with a large zero-bias conductance, it is not clear yet whether this observation reflects an intrinsic property or whether other competing factors mask the predicted LDOS behavior, like, for instance, lifetime effects which may wash out the $1/r$ behavior responsible for the Doppler effect. Franz and Te-šanović (1999) also argued that an anisotropic matrix element could lead to a measured tunneling conductance $\propto 1/r^3$, thus hiding the $1/r$ LDOS behavior. All

these factors may explain why the observation of the Volovik effect by STS is challenging.

E. Summary

The possibility to detect vortices with nanometer-scale resolution in HTS's is a considerable success, allowing one to uncover properties inaccessible with other techniques. Overcoming the problems due to the sample surface quality and homogeneity, individual vortices were probed in both Y123 and Bi2212. For Y123, at high fields and low temperatures, vortices are arranged in an oblique lattice, whose anisotropy is consistent with the observed intrinsic anisotropy of the cores. Direct observation of a twin boundary evidenced its ability to block the perpendicular flux-line motion.

For Bi2212, the tiny size of the cores reveals the very small coherence length of this material. The observation of a mostly disordered lattice underlines the strong pinning due to defects or inhomogeneities. The latter are also believed to be at the origin of the irregular shapes of the cores. Evidence for quantum tunneling of vortices between close pinning sites has been reported.

For both compounds, the vortex cores revealed striking electronic signatures, which cannot be understood within the framework of a conventional BCS *s*-wave or *d*-wave theory. In both underdoped and overdoped Bi2212, the cores reveal pseudogaplike spectra, similar to those measured above T_c. A pair of states at finite energy in vortex cores is systematically observed for both Y123 and Bi2212. Furthermore, the energy of these states scales linearly with the superconducting gap, strongly suggesting that the states for both materials have a common origin.

VIII. LOCAL ELECTRONIC MODULATIONS OBSERVED BY STM

The unusual properties of high-temperature superconductors and the existence of a pseudogap has led to numerous theoretical predictions for the superconducting state as well as the pseudogap state. Some of these imply the existence of spatial charge modulations, either static or dynamic, like stripes, charge-density waves, etc. The STM can in principle resolve such charge-density variations if they are static or possibly slowly fluctuating, and this has led to a search for such spatial structures in STM topographs or in STS surface maps on $Bi_2Sr_2CaCu_2O_{8+\delta}$. Two different types of spatial variations have been seen by STS: (i) large but irregular spatial variations of the gap, with typical lengths scales of the order of 3–10 nm, in samples which are not specially treated for homogeneity; and (ii) weaker but spatially periodic LDOS modulations with a wavelength of about 1.6–2 nm. The first type of spatial variations is discussed in Sec. V, whereas periodic modulations appear as a very different phenomenon and are the topic of this section.

The first indication of the presence of such periodic spatial modulations was the observation that around the center of a vortex there is a modulation of the LDOS

with a periodicity of about $4a_0$ (Hoffman, Hudson, *et al.*, 2002). Subsequently, Howald, Eisaki, Kaneko, Greven, and Kapitulnik (2003) found that charge modulations were also present in the absence of a magnetic field. They reported that the structure appeared at an energy around 25 meV and that the superperiod did not disperse with energy. Hoffman, McElroy, *et al.* (2002) reported similar zero-field electronic modulations, but in contrast to Howald, Eisaki, Kaneko, Greven, and Kapitulnik (2003) they found that these modulations disperse with energy. They successfully interpreted their findings in terms of quasiparticle interference due to scattering from impurities and other inhomogeneities. More recently Vershinin, Misra, Ono, *et al.* (2004) observed electronic modulations in the pseudogap phase above T_c. Contrary to the case of quasiparticle interference patterns, where a large number of q vectors were observed, here a single square pattern was detected with a q vector that does not disperse with energy. This finding has to be contrasted with the results obtained by McElroy, Lee, Hoffman, *et al.* (2005). They observed at low temperature, in regions of strong underdoping where the coherence peaks in the STS spectra have disappeared, that a nondispersing square pattern is found at high energy with a period similar to the one seen in the pseudogap phase. A nondispersing square lattice was subsequently found at low temperature by Hanaguri *et al.* (2004) in strongly underdoped $Ca_{1-x}Na_xCuO_2Cl_2$ (NCCOC). Finally, Levy *et al.* (2005) have recently studied the electronic modulations inside the vortex core in detail. They confirmed the initial observation by Hoffman, Hudson, *et al.* (2002), but showed that this modulation does not disperse with energy and thus appears to be similar to the one found in the pseudogap phase. They were also able to link the local square modulation to the localized state structure observed in vortex-core spectra (Maggio-Aprile *et al.*, 1995; Hoogenboom, Renner, *et al.*, 2000; Pan, Hudson, Gupta, *et al.*, 2000). They thus demonstrated the existence of a direct relation between the superconducting state and vortex-core electronic modulations.

In the following sections we shall review electronic modulations resulting from quasiparticle interference. This will be followed by a discussion of the square pattern in the pseudogap state and of electronic modulations observed in vortex cores. Finally we shall discuss the relations between these different findings.

A. Quasiparticle interference oscillations in the superconducting state

The detection of electronic modulations in the superconducting state is made difficult by the strong tendency of these materials to show inhomogeneities masking the weak periodic modulations. In order to overcome this difficulty Hoffman, McElroy, *et al.* (2002) and Howald, Eisaki, Kaneko, Greven, and Kapitulnik (2003) made large maps of the conductance at a given energy. These maps were then Fourier transformed to search for other periodicities than the atomic lattice and the well-known
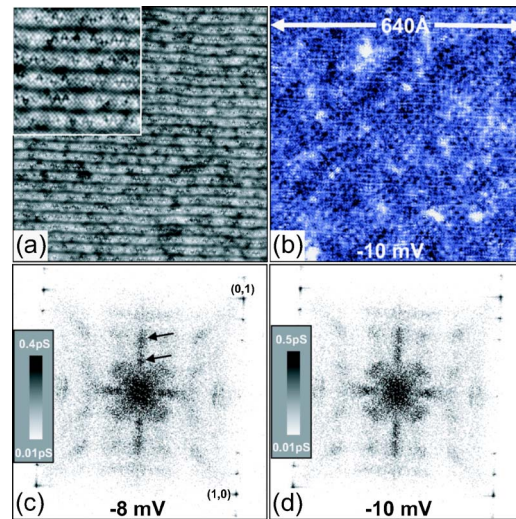

FIG. 54. (Color online) Quasiparticle interference in Bi2212. (a) Atomic-resolution image of a 64×64 nm^2 region on near-optimally doped Bi2212. Inset: 16×16 nm^2 magnification. (b) Conductance map of the same field of view acquired at $V = -10$ mV. (c) and (d) Fourier-space images of conductance maps at -8 and -10 mV, respectively. The square of intense points near the corners of each panel corresponds to the atomic lattice, and the arrows in (c) indicate the q vectors of the supermodulation. These two sets of spots do not disperse with energy. The maps clearly show an additional pattern with fourfold symmetry. The corresponding wave vectors disperse in energy. From McElroy *et al.*, 2003.

supermodulation in the b direction. In Fig. 54 we display such a map and the Fourier transform for different energies. Figure 54(a) shows the topography and 54(b) the conductance map of the same area at -10 mV. Figures 54(c) and 54(d) show the Fourier transform of such conductance maps for two different energies.

As can easily be seen, in addition to the fine points at high q values reflecting the atomic lattice and supermodulation in the b direction, one observes a number of more diffuse spots at lower q values reflecting periodic modulations of the local density of states. These spots evolve with energy in a characteristic way. Whereas the q values for the spots in the $(\pi, 0)$ and $(0, \pi)$ directions decrease with increasing energy, the q values for the spots in the $(\pm \pi, \pm \pi)$ directions increase with increasing energy. This can be understood in the framework of quasiparticle interference of a d-wave superconductor (Hoffman, McElroy, *et al.*, 2002; McElroy *et al.*, 2003; Wang and Lee, 2003; Zhang and Ting, 2003). Figure 55 illustrates the gap variation at the Fermi surface of a d-wave superconductor. At a given energy $\Delta(\mathbf{k})$ above or below the Fermi energy, interference through potential scattering can occur between points at the Fermi surface linked by the vector $\mathbf{q}_A$ or $\mathbf{q}_B$. This will give rise to oscillations in the LDOS with wave vectors $\mathbf{q}_A$ and $\mathbf{q}_B$ corresponding to the eight spots discussed above. One sees easily that the length of $\mathbf{q}_A$ will decrease with increasing energy (from the Fermi level) and the vector $\mathbf{q}_B$ will increase with increasing energy, exactly as observed in the experiment.
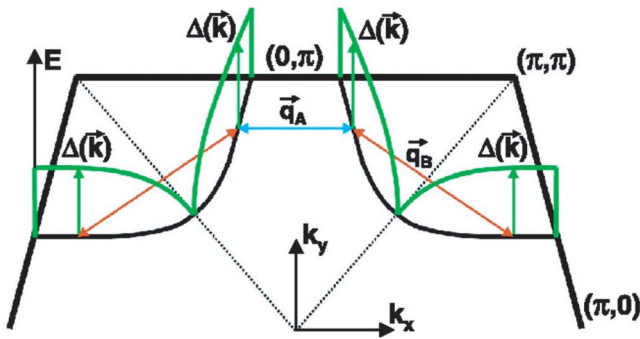
FIG. 55. (Color online) Representation of the quasiparticle energy along the Fermi surface. q_A and q_B are two possible vectors connecting quasiparticle states with identical energies, giving rise to interference patterns. From Hoffman, McElroy, *et al.*, 2002.

A more detailed analysis of these results was carried out by McElroy *et al.* (2003). By using the simple relations between the vectors q and wave vectors k one can calculate the locus (k_x, k_y) of the Fermi surface. The result reported by McElroy *et al.* (2003) is shown in Fig. 56(a) with a comparison of the ARPES results for the Fermi surface. A striking correspondence is found reinforcing the interpretation that these LDOS oscillations result from quasiparticle interference. Thus, although STM on homogeneous samples does not have k-space resolution, this can be obtained when local scattering potentials are introduced, producing quasiparticle interference. The relation $\Delta(k)$ can also be deduced from these results as illustrated in Fig. 56(b) and compares well to the results reported from ARPES measurements. Such quasiparticle interference oscillations in the LDOS at low temperature were also reported by Vershinin, Misra, Ono, *et al.* (2004) on a Bi2212 sample containing 0.6% of Zn impurities. It is important to stress that this

quasiparticle interference interpretation of the results implies that there is a sufficient number of scattering centers in the sample, i.e., that the sample contains either impurities, put in on purpose, or other imperfections resulting from sample preparation. Thus the intensity of the reflection spots in the Fourier transform is necessarily sample dependent. This may explain why Levy *et al.* (2005) did not observe such quasiparticle interference patterns in relatively homogeneous samples although they observed square modulations in the vortex cores.

The initial observations of Howald, Eisaki, Kaneko, Greven, and Kapitulnik (2003) contrast with those of Hoffman, McElroy, *et al.* (2002) and Vershinin, Misra, Ono, *et al.* (2004) in that the dominant features in the Fourier transform are four spots in the Cu-O bond direction. These do not disperse with energy and correspond to an oscillation with a period of about $4a_0$. Howald, Eisaki, Kaneko, Greven, and Kapitulnik (2003) concluded that these spots are there in addition to the spots reflecting quasiparticle interference. Using a filtered inverse Fourier transform of their images they claim to see evidence for one-dimensional stripelike patterns.

B. Electronic modulations in the pseudogap state

As discussed in Sec. VI the pseudogap state is still not understood. In a recent experiment on a slightly underdoped sample Vershinin, Misra, Ono, *et al.* (2004) succeeded to obtain detailed conductance maps at temperatures above T_c and thus to explore the pseudogap state (Fig. 57). The striking result of this investigation is the observation of a square superstructure with q values equal to $2\pi/4.7a_0$. As the energy is lowered below the pseudogap one sees a squarelike disordered pattern ap-
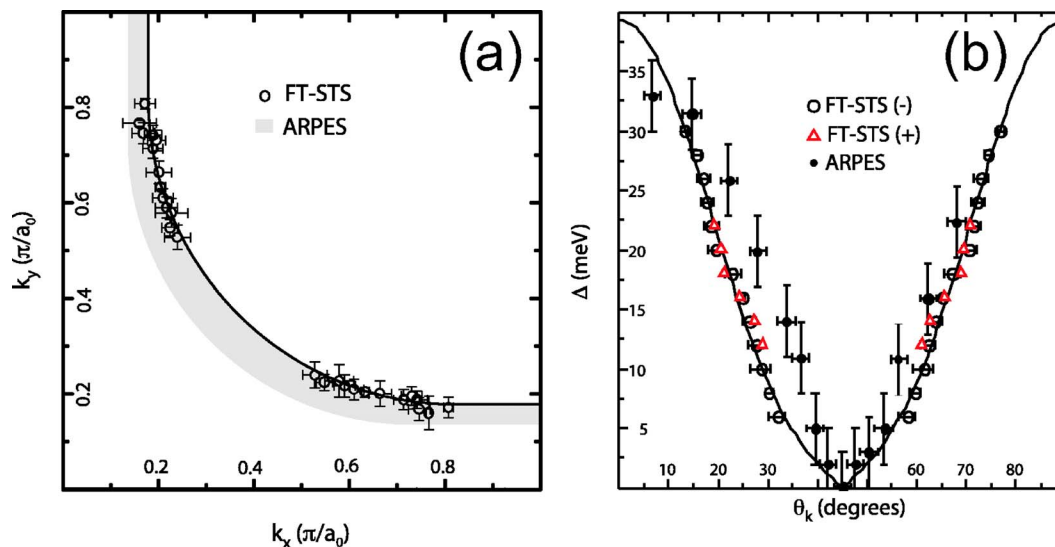

FIG. 56. (Color online) Analysis of the data shown in Fig. 54. (a) Fermi surface; the solid line is a fit to the data, assuming the Fermi surface is the combination of a circular arc joined with two straight lines. The grey band represents the Fermi surface determined by ARPES (Ding *et al.*, 1996). (b) Superconducting energy gap; the solid line is a d-wave fit to the data, and solid circles represent ARPES results (Ding *et al.*, 1996). From McElroy *et al.*, 2003.
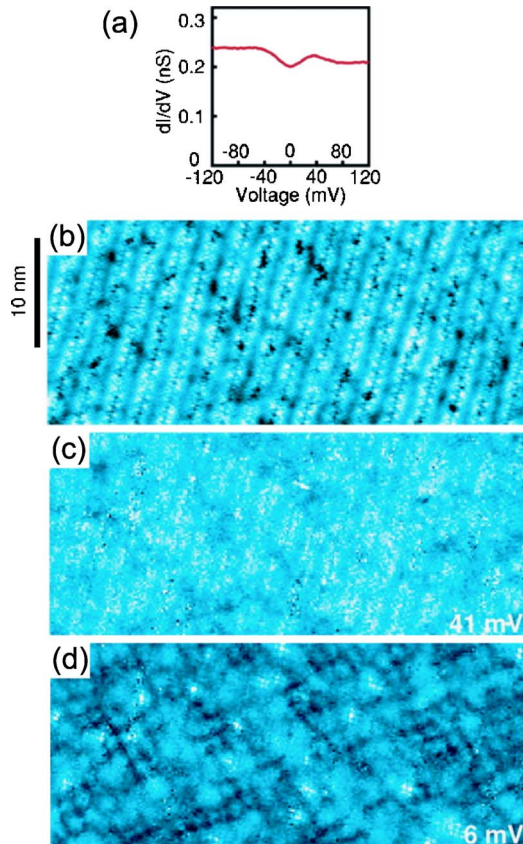
FIG. 57. (Color online) Energy and spatial dependence of the DOS at 100 K on Bi2212. (a) A typical spectrum showing the pseudogap. (b) A typical 45×19.5 nm^2 topograph showing atomic corrugation and the incommensurate supermodulation along the b axis. (c) and (d) Real-space conductance maps recorded simultaneously at 41 and 6 mV, respectively. From Vershinin, Misra, Ono, *et al.*, 2004.

pearing. The Fourier transform of one such map is shown in Fig. 58(a) and illustrated in 58(b). Four spots in the $(\pm\pi, 0)$ and $(0, \pm\pi)$ directions are seen in addition to the spots reflecting the atomic lattice. The intensity of these peaks is energy dependent and they are best seen at low energy around and below 20 meV as illustrated in Figs. 57(c) and 57(d). On the other hand, the positions of these spots in q space do not vary with energy, in contrast to the quasiparticle interference seen at lower temperature in the superconducting state at the same energies. In a more detailed analysis of these results Misra *et al.* (2004) demonstrated that the results of Vershinin, Misra, Ono, *et al.* (2004) cannot be understood in terms of a quasiparticle interference scheme.

Another situation related to the pseudogap was investigated by McElroy, Lee, Hoffman, *et al.* (2005). They studied samples with a strong inhomogeneity in the gap distribution at low temperature, presumably resulting from a local variation in the doping (see Sec. V.D). The larger the gap, i.e., the lower the doping, the smaller the coherence peaks are. Typical spectra from such a sample are shown in Fig. 16(c). Selecting strongly underdoped (on average) samples, these authors find large regions where the coherence peaks are completely suppressed. The spectra seen in such regions are illustrated in Fig. 33(a) together with spectra in higher-doping regions with smaller gaps and well-developed coherence peaks. They assigned regions without coherence peaks to a pseudogap behavior and they studied the spatial variations of the local density of states in these regions by suppressing other regions from the conductance maps. The result is that at low energy they find the same quasiparticle interference patterns as regions where a coherence peak is seen. However, in contrast to the latter regions they find at higher energy, above 65 meV, a square pattern similar to the one seen by Vershinin, Misra, Ono, *et al.* (2004) in the pseudogap state. This is illus-
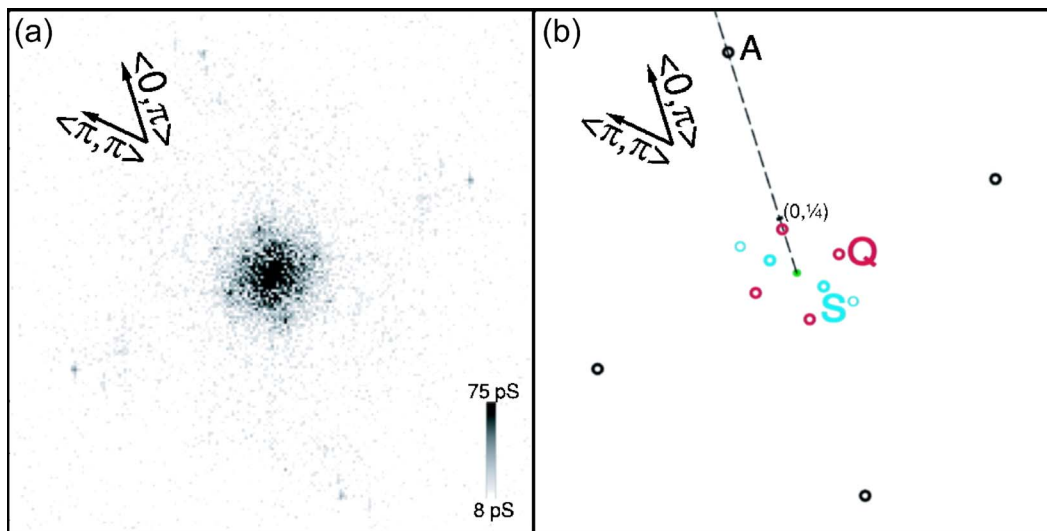

FIG. 58. (Color online) Fourier analysis of DOS modulations observed at 100 K (see also Fig. 57). (a) Fourier-space image of a conductance map $(38 \times 38$ nm$^2)$ acquired at 15 mV. (b) The Fourier-space image shows peaks corresponding to atomic sites (labeled A), primary (at $2\pi/6.8a_0$) and secondary peaks corresponding to the b-axis supermodulation (labeled S), and peaks at $\sim 2\pi/4.7a_0$ along the $(\pm\pi, 0)$ and $(0, \pm\pi)$ directions (labeled Q). From Vershinin, Misra, Ono, *et al.*, 2004.
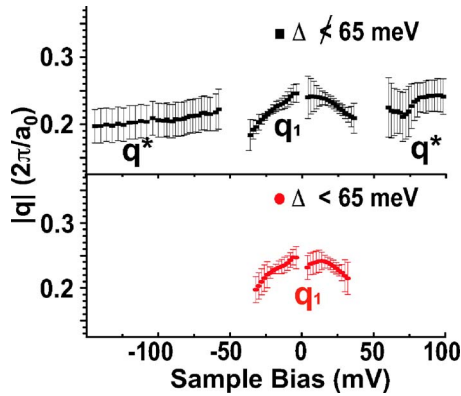
FIG. 59. (Color online) Dispersion of q vectors observed in regions with SC coherence-peaked spectra (bottom curve) and in regions with pseudogaplike spectra (top curve). The vector q^* has a length $\pi/4.5a_0 \pm 15\%$ (McElroy, Lee, Hoffman, *et al.*, 2005).

trated in Fig. 59. Their conclusion is that this square pattern, seen at high energy, is a different phenomenon than the quasiparticle oscillations seen at lower energy. Comparing the two reports discussed here (Vershinin, Misra, Ono, *et al.*, 2004; McElroy, Lee, Hoffman, *et al.*, 2005) we note the following: the nondispersing square pattern observed in the pseudogap phase above T_c in a nearly optimally doped sample is strongest at low energies. On the other hand, in the strongly underdoped samples investigated at low temperature an apparently different behavior is found. Here a nondispersing pattern is found at high energy while a dispersing quasiparticle interference pattern is found at low energy. We discuss this question further in Sec. VIII.D.

In order to study the pseudogap state in strongly underdoped samples Hanaguri *et al.* (2004) investigated $Ca_{1-x}Na_xCuO_2Cl_2$ (NCCOC). The parent compound $CaCuO_2Cl_2$ is a Mott insulator, and doping with Na makes it a superconductor for $x > 0.1$. The three compositions studied in this paper all showed a pseudogaplike tunneling spectrum. Conductivity maps at various energies showed electronic order with a dominant $4a_0 \times 4a_0$ superstructure similar to the one seen at high temperature in the pseudogap state in Bi2212. Figure 60 shows these modulations and their Fourier transform at 8 meV. The characteristic periods are energy indepen-
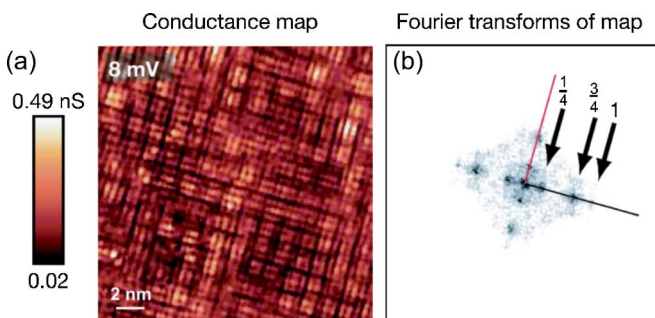

FIG. 60. (Color online) Conductance map on $Ca_{1-x}Na_xCuO_2Cl_2$ at 8 mV and the corresponding Fourier transform. From Hanaguri *et al.*, 2004.
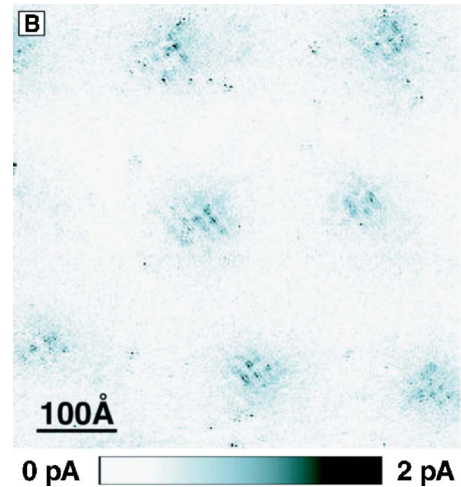

FIG. 61. (Color online) Local ordering in the vortex cores of Bi2212 seen in the difference map using the differential conductivity integrated from 0 to 12 meV. The difference map was obtained by subtracting the conductivity map obtained in zero field from the one obtained in the presence of a field of 3 T. From Hoffman, Hudson, *et al.*, 2002.

dent, as found by Vershinin, Misra, Ono, *et al.* (2004) in the pseudogap state above T_c in Bi2212. Another result implicit in the study on NCCOC is that the order appears to be independent of doping. However, since the spectra show no signature of superconductivity, no information about the precise doping level at the surface was given. Another striking result of this study was the observation of additional periodicities inside the $4a_0 \times 4a_0$ unit cell. A $\frac{4}{3}a_0$ structure was also found, suggesting a noncommensurate electronic modulation and thus a more complex structure than observed by Vershinin, Misra, Ono, *et al.* (2004). Very recently, Momono *et al.* (2005) studied two different surfaces of Bi2212 at low temperature, one (A) showing pseudogap tunneling spectra and the other (B) superconducting spectra with coherence peaks. Surface A showed a well-developed $(4a_0 \times 4a_0)$-type nondispersive modulation, whereas surface B did not show this modulation except for a small area.

C. Electronic modulations in the vortex core

Hoffman, Hudson, *et al.* (2002) analyzed conductance maps of Bi2212 taken in the presence of a magnetic field. These maps were obtained by plotting the differential conductance integrated between 0 and 12 meV. Because of the inhomogeneity of their samples, they also measured maps in zero field and obtained a difference map by subtracting the latter from the former. This is a delicate and difficult operation, but has the advantage that most perturbations due to inhomogeneities are eliminated. In this way they were able to show that the local density of states has a $4a_0 \times 4a_0$ spatial modulation in the vortex core. In Fig. 61 we display such a difference map showing a few lattice points per vortex due to this local order. Note that the variation in the conductance is
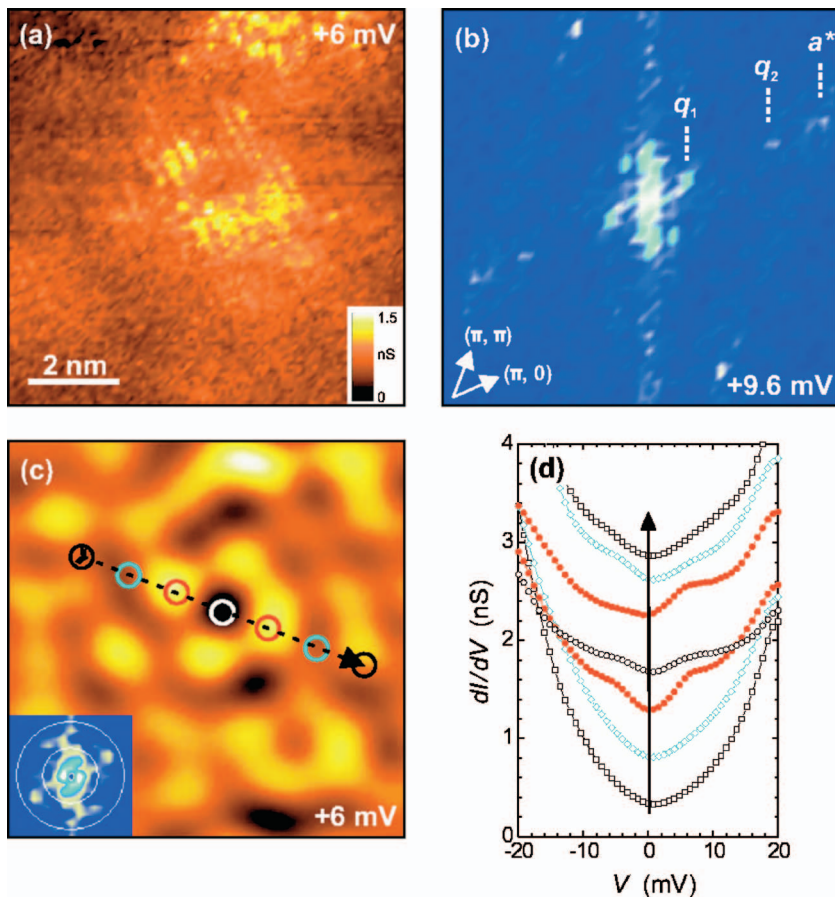
FIG. 62. (Color) Square modulation in the vortex core. (a) Conductance map at +6 mV of the area shown in Fig. 47(a), revealing a square pattern around the vortex center. (b) Fourier transform at +9.6 mV with a^* $=2\pi/a_0$, $q_1\approx\frac{1}{4}a^*$, and $q_2\approx\frac{3}{4}a^*$. (c) Filtered inverse FT image. Inset: The filter applied to the image acquired at +6 mV and which selects the region around the four q_1 peaks. (d) Spectra averaged in the seven circles along the arrow in (c). The curves are offset for clarity. Adapted from Levy *et al.*, 2005.

of the order of 10% of the zero-field signal.

More recently Levy *et al.* (2005) have carried out a detailed study of an individual vortex in Bi2212. Figure 47(a) shows a vortex imaged at −25 meV as well as spectra taken just outside the vortex and close to the vortex center. The salient features of the spectrum close to the center is that one sees a large gaplike structure, reflecting the pseudogap as discussed in Secs. VI and VII, and two peaks placed at $\sim\pm0.3\Delta_p$, suggesting the presence of one pair of localized states. Two questions motivated the investigations: (i) How does the square pattern observed in vortex cores relate to the square pattern observed in the pseudogap state above T_c? (ii) How does this square pattern in the vortex core relate to the localized state?

When this vortex was imaged at the energy of the core state [Fig. 62(a)] a square pattern oriented in the Cu-O bond direction was obtained at the center of the vortex. The Fourier transform of this pattern [Fig. 62(b)] showed, in addition to the atomic lattice, four spots with a period close to $4a_0$. A filtered inverse Fourier transform, selecting an area including the four spots, illustrates the correspondence between the latter and the pattern seen in the 6-meV image [Fig. 62(c)]. The dominant square pattern in Fig. 62(a) is well reproduced in 62(c). Note the difference in scale between Figs. 62(a) and 61. The individual spots inside each vortex of the latter correspond to the large spots in Figs. 62(a). The fine structures in Fig. 62(a) show the atomic lattice on

which is superposed the $\frac{4}{3}a_0$ period in one spatial direction.

Since it has been found that the vortex-core spectra show the pseudogap (Sec. VI.B.1), one might expect that the spatially ordered structure in the vortex cores has the same origin as the one observed in the pseudogap state. One important property of spatial modulations in the pseudogap, as discussed in Sec. VIII.B, is the absence of dispersion of **q** vectors, contrary to modulations observed in the low-temperature superconducting state. Thus one criterion in comparing the vortex cores with the pseudogap is to check whether the observed order disperses or not. This was also studied by Levy *et al.* (2005), who plotted the intensity of the Fourier transform along the $(\pi,0)$ direction for different energies. The position of the local order was indeed found to be independent of energy, exactly as observed for the pseudogap. The period in this overdoped sample was $(4.3\pm0.3)a_0$, somewhat less than observed in the underdoped sample by Vershinin, Misra, Ono, *et al.* (2004). This difference could be due either to a difference in doping or to the difference in temperature. Note that in the $(\pi,0)$ direction Levy *et al.* (2005) also observed the $\frac{4}{3}a_0$ modulation seen in NCCOC by Hanaguri *et al.* (2004).

The relation to localized states was also studied by Levy *et al.* (2005) who demonstrated that the intensity of the peaks corresponding to these states is maximal at the

four spots reflecting the local order, whereas between and outside these four spots the peaks at $\pm 0.3 \Delta_p$ are absent [Fig. 62(d)]. Since the spatial dependence of the peaks (no dispersion with position) suggests that these two peaks reflect only one pair of localized states (see Sec. VII.B), the STS measures the square of the wave function of this state. Thus the four-spot pattern in the center of the vortex may be understood as a plot of the wave function of the localized state. Note that this pattern is very different from what one would obtain for a classical *s*-wave localized state as predicted by Caroli *et al.* (1964).

D. Discussion

In this section we discuss some recent scanning tunneling spectroscopy observations on high-temperature superconductors. A detailed analysis of the tunneling spectra taken with high spatial resolution over large areas has revealed periodic variations with a spatial wavelength of the order of $(4-5)a_0$. These variations correspond to small, sometimes very small, spatial changes of the tunneling spectra. This has to be distinguished from the large gap inhomogeneities often found in these crystals as discussed in Sec. V.

The observed phenomena can be divided into two classes: (i) modulations with dispersing wavelength and (ii) modulations that do not disperse or have a much weaker dispersion than the former. The first category is observed in the superconducting state by two groups. These modulations are characterized by a large number of points in the Fourier transform and the position of these points disperse in a characteristic way with energy. In a series of papers, Hoffman, McElroy, *et al.* (2002), McElroy *et al.* (2003), Wang and Lee (2003), and Zhang and Ting (2003) convincingly interpreted these structures as modulations due to quasiparticle interference resulting from scattering on impurities and other imperfections. Note that with the observed behavior this explanation can work only if we have a *d*-wave superconductor. An *s*-wave superconductor would not give the same pattern. Also, the intensity of such charge modulations must depend on the amount of scattering centers in the sample and thus depends on the quality of the sample. This may explain why in some cases this type of density of states modulation has not been observed (Levy *et al.*, 2005). From these results one can determine the band structure around the Fermi surface as well as the angular dependence of the gap. These data, which agree largely with the results from ARPES, demonstrate how the STM, in addition to its spatial resolution, can also have *k*-space resolution.

The second category of spatial modulations has so far been observed in the pseudogap state at high temperature, on low doping, or in the vortex cores. In one case (Howald, Eisaki, Kaneko, Greven, and Kapitulnik, 2003) such modulations were reported in a Bi2212 sample which was inhomogeneous but on the average superconducting. In another case (Momono *et al.*, 2005) weak signs of modulations were observed on a superconduct-

ing surface, but modulations appeared strongly on a surface showing pseudogap behavior. In yet another case this was reported on NCCOC samples which were nominally superconducting but whose surfaces showed dominantly pseudogaplike spectra. Comparing all these data, there is considerable evidence that nondispersing order appears when *d*-wave superconductivity is suppressed, and thus that this order is a characteristic behavior of the pseudogap state. In addition to the absence of dispersion, all these square lattices have similar periodicities and the same orientation with respect to the atomic lattice. The reported periods are $4.7a_0$ in the pseudogap above T_c in an underdoped Bi2212 sample (Vershinin, Misra, Ono, *et al.*, 2004), $4.3a_0$ in the vortex cores at low temperature in a slightly overdoped Bi2212 sample (Levy *et al.*, 2005), and $4.0a_0$ at low temperature in a strongly underdoped oxychloride (Hanaguri *et al.*, 2004). A possible common interpretation of these numbers is that the square local ordering occurs at $4a_0$ at low doping and that the period increases with doping and temperature.

The observation of McElroy, Lee, Hoffman, *et al.* (2005) that the square pattern is seen at high energies in strongly underdoped samples and that in the same samples the dispersing quasiparticle interference pattern is seen at low energies seems at first to be contrary to the above conclusions. However, in this experiment the authors studied strongly underdoped regions in an inhomogeneous sample. In these regions superconducting coherence seems to be lost at high energy, i.e., for states around $(\pi, 0)$ but present at low energy, i.e., around $(\pi/2, \pi/2)$. In this sense the sample is partly in the superconducting state and partly in a pseudogap state. Thus depending on the energy one observes quasiparticle interference, characteristic of a superconducting state, or a square pattern, characteristic of a pseudogap.

Experiments on the vortex cores by Levy *et al.* (2005) bring a new dimension into this picture. The square pattern observed in the vortex core represents the spatial distribution of the localized state. On the other hand, this pattern is very similar to the order found in the pseudogap state: both are nondispersive and both have a maximum amplitude at low energy below 20 meV. Furthermore, the overall spectra of the pseudogap state and vortex core have been shown to be the same. This raises the question about the precise relation between the localized state and square pattern and in particular the question of whether the so-called localized state is also a characteristic of the pseudogap phase. So far no signature of a state at $\sim 0.3 \Delta_p$ has been observed in the pseudogap above T_c, but such a structure would most probably be thermally smeared so that one would not see it at temperatures of the order of 100 K. Thus it remains a challenge to determine whether or not there is such a state related to the zero-field pseudogap. Another scenario is that the square pattern is the characteristic feature of the pseudogap and that the localized state develops in the vortex core thanks to the presence of the square pattern.

The recent STM observations reviewed here, in the heavily underdoped NCCOC at low temperature, in the slightly underdoped Bi2212 above T_c, or in the vortex cores of slightly overdoped Bi2212, consistently reveal a tendency towards local electronic ordering when the *d*-wave superconductivity is suppressed and the pseudogap is formed. The relation between the superconducting state and pseudogap state and the appearance of spatial ordering has been the origin of numerous papers and discussions.[18]

One important experimental finding brought about by the STM investigations is strong evidence that the superconducting state, the pseudogap state, and the local square order have a common origin. Emery *et al.* (1997)

---

[18]See, e.g., Zaanen and Gunnarsson (1989), Wen and Lee (1996), Zhang (1997), Emery and Kivelson (1999), Vojta and Sachdev (1999), and Chakravarty *et al.* (2000). Several theories have predicted that the pseudogap corresponds to an ordered state. One-dimensional charge modulations, stripes, could be one candidate. Howald, Eisaki, Kaneko, Greven, and Kapitulnik (2003) argued that their observations show evidence for one-dimensional stripes. However, subsequent observations all show a clear two-dimensional pattern. One possible way out within this scenario would be that the two-dimensional pattern results from fluctuating one-dimensional domains or that the two-dimensional order results from the observation of two CuO_2 planes with crossed one-dimensional orders as put forward by Fine (2004). However, there is at present, with the exception of Howald, Eisaki, Kaneko, Greven, and Kapitulnik (2003), no experimental STM evidence in favor of any of those scenarios. Another possibility would be that local ordering is due to a spin-density wave (SDW) pinned by vortices. The SDW has been attributed to the proximity of a quantum phase transition (Demler *et al.*, 2001; Zhang *et al.*, 2002) or to strong quantum phase fluctuations (Franz *et al.*, 2002). Neutron scattering experiments have given ample evidence for the presence of such fluctuations (Cheong *et al.*, 1991; Lake *et al.*, 1999). If such fluctuations are pinned by imperfections, modulation in the LDOS may result. It has also been argued that there is local antiferromagnetic order in the vortex cores (Arovas *et al.*, 1997; Zhang, 1997; Zhu *et al.*, 2002; Takigawa *et al.*, 2004) which may be reflected in the local ordering observed in STM. Several other possibilities remain as to the nature of this electronic order. Conventional charge-density waves (Vojta, 2002) seem inconsistent with the data: this type of order, as well as the charged stripes discussed above, would induce LDOS modulations, which are approximately odd with respect to the bias polarity (Podolsky *et al.*, 2003; Chen *et al.*, 2004). In these scenarios one would also not understand why the gaps in the LDOS are always pinned at the Fermi energy (Franz, 2004). Other types of order involve the doped holes themselves. Using a variational approach to study a generalized Hubbard model, Fu *et al.* (2001) found an insulating ground state at doping $x = 1/16$, made of square-ordered solitons on top of an antiferromagnetic background. They argued that additional holes would make this system metallic and eventually superconducting at higher doping levels. The existence of this state was questioned by White and Scalapino (2004), who found that this type of structure is unstable in the *t-J* model; instead, they suggested that a pinned CDW along the one-dimensional stripes would lead to patterns similar to the ones observed experimentally.

proposed that the pseudogap reflects fluctuating superconductivity with pair correlations persisting well above T_c. A possible scenario within this scheme would be that in the pseudogap state pairs localize and form a disordered static lattice which can be seen in STM only below the pair-forming energy, i.e., the pseudogap. Several authors have proposed that the LDOS modulations reflect the spatial ordering of hole pairs rather than single holes (Chen *et al.*, 2001; Anderson, 2004; Tešanović, 2004; Melikyan and Tešanović, 2005).

The findings by STM reported in this section clearly shed light on the quest for understanding the microscopic nature of both the superconducting state and pseudogap state. Further investigations along these lines will certainly be necessary to unravel the detailed mechanisms behind the relation between the two phenomena.

IX. CONCLUSION

Over the last decade scanning tunneling spectroscopy has evolved into a major experimental tool in the quest for an understanding of high-temperature superconductors. The first main achievement of STS on HTS's was to bring tunneling experiments into focus again after the first tunneling experiments on high-temperature superconductors using various methods failed to give reproducible results. In fact, by studying the spatial dependence it was possible to demonstrate reproducible and homogeneous tunneling on high-quality Bi2212 samples (Renner and Fisher, 1994a, 1995). It thus became clear that the tunneling spectra were consistent with *d*-wave symmetry, but with an unusually high value of the gap. Later on, other groups stressed the fact that samples are often inhomogeneous (Howald *et al.*, 2001; Pan *et al.*, 2001) even if other measurements tend to indicate higher homogeneity. Thus, STS with its very high spatial resolution revealed inhomogeneities that were not fully recognized by other methods.

STS has led to a number of important discoveries. In 1995 the vortex cores could be imaged on Y123 and anomalous vortex-core spectra were observed (Maggio-Aprile *et al.*, 1995), very different from expectations of the BCS theory (*d* wave or *s* wave). In 1998 the pseudogap was observed in Bi2212 by STM in both underdoped and overdoped samples (Renner, Revaz, Genoud, *et al.*, 1998). Prior to that the pseudogap was believed to be present only in underdoped samples. STS has also uncovered the striking doping dependence of the density of states, including the doping dependence of the gap and pseudogap and their scaling relations. It was recognized that the pseudogap phase is present in vortex cores at low temperature (Renner, Revaz, Kadowaki, *et al.*, 1998). Pan, Hudson, Gupta, *et al.* (2000) and Hoogenboom, Renner, *et al.* (2000) found later that weak signals from localized states are also present in the vortex cores in Bi2212. Hoogenboom *et al.* (2001) showed that the localized states in Bi2212 and Y123 both follow a universal linear scaling with the superconducting gap and thus that the vortex-core structures in Y123 and

Bi2212 have the same origin. Two groups reported spectroscopic studies of impurities in Bi2212 and showed that a zero-bias resonance appears at the site of a non-magnetic impurity, as expected for a *d*-wave superconductor (Hudson *et al.*, 1999; Yazdani *et al.*, 1999). The introduction of Fourier-transformed conductance maps opened new possibilities (Hoffman, McElroy, *et al.*, 2002; Howald, Eisaki, Kaneko, Greven, and Kapitulnik, 2003). This led to the discovery of periodic modulations of the local density of states in the superconducting phase (McElroy *et al.*, 2002; Howald, Eisaki, Kaneko, Greven, and Kapitulnik, 2003) as well as in the pseudogap phase (Vershinin, Misra, Ono, *et al.*, 2004), and in strongly underdoped NCCOC at low temperature (Hanaguri *et al.*, 2004). Whereas modulations in the superconducting state can be understood in terms of quasiparticle interference, the simple square pattern observed in the pseudogap may turn out to be a characteristic signature of order in this phase. The observation of such patterns in the vortex cores by Hoffman, Hudson, *et al.* (2002) was recently confirmed by Levy *et al.* (2005) who demonstrated the close relations between the localized states and the square pattern. These and other results reported in this review have uncovered a large number of remarkable and unexpected behaviors of high-temperature superconductors. The STM and STS studies have thus made essential contributions to our understanding of high-temperature superconductivity.

APPENDIX A: TUNNELING THEORY IN REAL SPACE

In this appendix we reproduce the detailed calculation of the single-particle current within the tunneling Hamiltonian formalism. The derivation follows the procedure given by Mahan (1990); however, we use the real-space formulation of the problem rather than the momentum-space formulation, since our focus is on local probes like the STM.

1. Calculation of the tunneling current

The tunnel junction is described by the Hamiltonian

$$\mathcal{H} = \mathcal{H}_L + \mathcal{H}_R + \mathcal{H}_T \equiv \mathcal{H}_0 + \mathcal{H}_T. \tag{A1}$$

$\mathcal{H}_L$ and $\mathcal{H}_R$ are the Hamiltonians of the left and right materials, respectively (Fig. 4), which contain all surface and geometric effects such as surface states and defects, surface curvature (e.g., in a STM tip), etc. The central assumption of the model is that the two materials are independent, meaning that the operators on one side of the junction all commute with the operators on the other side; in particular, $\mathcal{H}_L$ commutes with $\mathcal{H}_R$. The last term in Eq. (A1) is the tunneling Hamiltonian, Eq. (2), which is responsible for the transfer of electrons across the junction. It will prove useful to write $\mathcal{H}_T = \mathcal{X} + \mathcal{X}^\dagger$ with

$$\mathcal{X} = \int d\boldsymbol{l} \, d\boldsymbol{r} T(\boldsymbol{l}, \boldsymbol{r}) \psi^\dagger(\boldsymbol{r}) \psi(\boldsymbol{l}). \tag{A2}$$

$\psi^\dagger(\boldsymbol{r})$ and $\psi(\boldsymbol{l})$ are the electron creation and destruction operators in the right and left materials, respectively, and $T(\boldsymbol{l}, \boldsymbol{r})$ gives the matrix element for an electron to tunnel from a point $\boldsymbol{l}$ in the left system to a point $\boldsymbol{r}$ in the right system. $T(\boldsymbol{l}, \boldsymbol{r})$ relates to the the matrix element $T_{\lambda\rho}$ and the single-particle states $\varphi_{\lambda,\rho}$ of Sec. III through

$$T(\boldsymbol{l}, \boldsymbol{r}) = \sum_{\lambda\rho} \varphi_\lambda^*(\boldsymbol{l}) T_{\lambda\rho} \varphi_\rho(\boldsymbol{r}). \tag{A3}$$

The tunneling current is simply given by the rate of change of the particle number on the right side (Cohen *et al.*, 1962):

$$I = e \langle \dot{\mathcal{N}}_R \rangle. \tag{A4}$$

Our convention is that $e = |e|$ and the current is taken as positive when electrons flow from left to right. Since $\mathcal{N}_R$ commutes with $\mathcal{H}_L$ and $\mathcal{H}_R$, we have $i\dot{\mathcal{N}}_R = [\mathcal{N}_R, \mathcal{H}] = [\mathcal{N}_R, \mathcal{H}_T] = \mathcal{X} - \mathcal{X}^\dagger$, in units such that $\hbar = 1$. We now calculate $\langle \dot{\mathcal{N}}_R \rangle$ to first order in $\mathcal{H}_T$. Linear-response theory gives

$$\langle \dot{\mathcal{N}}_R \rangle_t = -i \int_{-\infty}^{+\infty} dt' \, \theta(t - t') \langle [\dot{\mathcal{N}}_R(t), \mathcal{H}_T(t')] \rangle. \tag{A5}$$

On the right-hand side of Eq. (A5) the time evolution of operators is governed by $\mathcal{H}_0$ and the angular brackets represent a thermal average with respect to $\mathcal{H}_0$. Since $\mathcal{H}_L$ and $\mathcal{H}_R$ commute, this average factorizes into left and right components. We can therefore assume that the left and right systems are in independent thermody-

namic equilibria and are characterized by two different chemical potentials μ_L and μ_R. Introducing $\mathcal{K}=\mathcal{H}_0 - \mu_L\mathcal{N}_L - \mu_R\mathcal{N}_R$ we rewrite the time evolution of the operator $\mathcal{X}$ as

$$e^{i\mathcal{K}t}e^{i(\mu_L\mathcal{N}_L+\mu_R\mathcal{N}_R)t}\mathcal{X}e^{-i(\mu_L\mathcal{N}_L+\mu_R\mathcal{N}_R)t}e^{-i\mathcal{K}t}$$

$$= e^{-i(\mu_L-\mu_R)t}e^{i\mathcal{K}t}\mathcal{X}e^{-i\mathcal{K}t} \equiv e^{-ieVt}\mathcal{X}(t), \quad (A6)$$

where V is the applied bias. The last line of Eq. (A6) is obtained using $e^{\mathcal{N}}\psi^\dagger=\psi^\dagger e^{\mathcal{N}+1}$ and $e^{\mathcal{N}}\psi=\psi e^{\mathcal{N}-1}$. We then have

$$i\dot{\mathcal{N}}_R(t) = e^{-ieVt}\mathcal{X}(t) - e^{ieVt}\mathcal{X}^\dagger(t), \quad (A7a)$$

$$\mathcal{H}_T(t') = e^{-ieVt'}\mathcal{X}(t') + e^{ieVt'}\mathcal{X}^\dagger(t'), \quad (A7b)$$

where the time evolution of $\mathcal{X}$ and $\mathcal{X}^\dagger$ is now governed by $\mathcal{K}$ as in Eq. (A6). Inserting Eq. (A7) into Eq. (A5) and using Eq. (A4) one arrives at

$$I = 2e\,\text{Im}\int_{-\infty}^{+\infty}dt'\{e^{-ieV(t-t')}(-i)\theta(t-t')\langle[\mathcal{X}(t),\mathcal{X}^\dagger(t')]\rangle$$

$$+ e^{-ieV(t+t')}(-i)\theta(t-t')\langle[\mathcal{X}(t),\mathcal{X}(t')]\rangle\} \equiv I_s + I_J(t). \quad (A8)$$

The first term I_s is the single-particle current and the second term is the pair (Josephson) current. According to Eq. (A8), I_s is the Fourier transform, at energy $-eV$, of the retarded correlation function $X(t-t')=-i\theta(t-t') \times\langle[\mathcal{X}(t),\mathcal{X}^\dagger(t')]\rangle$ of the (bosonic) operator $\mathcal{X}$. The latter is most easily evaluated by analytically continuing onto the real-frequency axis the corresponding temperature propagator (Mahan, 1990, p. 149):

$$\mathscr{X}(i\Omega_n) = -\int_0^\beta d\tau e^{i\Omega_n\tau}\langle\mathcal{T}_\tau\mathcal{X}(\tau)\mathcal{X}^\dagger(0)\rangle. \quad (A9)$$

$\Omega_n=2n\pi/\beta$ denote the even Matsubara frequencies with β the inverse temperature. One thus has

$$I_s = 2e\,\text{Im}\,\mathscr{X}(i\Omega_n \to -eV + i0^+). \quad (A10)$$

Looking at Eqs. (A9) and (A2) we see that $\mathscr{X}(i\Omega_n)$ is made up of the terms

$$-\langle\mathcal{T}_\tau\psi^\dagger(\boldsymbol{r}_1,\tau)\psi(\boldsymbol{l}_1,\tau)\psi^\dagger(\boldsymbol{l}_2,0)\psi(\boldsymbol{r}_2,0)\rangle$$

$$= \langle\mathcal{T}_\tau\psi(\boldsymbol{l}_1,\tau)\psi^\dagger(\boldsymbol{l}_2,0)\rangle\langle\mathcal{T}_\tau\psi(\boldsymbol{r}_2,0)\psi^\dagger(\boldsymbol{r}_1,\tau)\rangle$$

$$= \mathscr{G}(\boldsymbol{l}_1,\boldsymbol{l}_2,\tau)\mathscr{G}(\boldsymbol{r}_2,\boldsymbol{r}_1,-\tau). \quad (A11)$$

We have introduced the temperature Green's functions on both sides of the junction, with the usual definitions

$$\mathscr{G}(\boldsymbol{x}_1,\boldsymbol{x}_2,\tau) = -\langle\mathcal{T}_\tau\psi(\boldsymbol{x}_1,\tau)\psi^\dagger(\boldsymbol{x}_2,0)\rangle \quad (A12a)$$

$$= \frac{1}{\beta}\sum_n e^{-i\omega_n\tau}\mathscr{G}(\boldsymbol{x}_1,\boldsymbol{x}_2,i\omega_n), \quad (A12b)$$

with $\omega_n=(2n+1)\pi/\beta$ the odd Matsubara frequencies. It is then straightforward to evaluate $\mathscr{X}(i\Omega_n)$ in Eq. (A9) using Eqs. (A11) and (A12b):

$$\mathscr{X}(i\Omega_n) = \int d\boldsymbol{l}_1 d\boldsymbol{r}_1 d\boldsymbol{l}_2 d\boldsymbol{r}_2 T(\boldsymbol{l}_1,\boldsymbol{r}_1)T^*(\boldsymbol{l}_2,\boldsymbol{r}_2)$$

$$\times \frac{1}{\beta}\sum_m \mathscr{G}(\boldsymbol{l}_1,\boldsymbol{l}_2,i\omega_m)\mathscr{G}(\boldsymbol{r}_2,\boldsymbol{r}_1,i\omega_m-i\Omega_n).$$

The frequency sum is easily performed within the spectral representation,

$$\mathscr{G}(\boldsymbol{x}_1,\boldsymbol{x}_2,i\omega_m) = \int_{-\infty}^{+\infty}d\omega\frac{A(\boldsymbol{x}_1,\boldsymbol{x}_2,\omega)}{i\omega_m-\omega}, \quad (A13)$$

and using the usual trick for frequency summation (Mattuck, 1992, p. 251). We have, letting $i\Omega_n\to-eV+i0^+$,

$$\mathscr{X}(-eV+i0^+)$$

$$= \int d\boldsymbol{l}_1 d\boldsymbol{r}_1 d\boldsymbol{l}_2 d\boldsymbol{r}_2 T(\boldsymbol{l}_1,\boldsymbol{r}_1)T^*(\boldsymbol{l}_2,\boldsymbol{r}_2)\int d\omega d\omega'$$

$$\times \frac{A(\boldsymbol{l}_1,\boldsymbol{l}_2,\omega)A(\boldsymbol{r}_2,\boldsymbol{r}_1,\omega')[f(\omega)-f(\omega')]}{\omega-\omega'+eV-i0^+}.$$

Taking the imaginary part, inserting into Eq. (A10), and reintroducing a dimensional factor $\hbar^{-1}$, we finally get

$$I_s = \frac{2\pi e}{\hbar}\int d\omega[f(\omega-eV)-f(\omega)]$$

$$\times \int d\boldsymbol{l}_1 d\boldsymbol{r}_1 d\boldsymbol{l}_2 d\boldsymbol{r}_2 T(\boldsymbol{l}_1,\boldsymbol{r}_1)T^*(\boldsymbol{l}_2,\boldsymbol{r}_2)$$

$$\times A(\boldsymbol{l}_1,\boldsymbol{l}_2,\omega-eV)A(\boldsymbol{r}_2,\boldsymbol{r}_1,\omega). \quad (A14)$$

Equation (3) results immediately from Eq. (A14) by a change of representation, i.e., substituting the matrix element with Eq. (A3) and choosing the single-particle states that diagonalize the spectral function

$$\int d\boldsymbol{x}_1 d\boldsymbol{x}_2\varphi_i^*(\boldsymbol{x}_1)A(\boldsymbol{x}_1,\boldsymbol{x}_2,\omega)\varphi_j(\boldsymbol{x}_2) = \delta_{ij}A_i(\omega).$$

TABLE III. Gap values for $Bi_2Sr_2CuO_{6+\delta}$ (Bi2201).

T_c (K)	p	Δ_p (meV)	$\frac{2\Delta_p}{k_BT_c}$	Reference
<4[a]	0.160	16±3		Kugler *et al.* (2001, Sec. VI.A.2)
10[b]	0.180	12±3	27.9	Kugler *et al.* (2001)
3.5[b]	0.185	13±3	86.2	Kugler (2000)
With La or Pb substitutions				
29[c]	0.145	14.5±3	11.6	Kugler (2000)
10[d]		25±5	58.0	Mashima *et al.* (2003)

[a]$Bi_{2.2}Sr_{1.8}CuO_{6+\delta}$.
[b]$Bi_{2.1}Sr_{1.9}CuO_{6+\delta}$.
[c]$Bi_{1.8}Sr_{1.7}La_{0.5}CuO_{6+\delta}$.
[d]$Bi_{2.1}Pb_{0.37}Sr_{1.91}CuO_{6+\delta}$.

TABLE IV. Gap values for $Bi_2Sr_2CaCu_2O_{8+\delta}$ (Bi2212). Values indicated without parentheses are given explicitly in the publications. Values within parentheses were estimated using the generic formula $p=0.16\pm\sqrt{(1-T_c/T_c^{max})/82.6}$ (Presland *et al.*, 1991) with $T_c^{max}=92$ K. Where the sample is claimed to be optimally doped although $T_c \neq T_c^{max}$, we set p to [0.16].

T_c (K)	p	Δ_p (meV)	$\frac{2\Delta_p}{k_B T_c}$	Reference
63	(0.10)	40	14.7	Nakano *et al.* (1998)
60	0.10	36 ± 2	13.9	Oda *et al.* (1997)
65	0.11	62	22.1	McElroy *et al.* (2004), McElroy, Lee, Hoffmann, *et al.* (2005)
67	0.11	55 ± 15	19.1	Matsuda *et al.* (2003)
78	(0.12)	50.2	14.9	Hoffman, Hudson, *et al.* (2002)
80	(0.12)	42 ± 2	12.2	Howald *et al.* (2001)
81	(0.12)	50	14.3	Matsuda *et al.* (1999a, 1999b)
81	(0.12)	40	11.5	Murakami and Aoki (1995)
75	0.13	48 ± 1	14.9	McElroy *et al.* (2004), McElroy, Lee, Hoffmann, *et al.* (2005)
86	(0.13)	52	14.0	Matsuda *et al.* (1999a, 1999b)
83	(0.13)	47 ± 4	13.1	Mastuba, Sakata, Mochiku, *et al.* (2003)
(85)	0.13	45 ± 12	12.3	Matsuda *et al.* (2003)
85	(0.13)	33	9.0	Nakano *et al.* (1998)
83	(0.13)	44	12.3	Renner, Revaz, Genoud, *et al.* (1998)
86	(0.13)	45	12.1	Sakata *et al.* (2003)
79	0.14	50	14.7	Lang *et al.* (2002)
88	(0.14)	50	13.2	Matsuura *et al.* (1998)
82	0.14	34 ± 2	9.6	Oda *et al.* (1997)
79	0.15	43 ± 1	12.6	McElroy *et al.* (2004), McElroy, Lee, Hoffmann, *et al.* (2005)
80	0.15	38	11.0	Oda *et al.* (2000)
92	(0.16)	35	8.8	DeWilde *et al.* (1998)
92	(0.16)	43.7	11.0	Hoffman, Hudson, *et al.* (2002)
92	[0.16]	30 ± 2	7.6	Iavarone *et al.* (1998)
84[a]	[0.16]	40	11.0	Misra *et al.* (2002a)
93[a,b]	(0.16)	25–55	~10.0	Cren *et al.* (2000)
90	[0.16]	54	13.9	Matsuda *et al.* (1999a, 1999b)
89	0.16	40 ± 10	10.4	Matsuda *et al.* (2003)
88	[0.16]	32 ± 2	8.4	Oda *et al.* (1997)
92.3	[0.16]	29 ± 4	7.3	Renner and Fischer (1995)
92.2	[0.16]	41.5	10.4	Renner, Revaz, Genoud, *et al.* (1998)
90	[0.16]	39	10.1	Wolf *et al.* (1994)
86.5[c]	(0.18)	45 ± 15	12.1	Howald, Eisaki, Kaneko, Greven, and Kapitulnik (2003), Howald, Eisaki, Kaneko, and Kapitulnik (2003)
88	(0.18)	28 ± 2	7.4	Kitazawa *et al.* (1997)
(89)	0.18	35.6	9.3	Lang *et al.* (2002)
(89)	0.18	36 ± 1	9.4	McElroy *et al.* (2004), McElroy, Lee, Hoffmann, *et al.* (2005)
(89)	0.18	35 ± 7	9.1	Matsuda *et al.* (2003)
85	(0.19)	25	6.8	Chen and Ng (1992)
85	(0.19)	36.7	10.0	Hoffman, Hudson, *et al.* (2002)
87	(0.19)	32	8.5	Hudson *et al.* (1999)
87	(0.19)	26	7.4	Ichimura and Nomura (1993)
86	(0.19)	35 ± 5	9.4	Kaneko *et al.* (1999)
89	0.19	33 ± 1	8.6	McElroy *et al.* (2004), McElroy, Lee, Hoffmann, *et al.* (2005)
85	(0.19)	35	9.6	Maki *et al.* (2001)
84	(0.19)	50	13.8	Matsuda *et al.* (1999a, 1999b)

TABLE IV. (*Continued.*)

T_c (K)	p	Δ_p (meV)	$\frac{2\Delta_p}{k_B T_c}$	Reference
85	(0.19)	26	7.1	Nakano *et al.* (1998)
84	(0.19)	32	8.8	Pan, Hudson, Gupta, *et al.* (2000)
87	(0.19)	17[d]	4.5	Suzuki *et al.* (1999b)
87	(0.19)	31–40[e]	~9.3	Suzuki *et al.* (1999a)
		40		Hudson *et al.* (2000)
76.4	(0.20)	47±13	12.2	Hoogenboom, Kadowaki, *et al.* (2003)
77	(0.20)	30±1	9.0	Kugler *et al.* (2000)
77	(0.20)	40±10	12.1	Hoogenboom, Kugler, *et al.* (2000)
77	(0.20)	45±5	13.6	Hoogenboom, Renner, *et al.* (2000)
80.7	(0.20)	36±2	10.4	Hoogenboom, Kadowaki, *et al.* (2003)
81	(0.20)	43	12.3	Matsuda *et al.* (1999a, 1999b)
82	(0.20)	34±1	9.6	Oda *et al.* (1996)
72	(0.21)	30	9.7	DeWilde *et al.* (1998)
72	(0.21)	22±2	7.1	Iavarone *et al.* (1998)
		29±5		Mallet *et al.* (1996)
81	0.21	27±2	7.7	Oda *et al.* (1997)
80	0.21	24	7.0	Oda *et al.* (2000)
74.3	(0.21)	34	10.6	Renner, Revaz, Genoud, *et al.* (1998)
74	(0.21)	32±2	10.0	Yazdani *et al.* (1999)
(64)	0.22	22±5	8.0	Matsuda *et al.* (2003)
56	(0.23)	21	8.7	Renner, Revaz, Genoud, *et al.* (1998)
With Zn, Ni, Co, or Pb substitutions:				
84[f]	(0.13)	45	12.4	Pan, Hudson, Lang, *et al.* (2000)
85[g]	(0.19)	20	5.5	Hudson *et al.* (2003)
[h]		50[i]		Zhao *et al.* (2000)
[j]		50		Cren *et al.* (2001)
68[k]	(0.22)	40±20	13.7	Kinoda *et al.* (2003)

[a]Thin film.
[b]$Bi_2Sr_{1.98}Ca_{1.38}Cu_{2.28}O_{8+\delta}$, $T_c^{onset}=93$ K by dc resistivity and 55 K by ac susceptibility.
[c]$Bi_{2.1}Sr_{1.9}CaCu_2O_{8+\delta}$.
[d]Tunneling direction in the *ab* plane varies between [110] and [100].
[e]$I\|[110]$.
[f]$Bi_2Sr_2Ca(Cu_{1-x}Zn_x)_2O_{8+\delta}$.
[g]$Bi_2Sr_2Ca(Cu_{1-x}Ni_x)_2O_{8+\delta}$.
[h]$Bi_{1.83}Sr_{1.8}Ca(Cu_{1-x}Co_x)_2O_{8+\delta}$.
[i]Measured at $T=66$ K.
[j]$Bi_{1.95}Pb_{0.5}Sr_2CaCu_2O_{8+\delta}$.
[k]$Bi_{1.4}Pb_{0.6}Sr_2CaCu_2O_{8+\delta}$.

General relations about the real-space Green's function and spectral function are given by Hedin and Lundqvist (1969). Of particular interest is the relation between the spectral function and local density of states: $N(\boldsymbol{x},\omega) = A(\boldsymbol{x},\boldsymbol{x},\omega)$.

The calculation of the Josephson current proceeds along the same lines, by considering the anomalous correlation function of the operator $\mathcal{X}$:

$$I_J(t) = 2e \operatorname{Im} e^{-2ieVt} \mathcal{Y}(i\Omega_n \to eV + i0^+),$$

$$\mathcal{Y}(i\Omega_n) = -\int_0^\beta d\tau e^{i\Omega_n\tau} \langle \mathcal{T}_\tau \mathcal{X}(\tau)\mathcal{X}(0)\rangle.$$

We refer the reader to the work of Josephson (1969) for a detailed discussion of this term.

2. STM and the local density of states

Starting from Eq. (A14) it is easy to see how the Tersoff-Hamann (1983) matrix element Eq. (8) leads to

Eq. (5) for the tunneling current. Inserting $T_{\lambda\rho} \propto \varphi_\rho^*(\boldsymbol{x})$ into Eq. (A3) one gets, owing to the completion property of the functions φ_ρ,

$$T(\boldsymbol{l},\boldsymbol{r}) \propto \delta(\boldsymbol{r}-\boldsymbol{x})\sum_\lambda \varphi_\lambda^*(\boldsymbol{l}). \qquad (A15)$$

The delta function in the matrix element (A15) substitutes $A(\boldsymbol{r}_2,\boldsymbol{r}_1,\omega)$ in Eq. (A14) with $A(\boldsymbol{x},\boldsymbol{x},\omega)=N_R(\boldsymbol{x},\omega)$. On the other hand, if the tip material is a simple metal, its spectral function takes the form Hedin and Lundqvist (1969)

$$A(\boldsymbol{l}_1,\boldsymbol{l}_2,\omega)=\sum_\lambda \varphi_\lambda(\boldsymbol{l}_1)\varphi_\lambda^*(\boldsymbol{l}_2)\delta(\omega-\varepsilon_\lambda). \qquad (A16)$$

Then the $\boldsymbol{l}$ integrals in Eq. (A14) cancel the λ sums of Eq. (A15) due to the orthogonality of the functions φ_λ. Thus Eqs. (A14)–(A16) lead to

$$I_s \propto \int d\omega[f(\omega-eV)-f(\omega)]N_L(\omega-eV)N_R(\boldsymbol{x},\omega).$$

In the calculation of the matrix element Eq. (8), Tersoff and Hamann assumed that the sample electronic structure can be represented by independent electrons, so that φ_ρ was meant as the true wave function in the sample. Nevertheless, we implicitly considered in our derivation that the validity of Eq. (8) carries over to the case where the functions φ_ρ are general basis functions. In this way the validity of Eq. (5) could be extended to correlated systems. We believe that this procedure is correct, since the Tersoff-Hamann calculation does not depend on the detailed form and nature of φ_ρ.

3. Case of a nonlocal matrix element

If the relation between the matrix element and sample wave function is nonlocal, like in Eq. (9), then using Eq. (A3) the form of Eq. (A15) is generalized to

$$T(\boldsymbol{l},\boldsymbol{r}) \propto M(\boldsymbol{r}-\boldsymbol{x})\sum_\lambda \varphi_\lambda^*(\boldsymbol{l}). \qquad (A17)$$

The resulting tunneling conductance is, using Eq. (A14) and the common approximations for the tip,

$$\sigma(\boldsymbol{x},V) \propto \int d\omega[-f'(\omega-eV)]\int d\boldsymbol{r}_1 d\boldsymbol{r}_2$$

$$\times M(\boldsymbol{r}_1-\boldsymbol{x})M^*(\boldsymbol{r}_2-\boldsymbol{x})A(\boldsymbol{r}_2,\boldsymbol{r}_1,\omega). \qquad (A18)$$

If the sample is translation invariant $A(\boldsymbol{r}_2,\boldsymbol{r}_1,\omega)=A(\boldsymbol{r}_2-\boldsymbol{r}_1,\omega)$, this expression takes a simpler form in reciprocal space. Then the conductance no longer depends on $\boldsymbol{x}$ and is just Eq. (10).

APPENDIX B: HTS GAPS MEASURED BY STS

Here we provide a list of superconducting gap values of high-T_c cuprates which have been obtained by scanning tunneling spectroscopy (see Tables III–X). The superconducting gap is defined by the energy $\pm\Delta_p$ of the superconducting coherence peaks. All collected data

TABLE V. Gap values for $Bi_2Sr_2Ca_2Cu_3O_{10+\delta}$ (Bi2223).

T_c (K)	p	Δ_p (meV)	$\dfrac{2\Delta_p}{k_BT_c}$	Reference
109	UD	60±3	12.8	Kugler *et al.* (2006)
111	OP	45±7	9.4	Kugler *et al.* (2006)

TABLE VI. Gap values for $HgBa_2Ca_{n-1}Cu_nO_{2n+2+\delta}$.

T_c (K)	p	Δ_p (meV)	$\dfrac{2\Delta_p}{k_BT_c}$	Reference
Hg1201 ($n=1$)				
97[a]	OP	33	7.9	Wei, Tsuei, *et al.* (1998)
Hg1212 ($n=2$)				
123[b]	OP	50	9.4	Wei, Tsuei, *et al.* (1998)
Hg1223 ($n=3$)				
125[c]	(OP)	~24[d]	4.5	Rossel *et al.* (1994)
133[a]	(OP)	~38[e]	6.6	Rossel *et al.* (1994)
135[a]	OP	75	12.7	Wei, Tsuei, *et al.* (1998)

[a]Polycrystal.
[b]Thin film.
[c]Melted sample.
[d]$\Delta=15$ meV using Dynes fit.
[e]$\Delta=24\pm2$ meV using Dynes fit.

TABLE VII. Gap values for $La_{2-x}Sr_xCuO_4$ (La214). The doping level was determined directly by the Sr stoichiometry ($p=x$).

T_c (K)	p	Δ_p (meV)	$\dfrac{2\Delta_p}{k_BT_c}$	Reference
29.5	0.10	7.5	5.9	Tanaka *et al.* (1995, 1996)
~40	0.14	16	9.3	Nakano *et al.* (1998)
~35	0.14	17	11.3	Oda *et al.* (2000)
33	0.15	7	4.9	Kirtley *et al.* (1987)
35.5	0.15	5.5	3.6	Tanaka *et al.* (1995, 1996)
39	0.16	8±2	4.8	Kato *et al.* (2003)
~40	0.18	10	5.8	Nakano *et al.* (1998)
~35	0.18	9	5	Oda *et al.* (2000)

TABLE VIII. Gap values for $YBa_2Cu_3O_{7-\delta}$ (Y123).

T_c (K)	p	Δ_p (meV)	$\dfrac{2\Delta_p}{k_B T_c}$	Reference
60	UD	~20	7.7	Yeh *et al.* (2001)
85[a]	UD	19	5.2	Yeh *et al.* (2001)
89	UD	20	5.2	Born *et al.* (2002)
82[b]	OP	18	5.1	Yeh *et al.* (2001)
85[c]	(OP)	18	4.9	Kirtley *et al.* (1987)
85[c]	(OP)	15[d]	4.1	Kirtley *et al.* (1987)
90[a]	?	14±2[e]	3.6	Hoevers *et al.* (1988)
90	OP	28[f]	7.2	Tanaka *et al.* (1994)
90[a]	OP	~20	5.2	Ueno *et al.* (2001, 2003)
90	OP	28	7.2	Wan *et al.* (1989)
>90[a]	(OP)	~17.5[e]	4.5	Miller *et al.* (1993)
91	(OP)	24–32	7.1	Murakami *et al.* (2001)
91	(OP)	~25[g]	6.4	Murakami *et al.* (2001)
92[a]	OP	20[h]	5.0	Alff *et al.* (1997)
92[a]	OP	20	5.0	Born *et al.* (2002)
92	OP	30±8	7.6	Edwards *et al.* (1992)
92	OP	20	5.0	Edwards *et al.* (1995)
92[a]	OP	17.5[e]	4.4	Koinuma *et al.* (1993)
92[a]	OP	~21[h]	5.3	Koyanagi *et al.* (1995)
92	OP	28±2	7.1	Kugler *et al.* (2000)
92	OP	20±2	5.0	Maggio-Aprile *et al.* (1995)
92	OP	18	4.5	Maggio-Aprile *et al.* (2000)
92	(OP)	18	4.5	Maki *et al.* (2001)
92[a]	OP	20[e]	5.0	Nantoh, Hasegawa, Kawasaki, *et al.* (1994)
92[a]	OP	30±10[h]	7.6	Nantoh *et al.* (1995)
92	OP	19±4	4.8	Wei *et al.* (1998b)
92	OP	29±3[e]	7.3	Wei *et al.* (1998b)
92	OP	27±4[h]	6.8	Wei *et al.* (1998b)
92.9	OP	18	4.5	Yeh *et al.* (2001)
90	OD	20	5.2	Shibata *et al.* (2003a, 2003b)
78[a,i]	OD	19	5.7	Yeh *et al.* (2001)

[a]Thin film.
[b]$YBa_2Cu_{0.9934}Zn_{0.0026}Mg_{0.0043}O_{6.9}$.
[c]Measured by high-field magnetic susceptibility, $T_c = 92$ K by resistivity.
[d]$I\|ab$ plane.
[e]Tunneling on (100) plane.
[f]Tunneling on (110) and (100) planes.
[g]Tunneling on electrical field etched surface.
[h]Tunneling on (110) plane.
[i]$Y_{0.7}Ca_{0.3}Ba_2Cu_3O_{7-\delta}$.

were obtained on SIN vacuum tunnel junctions at low temperature and on single crystals with the tip perpendicular to the (001) surface plane ($I\|[100]$), unless stated differently. The data are listed as a function of increasing doping level for underdoped (UD), optimally doped (OP), and overdoped (OD) materials.

TABLE IX. Gap values for $NdBa_2Cu_3O_{7-\delta}$ (Nd123).

T_c (K)	p	Δ_p (meV)	$\dfrac{2\Delta_p}{k_B T_c}$	Reference
95[a]	OP	30	7.3	Nishiyama *et al.* (2002)

[a]Measured by a superconducting quantum interference device.

TABLE X. Gap values for $Nd_{2-x}Ce_xCuO_{4-\delta}$, an electron-doped cuprate.

T_c (K)	p	Δ_p (meV)	$\dfrac{2\Delta_p}{k_B T_c}$	Reference
18	(OP)	4.5[a]	5.8	Kashiwaya *et al.* (1997)
17.5	OP	4 ± 1.5	5.3	Kashiwaya *et al.* (1998)
18	(OP)	>5	6.4	Kashiwaya *et al.* (1997)
20.5	OP	~ 4.5[b]	5.1	Hayashi, Ueda, *et al.* (1998)

[a]Tunneling on (100) plane.
[b]$I \| [110]$ and $[100]$.

REFERENCES

Abrikosov, A. A., 1957, Sov. Phys. JETP **5**, 1174.

Abrikosov, A. A., and L. P. Gor'kov, 1960, Sov. Phys. JETP **12**, 1243.

Affleck, I., M. Franz, and M. H. Sharifzadef Amin, 1997, Phys. Rev. B **55**, R704.

Affleck, I., and J. B. Marston, 1988, Phys. Rev. B **37**, 3774.

Aleszkiewicz, M., P. Aleszkiewicz, and J. Rauluszkiewicz, 1997, Czech. J. Phys. **47**, 367.

Alff, L., Y. Krockenberger, B. Welter, M. Schonecke, R. Gross, D. Manske, and M. Naito, 2003, Nature (London) **422**, 698.

Alff, L., A. Marx, R. Gross, A. Beck, H. Takashima, S. Kashiwaya, M. Koyanagi, and Y. Tanaka, 1998, Appl. Supercond. **6**, 783.

Alff, L., H. Takashima, S. Kashiwaya, N. Terada, H. Ihara, Y. Tanaka, M. Koyanagi, and K. Kajimura, 1997, Phys. Rev. B **55**, R14757.

Alloul, H., T. Ohno, and P. Mendels, 1989, Phys. Rev. Lett. **63**, 1700.

Anagawa, K., Y. Yamada, T. Watanabe, and M. Suzuki, 2003, Phys. Rev. B **67**, 214513.

Andersen, B. M., H. Bruus, and P. Hedegård, 2000, Phys. Rev. B **61**, 6298.

Anderson, P. W., 1959, J. Phys. Chem. Solids **11**, 26.

Anderson, P. W., 1987, Science **235**, 1196.

Anderson, P. W., 1997, *The Theory of Superconductivity in the High-T_c Cuprates* (Princeton University Press, Princeton).

Anderson, P. W., 2004, e-print cond-mat/0406038.

Anderson, P. W., P. A. Lee, M. Randeria, T. M. Rice, N. Trivedi, and F. C. Zhang, 2004, J. Phys.: Condens. Matter **16**, R755.

Anderson, P. W., and N. P. Ong, 2006, J. Phys. Chem. Solids **67**, 1.

Ando, Y., Y. Hanaki, S. Ono, K. Segawa, Y. Abe, and N. Miyamoto, 2000, Phys. Rev. B **61**, R14956.

Appelbaum, J. A., and W. F. Brinkman, 1969a, Phys. Rev. **183**, 553.

Appelbaum, J. A., and W. F. Brinkman, 1969b, Phys. Rev. **186**, 464.

Aprili, M., E. Badica, and L. H. Greene, 1999, Phys. Rev. Lett. **83**, 4630.

Aprili, M., M. Covington, E. Paraoanu, B. Niedermeier, and L. H. Greene, 1998, Phys. Rev. B **57**, R8139.

Arovas, D. P., A. J. Berlinsky, C. Kallin, and S.-C. Zhang, 1997, Phys. Rev. Lett. **79**, 2871.

Balatsky, A. V., M. I. Salkola, and A. Rosengren, 1995, Phys. Rev. B **51**, 15547.

Balatsky, A. V., I. Vekhter, and J.-X. Zhu, 2006, Rev. Mod. Phys. **78**, 373.

Bardeen, J., 1961, Phys. Rev. Lett. **6**, 57.

Bardeen, J., 1962, Phys. Rev. Lett. **9**, 147.

Bardeen, J., L. N. Cooper, and J. R. Schrieffer, 1957, Phys. Rev. **108**, 1175.

Bednorz, J. G., and K. A. Müller, 1986, Z. Phys. B: Condens. Matter **64**, 189.

Behler, S., S. H. Pan, P. Jess, A. Baratoff, H.-J. Guenterodt, F. Levy, G. Wirth, and J. Wiesner, 1994, Phys. Rev. Lett. **72**, 1750.

Berthod, C., and B. Giovannini, 2001, Phys. Rev. Lett. **87**, 277002.

Besocke, K., 1987, Surf. Sci. **181**, 145.

Beuermann, G., 1981, Z. Phys. B: Condens. Matter **44**, 29.

Binnig, G., and H. Rohrer, 1982a, Helv. Phys. Acta **55**, 726.

Binnig, G., and H. Rohrer, 1982b, Helv. Phys. Acta **55**, 128.

Binnig, G., and H. Rohrer, 1987, Rev. Mod. Phys. **59**, 615.

Biswas, A., P. Fournier, V. N. Smolyaninova, R. C. Budhani, J. S. Higgins, and R. L. Greene, 2001, Phys. Rev. B **64**, 104519.

Blonder, G. E., M. Tinkham, and T. M. Klapwijk, 1982, Phys. Rev. B **25**, 4515.

Born, V., C. Jooss, and H. C. Freyhardt, 2002, Physica C **382**, 224.

Brown, S. P., D. Charalambous, E. C. Jones, E. M. Forgan, P. G. Kealey, A. Erb, and J. Kohlbrecher, 2004, Phys. Rev. Lett. **92**, 067004.

Büttiker, M., Y. Imry, R. Landauer, and S. Pinhas, 1985, Phys. Rev. B **31**, 6207.

Byers, J. M., M. E. Flatté, and D. J. Scalapino, 1993, Phys. Rev. Lett. **71**, 3363.

Campuzano, J. C., G. Jennings, M. Faiz, L. Beaulaigue, B. W. Veal, J. Z. Liu, A. P. Paulikas, K. Vandervoort, H. Claus, R. S. List, A. J. Arko, and R. J. Bartlett, 1990, Phys. Rev. Lett. **64**, 2308.

Campuzano, J. C., M. Norman, and M. Randeria, 2004, in *Physics of Superconductors*, edited by K. H. Bennemann and J. B. Ketterson (Springer, Berlin), Vol. II, p. 167.

Carlson, E. W., V. J. Emery, S. A. Kivelson, and D. Orgad, 2004, in *The Physics of Superconductors*, edited by K. H. Bennemann and J. B. Ketterson (Springer-Verlag, Berlin), Vol. II.

Carminati, R., and J. J. Sáenz, 2000, Phys. Rev. Lett. **84**, 5156.

Caroli, C., R. Combescot, P. Nozières, and D. Saint-James, 1971, J. Phys. C **4**, 916.

Caroli, C., P. G. de Gennes, and J. Matricon, 1964, Phys. Lett. **9**, 307.

Chakravarty, S., R. B. Laughlin, D. K. Morr, and C. Nayak, 2001, Phys. Rev. B **63**, 094503.

Chakravarty, S., A. Sudbø, P. W. Anderson, and S. Strong, 1993, Science **261**, 337.

Chen, C. J., 1988, J. Vac. Sci. Technol. A **6**, 319.

Chen, C. J., 1990a, Phys. Rev. Lett. **65**, 448.

Chen, C. J., 1990b, Phys. Rev. B **42**, 8841.

Chen, C. J., 1993, *Introduction to Scanning Tunneling Microscopy* (Oxford University Press, New York).

Chen, H.-D., J.-P. Hu, S. Capponi, E. Arrigoni, and S.-C. Zhang, 2002, Phys. Rev. Lett. **89**, 137004.

Chen, H.-D., O. Vafek, A. Yazdani, and S.-C. Zhang, 2004, Phys. Rev. Lett. **93**, 187002.

Chen, Q., and K.-W. Ng, 1992, Phys. Rev. B **45**, 2569.

Chen, Q., J. Stajic, S. Tan, and K. Levin, 2005, Phys. Rep. **412**, 1.

Chen, X. J., and H. Q. Lin, 2004, Phys. Rev. B **69**, 104518.

Chen, Y., and C. S. Ting, 2002, Phys. Rev. B **65**, 180513(R).

Cheong, S. W., G. Aeppli, T. E. Mason, H. Mook, S. M. Hayden, P. C. Canfield, Z. Fisk, K. N. Clausen, and J. L. Martinez, 1991, Phys. Rev. Lett. **67**, 1791.

Chubukov, A. V., D. Pines, and J. Schmalian, 2003, in *Conventional and High-T$_c$ Superconductors*, edited by K. Bennemann and J. Ketterson, The Physics of Superconductors Vol. I (Spinger, Berlin) p. 495.

Chubukov, A. V., D. Pines, and B. P. Stojković, 1996, J. Phys.: Condens. Matter **8**, 10017.

Ciraci, S., and I. P. Batra, 1987, Phys. Rev. B **36**, 6194.

Clogston, A. M., 1962, Phys. Rev. Lett. **9**, 266.

Cohen, M. H., L. M. Falicov, and J. C. Phillips, 1962, Phys. Rev. Lett. **8**, 316.

Coleman, R. V., Z. Dai, W. W. McNairy, C. G. Slough, and C. Wang, 1992, in *Surface Properties of Layered Structures*, edited by G. Benedek (Kluwer Academic, Dordrecht), p. 27.

Crabtree, G. W., G. K. Leaf, H. G. Kaper, V. M. Vinokur, A. E. Koshelev, D. W. Braun, D. M. Levine, W. K. Kwok, and J. A. Fendrich, 1996, Physica C **263**, 401.

Cren, T., D. Roditchev, W. Sacks, and J. Klein, 2001, Europhys. Lett. **54**, 84.

Cren, T., D. Roditchev, W. Sacks, K. Klein, J.-B. Moussy, C. Deville-Cavellin, and M. Laguës, 2000, Phys. Rev. Lett. **84**, 147.

Cuevas, J. C., A. Martín-Rodero, and A. Levy Yeyati, 1996, Phys. Rev. B **54**, 7366.

Dagotto, E., 1994, Rev. Mod. Phys. **66**, 763.

Damascelli, A., Z. Hussain, and Z.-X. Shen, 2003, Rev. Mod. Phys. **75**, 473.

Demler, E., W. Hanke, and S.-C. Zhang, 2004, Rev. Mod. Phys. **76**, 909.

Demler, E., S. Sachdev, and Y. Zhang, 2001, Phys. Rev. Lett. **87**, 067202.

Derro, D. J., E. W. Hudson, K. M. Lang, S. H. Pan, J. C. Davis, J. T. Markert, and A. L. de Lozanne, 2002, Phys. Rev. Lett. **88**, 097002.

Dessau, D. S., B. O. Wells, Z.-X. Shen, W. E. Spicer, A. J. Arko, R. S. List, D. B. Mitzi, and A. Kapitulnik, 1991, Phys. Rev. Lett. **66**, 2160.

de Trey, P., S. Gygax, and J. P. Jan, 1973, J. Low Temp. Phys. **11**, 421.

Deutscher, G., 1999, Nature (London) **397**, 410.

Deutscher, G., 2005, Rev. Mod. Phys. **77**, 109.

DeWilde, Y., M. Iavarone, U. Welp, V. Metlushko, A. E. Koshelev, I. Aranson, G. W. Crabtree, and P. C. Canfield, 1997, Phys. Rev. Lett. **78**, 4273.

DeWilde, Y., M. Iavarone, U. Welp, V. Metlushko, A. E. Koshelev, I. Aranson, G. W. Crabtree, P. L. Gammel, D. J. Bishop, and P. C. Canfield, 1997, Physica C **282-287**, 355.

DeWilde, Y., N. Miyakawa, P. Guptasarma, M. Iavarone, L. Ozyuzer, J. F. Zasadzinski, P. Romano, D. G. Hinks, C. Kendziora, G. W. Crabtree, and K. E. Gray, 1998, Phys. Rev. Lett. **80**, 153.

Ding, H., T. Yokoya, J. C. Campuzano, T. Takahashi, M. Randeria, M. R. Norman, T. Mochiku, K. Kadowaki, and J. Giapintzakis, 1996, Nature (London) **382**, 51.

Dipasupil, R. M., M. Oda, and M. Ido, 2002, J. Phys. Soc. Jpn. **71**, 1535.

Dolan, G. J., G. V. Chandrashekhar, T. R. Dinger, C. Feild, and F. Holtzberg, 1989, Phys. Rev. Lett. **62**, 827.

Dolan, G. J., F. Holtzberg, C. Feild, and T. R. Dinger, 1989, Phys. Rev. Lett. **62**, 2184.

Doyen, G., D. Drakova, and M. Scheffler, 1993, Phys. Rev. B **47**, 9778.

Duke, C. B., 1969, in *Solid State Physics: Advances in Research and Applications*, edited by F. Seitz, D. Turnbull, and H. Ehrenreich (Academic, New York), Vol. 10.

Eckl, T., D. J. Scalapino, E. Arrigoni, and W. Hanke, 2002, Phys. Rev. B **66**, 140510.

Edwards, H. L., D. J. Derro, A. L. Barr, J. T. Markert, and A. L. de Lozanne, 1995, Phys. Rev. Lett. **75**, 1387.

Edwards, H. L., J. T. Markert, and A. L. de Lozanne, 1992, Phys. Rev. Lett. **69**, 2967.

Edwards, H. L., J. T. Markert, and A. L. de Lozanne, 1994, J. Vac. Sci. Technol. B **12**, 1886.

Ekvall, I., E. Wahlström, D. Claesson, H. Olin, and E. Olsson, 1999, Meas. Sci. Technol. **10**, 11.

Eliashberg, G. M., 1960, Sov. Phys. JETP **11**, 696.

Emery, V. J., and S. A. Kivelson, 1995, Nature (London) **374**, 434.

Emery, V. J., and S. A. Kivelson, 1999, J. Low Temp. Phys. **117**, 189.

Emery, V. J., S. A. Kivelson, and H. Q. Lin, 1990, Phys. Rev. Lett. **64**, 475.

Emery, V. J., S. A. Kivelson, and O. Zachar, 1997, Physica C **282**, 174.

Eschrig, M., and M. R. Norman, 2000, Phys. Rev. Lett. **85**, 3261.

Eskildsen, M. R., P. L. Gammel, B. P. Barber, A. P. Ramirez, D. J. Bishop, N. H. Andersen, K. Mortensen, C. A. Bolle, C. M. Lieber, and P. C. Canfield, 1997, Phys. Rev. Lett. **79**, 487.

Eskildsen, M. R., M. Kugler, S. Tanaka, J. Jun, S. M. Kazakov, J. Karpinski, and Ø. Fischer, 2002, Phys. Rev. Lett. **89**, 187003.

Essmann, U., and H. Träuble, 1967, Phys. Lett. **24**, 526.

Fang, A., C. Howald, N. Kaneko, M. Greven, and A. Kapitulnik, 2004, Phys. Rev. B **70**, 214514.

Feng, D. L., D. H. Lu, K. M. Shen, C. Kim, H. Eisaki, A. Damascelli, R. Yoshizaki, J.-I. Shimoyama, K. Kishio, G. D. Gu, S. Oh, A. Andrus, J. O'Donnell, J. N. Eckstein, and Z.-X. Shen, 2000, Science **289**, 277.

Feuchtwang, T. E., 1974, Phys. Rev. B **10**, 4121.

Fine, B. V., 2004, Phys. Rev. B **70**, 224508.

Foley, E. T., A. F. Kam, and J. W. Lyding, 2000, Rev. Sci. Instrum. **71**, 3428.

Fong, H. F., P. Bourges, Y. Sidis, L. P. Regnault, A. Ivanov, G. D. Gu, N. Koshizuka, and B. Keimer, 1999, Nature (London) **398**, 588.

Fong, H. F., B. Keimer, P. W. Anderson, D. Reznik, F. Dogan, and I. A. Aksay, 1995, Phys. Rev. Lett. **75**, 316.

Franz, M., 2004, Science **305**, 1410.

Franz, M., and A. J. Millis, 1998, Phys. Rev. B **58**, 14572.

Franz, M., D. E. Sheehy, and Z. Tešanović, 2002, Phys. Rev. Lett. **88**, 257005.

Franz, M., and Z. Tešanović, 1998, Phys. Rev. Lett. **80**, 4763.

Franz, M., and Z. Tešanović, 1999, Phys. Rev. B **60**, 3581.

Franz, M., and Z. Tešanović, 2001, Phys. Rev. Lett. **87**, 257003.

Fu, H. C., J. C. Davis, and D.-H. Lee, 2004, e-print cond-mat/0403001.

Fukuyama, H., H. Tan, T. Kumakura, and M. Morishita, 1996, Czech. J. Phys. **46**, 2847.

Gammel, P., C. A. Duran, D. J. Bishop, V. G. Kogan, M. Ledvij, A. Y. Simonov, J. P. Rice, and D. M. Ginsberg, 1992, Phys. Rev. Lett. **69**, 3808.

Gammel, P. L., D. J. Bishop, G. J. Dolan, J. R. Kwo, C. A. Murray, L. F. Schneemeyer, and J. V. Waszczak, 1987, Phys. Rev. Lett. **59**, 2592.

Geshkenbein, V. B., L. B. Ioffe, and A. I. Larkin, 1997, Phys. Rev. B **55**, 3173.

Giaever, I., 1960, Phys. Rev. Lett. **5**, 147.

Giovannini, B., and C. Berthod, 2001, Phys. Rev. B **63**, 144516.

Gladyshevskii, R., N. Musolino, and R. Flükiger, 2004, Phys. Rev. B **70**, 184522.

Gladyshevskii, R. E., and R. Flükiger, 1996, Acta Crystallogr., Sect. B: Struct. Sci. **52**, 38.

Gorina, J. I., G. A. Kaljushnaia, V. P. Martovitsky, V. V. Rodin, and N. N. Sentjurina, 1998, Solid State Commun. **108**, 175.

Güntherodt, H.-J., and R. Wiesendanger, 1994, Eds., *Scanning Tunneling Microscopy* (Springer-Verlag), Vol. I.

Gupta, A. K., and K.-W. Ng, 1998, Phys. Rev. B **58**, R8901.

Gygi, F., and M. Schlüter, 1990a, Phys. Rev. Lett. **65**, 1820.

Gygi, F., and M. Schlüter, 1990b, Phys. Rev. B **41**, 822.

Gygi, F., and M. Schlüter, 1991, Phys. Rev. B **43**, 7609.

Hamers, R. J., R. M. Tromp, and J. E. Demuth, 1986, Phys. Rev. Lett. **56**, 1972.

Han, J. H., and D.-H. Lee, 2000, Phys. Rev. Lett. **85**, 1100.

Hanaguri, T., C. Lupien, Y. Kohsaka, D.-H. Lee, M. Azuma, M. Takano, H. Takagi, and J. C. Davis, 2004, Nature (London) **430**, 1001.

Hancotte, H., D. N. Davydov, M. Ye, and R. Deltour, 1995, Physica B **204**, 206.

Harrison, W. A., 1961, Phys. Rev. **123**, 85.

Hasegawa, T., and K. Kitazawa, 1990, Jpn. J. Appl. Phys., Part 2 **29**, L434.

Hasegawa, T., M. Nantoh, and K. Kitazawa, 1991, Jpn. J. Appl. Phys., Part 2 **30**, L276.

Hasegawa, T., M. Nantoh, N. Motohira, K. Kishio, and K. Kitazawa, 1991, Supercond. Sci. Technol. **4**, S73.

Hasegawa, T., M. Nantoh, A. Takagi, H. Ikuta, M. Kawasaki, H. Koinuma, and K. Kitazawa, 1992, J. Phys. Chem. Solids **53**, 1643.

Hayashi, N., M. Ichioka, and K. Machida, 1996, Phys. Rev. Lett. **77**, 4074.

Hayashi, N., T. Isoshima, M. Ichioka, and K. Machida, 1998, Phys. Rev. Lett. **80**, 2921.

Hayashi, F., E. Ueda, M. Sato, K. Kurahashi, and K. Yamada, 1998, J. Phys. Soc. Jpn. **67**, 3234.

He, H., Y. Sidis, P. Bourges, G. D. Gu, A. Ivanov, N. Koshizuka, B. Liang, C. T. Lin, L. P. Regnault, E. Schoenherr, and B. Keimer, 2001, Phys. Rev. Lett. **86**, 1610.

Hedin, L., and S. Lundqvist, 1969, in *Solid State Physics: Advances in Research and Applications*, edited by F. Seitz, D. Turnbull, and H. Ehrenreich (Academic, New York), Vol. 23.

Heim, S., T. Nachtrab, M. Mossle, R. Kleiner, R. Koch, S. Rother, P. Waldmann, O. Müller, T. Kimura, and Y. Tokura, 2002, Physica C **367**, 348.

Heinrich, A. J., C. P. Lutz, J. A. Gupta, and D. M. Eigler, 2003, in *Scanning Tunneling Microscopy/Spectroscopy and Related Techniques*, edited by Paul M. Koenraad and Martijn Kemerink, AIP Conf. Proc. No. 696 (AIP, Melville, NY).

Heinrich, H., G. Kostorz, B. Heeb, and L. J. Gauckler, 1994, Physica C **224**, 133.

Herbsommer, J. A., G. Nieva, and J. Luzuriaga, 2000, Phys. Rev. B **62**, 3534.

Herman, F., R. V. Kasowski, and W. Y. Hsu, 1988, Phys. Rev. B **38**, 204.

Hess, H. F., R. B. Robinson, R. C. Dynes, J. M. Valles, and J. V. Waszczak, 1989, Phys. Rev. Lett. **62**, 214.

Hess, H. F., R. B. Robinson, and J. V. Waszczak, 1990, Phys. Rev. Lett. **64**, 2711.

Hess, H. F., R. B. Robinson, and J. V. Waszczak, 1991, Physica B **169**, 422.

Himeda, A., M. Ogata, Y. Tanaka, and S. Kashiwaya, 1997, J. Phys. Soc. Jpn. **66**, 3367.

Hoevers, H. F. C., P. J. M. van Bentum, L. E. C. van de Leemput, H. van Kempen, A. J. G. Schellingerhout, and D. van der Marel, 1988, Physica C **152**, 105.

Hofer, W. A., A. J. Fisher, R. A. Wolkow, and P. Grütter, 2001, Phys. Rev. Lett. **87**, 236104.

Hofer, W. A., A. S. Foster, and A. L. Shluger, 2003, Rev. Mod. Phys. **75**, 1287.

Hoffman, J. E., E. W. Hudson, K. M. Lang, V. Madhavan, H. Eisaki, S. Uchida, and J. C. Davis, 2002, Science **295**, 466.

Hoffman, J. E., K. McElroy, D.-H. Lee, K. M. Lang, H. Eisaki, S. Uchida, and J. C. Davis, 2002, Science **297**, 1148.

Hoogenboom, B. W., C. Berthod, M. Peter, Ø. Fischer, and A. A. Kordyuk, 2003, Phys. Rev. B **67**, 224502.

Hoogenboom, B. W., K. Kadowaki, B. Revaz, Ø. Fischer, and A. A. Kordyuk, 2003, Physica C **391**, 376.

Hoogenboom, B. W., K. Kadowaki, B. Revaz, M. Li, C. Renner, and Ø. Fischer, 2001, Phys. Rev. Lett. **87**, 267001.

Hoogenboom, B. W., M. Kugler, B. Revaz, I. Maggio-Aprile, Ø. Fischer, and C. Renner, 2000, Phys. Rev. B **62**, 9179.

Hoogenboom, B. W., C. Renner, B. Revaz, I. Maggio-Aprile, and Ø. Fischer, 2000, Physica C **332**, 440.

Horch, S., P. Zeppenfeld, R. David, and G. Comsa, 1994, Rev. Sci. Instrum. **65**, 3204.

Howald, C., H. Eisaki, N. Kaneko, M. Greven, and A. Kapitulnik, 2003, Phys. Rev. B **67**, 014533.

Howald, D., H. Eisaki, N. Kaneko, and A. Kapitulnik, 2003, Proc. Natl. Acad. Sci. U.S.A. **100**, 9705.

Howald, C., P. Fournier, and A. Kapitulnik, 2001, Phys. Rev. B **64**, 100504(R).

Hu, C.-R., 1994, Phys. Rev. Lett. **72**, 1526.

Hubler, U., P. Jess, H. P. Lang, A. Erb, E. Walker, M. Regier, D. Schild, J. Halbritter, and H.-J. Güntherodt, 1998, Appl. Phys. A: Mater. Sci. Process. **66**, S1219.

Hudson, E. W., K. M. Lang, V. Madhavan, S. H. Pan, H. Eisaki, S. Uchida, and J. C. Davis, 2001, Nature (London) **411**, 920.

Hudson, E. W., V. Madhavan, K. McElroy, J. E. Hoffman, K. M. Lang, H. Eisaki, S. Uchida, and J. C. Davis, 2003, Physica B **329**, 1365.

Hudson, E. W., S. H. Pan, A. K. Gupta, K. W. Ng, and J. C. Davis, 1999, Science **285**, 88.

Hudson, E. W., S. H. Pan, K. M. Lang, A. K. Gupta, K.-W. Ng, and J. C. Davis, 2000, Physica B **284**, 969.

Huscroft, C., and R. T. Scalettar, 1998, Phys. Rev. Lett. **81**, 2775.

Hussey, N. E., 2002, Adv. Phys. **51**, 1685.

Hwu, Y., L. Lozzi, M. Marsi, S. La Rosa, M. Winokur, P. Davis, M. Onellion, H. Berger, F. Gozzo, F. Lévy, and G. Margaritondo, 1991, Phys. Rev. Lett. **67**, 2573.

Hybertsen, M. S., and L. F. Mattheiss, 1988, Phys. Rev. Lett. **60**, 1661.

Iavarone, M., Y. De Wilde, P. Guptasarma, D. G. Hinks, G. W. Crabtree, and P. C. Canfield, 1998, J. Phys. Chem. Solids **59**, 2030.

Ichimura, K., and K. Nomura, 1993, J. Phys. Soc. Jpn. **62**, 3661.

Ichioka, M., A. Hasegawa, and K. Machida, 1999, Phys. Rev. B

59, 8902.

Ichioka, M., N. Hayashi, N. Enomoto, and K. Machida, 1996, Phys. Rev. B **53**, 15316.

Ikeda, K., K. Takamuku, H. Kubota, R. Itti, and N. Koshizuka, 1993, Rev. Sci. Instrum. **64**, 2221.

Inoue, A., H. Mukaida, M. Nakao, and R. Yoshizaki, 1994, Physica C **233**, 49.

Inoue, A., M. Nakao, and R. Yoshizaki, 1995, Physica C **249**, 151.

Jarlborg, T., and G. Santi, 2000, Physica C **329**, 243.

Josephson, B. D., 1962, Phys. Lett. **1**, 251.

Josephson, B. D., 1969, in *Superconductivity*, edited by R. D. Parks (Dekker, New York), Vol. 1, p. 423.

Junod, A., A. Erb, and C. Renner, 1999, Physica C **317-318**, 333.

Kamerlingh Onnes, H., 1911, Comm. Leiden **120b**.

Kampf, A. P., and J. P. Schrieffer, 1990, Phys. Rev. B **42**, 7967.

Kane, J., and K. W. Ng, 1996, Phys. Rev. B **53**, 2819.

Kaneko, S., H. Sakata, Y. Ono, N. Nishida, T. Mochiku, and K. Hirata, 1999, Surf. Sci. **438**, 353.

Karraï, K., E. J. Choi, F. Dunmore, S. H. Liu, H. D. Drew, Q. Li, D. B. Fenner, Y. D. Zhu, and F.-C. Zhang, 1992, Phys. Rev. Lett. **69**, 152.

Kashiwaya, S., L. Alff, H. Takashima, N. Terada, T. Ito, K. Oka, Y. Tanaka, M. Koyanagi, S. Ueno, and K. Kajimura, 1997, Physica C **282-287**, 1477.

Kashiwaya, S., T. Ito, K. Oka, S. Ueno, H. Takashima, M. Koyanagi, Y. Tanaka, and K. Kajimura, 1998, Phys. Rev. B **57**, 8680.

Kashiwaya, S., and Y. Tanaka, 2000, Rep. Prog. Phys. **63**, 1641.

Kato, T., H. Morimoto, A. Katagiri, S. Okitsu, and H. Sakata, 2003, Physica C **392**, 221.

Keimer, B., W. Y. Shih, R. W. Erwin, J. W. Lynn, F. Dogan, and I. A. Aksay, 1994, Phys. Rev. Lett. **73**, 3459.

Kent, A. D., C. Renner, P. Niedermann, J.-G. Bosch, and Ø. Fischer, 1992, Ultramicroscopy **42-44**, 1632.

Kinoda, G., T. Hasegawa, S. Nakao, T. Hanaguri, K. Kitazawa, K. Shimizu, J. Shimoyama, and K. Kishio, 2003, Phys. Rev. B **67**, 224509.

Kirk, M. D., J. Nogami, A. A. Baski, D. B. Mitzi, A. Kapitulnik, T. H. Geballe, and C. F. Quate, 1988, Science **242**, 1673.

Kirtley, J. R., R. T. Collins, Z. Schlesinger, W. J. Gallagher, R. L. Sandstrom, T. R. Dinger, and D. A. Chance, 1987, Phys. Rev. B **35**, 8846.

Kishine, J.-i., P. A. Lee, and X.-G. Wen, 2001, Phys. Rev. Lett. **86**, 5365.

Kitazawa, K., T. Hasegawa, T. Taneda, S. Matsuura, T. Endo, H. Sugawara, J. Shimoyama, and K. Kishio, 1997, Physica C **282**, 1479.

Kitazawa, K., H. Sugawara, and T. Hasegawa, 1996, Physica C **263**, 214.

Kivelson, S. A., I. P. Bindloss, E. Fradkin, V. Oganesyan, J. M. Tranquada, A. Kapitulnik, and C. Howald, 2003, Rev. Mod. Phys. **75**, 1201.

Kleefisch, S., B. Welter, A. Marx, L. Alff, R. Gross, and M. Naito, 2001, Phys. Rev. B **63**, 100507.

Kleiner, R., F. Steinmeyer, G. Kunkel, and P. Müller, 1992, Phys. Rev. Lett. **68**, 2394.

Kohen, A., Y. Dagan, and G. Deutscher, 2000, Physica C **341**, 687.

Koinuma, H., S. Gonda, J. Gong, M. Kawasaki, M. Yoshimoto, M. Nantoh, T. Hasegawa, and K. Kitazawa, 1993, J. Phys. Chem. Solids **54**, 1215.

Kondo, Y., E. T. Foley, T. Amakusa, N. Shibata, S. Chiba, M. Iwatsuki, and H. Tokumoto, 2001, Rev. Sci. Instrum. **72**, 2977.

Kouznetsov, K., and L. Coffey, 1996, Phys. Rev. B **54**, 3617.

Koyanagi, M., S. Kashiwaya, M. Matsuda, H. Takashima, and K. Kajimura, 1995, Jpn. J. Appl. Phys., Part 1 **34**, 89.

Krakauer, H., and W. E. Pickett, 1988, Phys. Rev. Lett. **60**, 1665.

Krasnov, V. M., A. E. Kovalev, A. Yurgens, and D. Winkler, 2001, Phys. Rev. Lett. **86**, 2657.

Krasnov, V. M., A. Yurgens, D. Winkler, P. Delsing, and T. Claeson, 2000, Phys. Rev. Lett. **84**, 5860.

Krusin-Elbaum, L., T. Shibauchi, G. Blatter, C. H. Mielke, M. Li, M. P. Maley, and P. H. Kes, 2003, Physica C **387**, 169.

Kugler, M., 2000, Ph.D. thesis, University of Geneva.

Kugler, M., 2001, unpublished.

Kugler, M., G. Levy de Castro, E. Giannini, A. Piriou, A. A. Manuel, C. Hess, and Ø. Fischer, 2006, J. Phys. Chem. Solids **67**, 353.

Kugler, M., C. Renner, V. Mikheev, G. Batey, and Ø. Fischer, 2000, Rev. Sci. Instrum. **71**, 1475.

Kugler, M., C. Renner, S. Ono, Y. Ando, and Ø. Fischer, 2001, Phys. Rev. Lett. **86**, 4911.

Lake, B., G. Aeppli, T. E. Mason, A. Schroder, D. F. McMorrow, K. Lefmann, M. Isshiki, M. Nohara, H. Takagi, and S. M. Hayden, 1999, Nature (London) **400**, 43.

Lammert, P. E., and D. S. Rokhsar, 2001, e-print cond-mat/0108146.

Lang, H., T. Frey, and H.-J. Güntherodt, 1991, Europhys. Lett. **15**, 667.

Lang, K. M., V. Madhavan, J. E. Hoffman, E. W. Hudson, H. Eisaki, S. Uchida, and J. C. Davis, 2002, Nature (London) **415**, 412.

Lang, N. D., 1985, Phys. Rev. Lett. **55**, 230.

Laughlin, R. B., 1998, Phys. Rev. Lett. **80**, 5188.

Ledvij, M., and R. A. Klemm, 1995, Phys. Rev. B **51**, 3269.

Lee, P. A., 1993, Phys. Rev. Lett. **71**, 1887.

Lee, P. A., N. Nagaosa, and X.-G. Wen, 2006, Rev. Mod. Phys. **78**, 17.

Lee, P. A., and X.-G. Wen, 2001, Phys. Rev. B **63**, 224517.

Levinstein, H. J., and J. E. Kunzler, 1966, Phys. Lett. **20**, 581.

Levy, G., 2005, unpublished.

Levy, G., M. Kugler, A. A. Manuel, Ø. Fischer, and M. Li, 2005, Phys. Rev. Lett. **95**, 257005.

Lin, H., S. Sahrakorpi, R. S. Markiewicz, and A. Bansil, 2006, Phys. Rev. Lett. **96**, 097001.

Liu, J., Y. Li, and C. M. Lieber, 1994, Phys. Rev. B **49**, 6234.

Loeser, A. G., Z.-X. Shen, D. S. Dessau, D. S. Marshall, C. H. Park, P. Fournier, and A. Kapitulnik, 1996, Science **273**, 325.

Löfwander, T., V. S. Shumeiko, and G. Wendin, 2001, Supercond. Sci. Technol. **14**, R53.

Lucas, A. A., H. Morawitz, G. R. Henry, J.-P. Vigneron, P. Lambin, P. H. Cutler, and T. E. Feuchtwang, 1988, Phys. Rev. B **37**, 10708.

Lyding, J. W., S. Skala, J. S. Hubacek, R. Brockenbrough, and G. Gammie, 1988, Rev. Sci. Instrum. **59**, 1897.

Maggio-Aprile, I., 1996, Ph.D. thesis, University of Geneva.

Maggio-Aprile, I., C. Renner, A. Erb, E. Walker, and Ø. Fischer, 1995, Phys. Rev. Lett. **75**, 2754.

Maggio-Aprile, I., C. Renner, A. Erb, E. Walker, and Ø. Fischer, 1997, Nature (London) **390**, 487.

Maggio-Aprile, I., C. Renner, A. Erb, E. Walker, B. Revaz, J.-Y. Genoud, K. Kadowaki, and Ø. Fischer, 2000, J. Electron Spectrosc. Relat. Phenom. **109**, 147.

Mahan, G. D., 1990, *Many-Particle Physics*, 2nd ed. (Plenum, New York).

Maki, M., T. Nishizaki, K. Shibata, T. Sasaki, and N. Kobayashi, 2001, Physica C **357**, 291.

Mallet, P., D. Roditchev, W. Sacks, D. Défourneau, and J. Klein, 1996, Phys. Rev. B **54**, 13324.

Martin, I., A. V. Balatsky, and J. Zaanen, 2002, Phys. Rev. Lett. **88**, 097003.

Martinez-Samper, P., J. G. Rodrigo, G. Rubio-Bollinger, H. Suderow, S. Vieira, S. Lee, and S. Tajima, 2003, Physica C **385**, 233.

Mashima, H., G. Kinoda, H. Ikuta, and T. Hasegawa, 2003, Physica C **388**, 275.

Maśka, M. M., and M. Mierzejewski, 2003, Phys. Rev. B **68**, 024513.

Massidda, S., J. Yu, and A. J. Freeman, 1988, Physica C **152**, 251.

Matsuba, K., H. Sakata, N. Kosugi, H. Nishimori, and N. Nishida, 2003, J. Phys. Soc. Jpn. **72**, 2153.

Matsuba, K., H. Sakata, T. Mochiku, K. Hirata, and N. Nishida, 2003, Physica C **388**, 281.

Matsuda, A., T. Fujii, and T. Watanabe, 2003, Physica C **388-389**, 207.

Matsuda, A., S. Sugita, and T. Watanabe, 1999a, in *Advances in Superconductivity XI*, edited by N. Koshizuka and S. Tajima (Springer-Verlag, Berlin), Vol. 1, p. 151.

Matsuda, A., S. Sugita, and T. Watanabe, 1999b, Phys. Rev. B **60**, 1377.

Matsui, T., H. Kambara, and H. Fukuyama, 2000, J. Low Temp. Phys. **121**, 803.

Matsuura, S., T. Taneda, W. Yamaguchi, H. Sugawara, T. Hasegawa, and K. Kitazawa, 1998, Physica C **300**, 26.

Mattheiss, L. F., and D. R. Hamann, 1988, Phys. Rev. B **38**, 5012.

Mattuck, R. D., 1992, *A Guide to Feynman Diagrams in the Many-Body Problem*, 2nd ed. (Dover, New York).

McElroy, K., D.-H. Lee, J. E. Hoffmann, K. M. Lang, E. W. Hudson, H. Eisaki, S. Uchida, J. Lee, and J. C. Davis, 2004, e-print cond-mat/0404005.

McElroy, K., D.-H. Lee, J. E. Hoffmann, K. M. Lang, J. Lee, E. W. Hudson, H. Eisaki, S. Uchida, and J. C. Davis, 2005, Phys. Rev. Lett. **94**, 197005.

McElroy, K., J. Lee, J. A. Slezak, D.-H. Lee, H. Eisaki, S. Uchida, and J. C. Davis, 2005, Science **309**, 1048.

McElroy, K., R. W. Simmonds, J. E. Hoffman, D.-H. Lee, J. Orenstein, H. Eisaki, S. Uchida, and J. C. Davis, 2003, Nature (London) **422**, 592.

McMillan, W. L., and J. M. Rowell, 1965, Phys. Rev. Lett. **14**, 108.

Meingast, C., V. Pasler, P. Nagel, A. Rykov, S. Tajima, and P. Olsson, 2001, Phys. Rev. Lett. **86**, 1606.

Melikyan, A., and Z. Tešanović, 2005, Phys. Rev. B **71**, 214511.

Meyer, G., 1996, Rev. Sci. Instrum. **67**, 2960.

Micnas, R., M. H. Pedersen, S. Schafroth, T. Schneider, J. J. Rodríguez-Núñez, and H. Beck, 1995, Phys. Rev. B **52**, 16223.

Miller, T. G., M. McElfresh, and R. Reifenberger, 1993, Phys. Rev. B **48**, 7499.

Misra, S., S. Oh, D. J. Hornbaker, T. DiLuccio, J. N. Eckstein, and A. Yazdani, 2002a, Phys. Rev. Lett. **89**, 087002.

Misra, S., S. Oh, D. J. Hornbaker, T. DiLuccio, J. N. Eckstein, and A. Yazdani, 2002b, Phys. Rev. B **66**, 100510.

Misra, S., M. Vershinin, P. Phillips, and A. Yazdani, 2004, Phys. Rev. B **70**, 220503(R).

Miyakawa, N., P. Guptsarama, J. F. Zasadzinski, D. G. Hinks, and K. E. Gray, 1998, Phys. Rev. Lett. **80**, 157.

Miyakawa, N., J. F. Zasadzinski, L. Ozyuzer, P. Guptsarama, D. G. Hinks, C. Kendziora, and K. E. Gray, 1999, Phys. Rev. Lett. **83**, 1018.

Moler, K. A., D. J. Baar, J. S. Urbach, R. Liang, W. N. Hardy, and A. Kapitulnik, 1994, Phys. Rev. Lett. **73**, 2744.

Momono, N., A. Hashimoto, Y. Kobatake, M. Oda, and M. Ido, 2005, J. Phys. Soc. Jpn. **74**, 2400.

Moreo, A., D. J. Scalapino, and S. R. White, 1992, Phys. Rev. B **45**, 7544.

Morita, Y., M. Kohmoto, and K. Maki, 1997a, Europhys. Lett. **40**, 207.

Morita, Y., M. Kohmoto, and K. Maki, 1997b, Phys. Rev. Lett. **78**, 4841.

Moussy, N., H. Courtois, and B. Pannetier, 2001, Rev. Sci. Instrum. **72**, 128.

Murakami, H., and R. Aoki, 1995, J. Phys. Soc. Jpn. **64**, 1287.

Murakami, H., H. Asaoka, K. Sakai, T. Ito, and M. Tonouchi, 2001, Appl. Surf. Sci. **175-176**, 306.

Naaman, O., and R. C. Dynes, 2003, Int. J. Mod. Phys. B **17**, 3569.

Naaman, O., and R. C. Dynes, 2004, Solid State Commun. **129**, 299.

Naaman, O., W. Teizer, and R. C. Dynes, 2001, Phys. Rev. Lett. **87**, 097004.

Nakano, T., N. Momono, M. Oda, and M. Ido, 1998, J. Phys. Soc. Jpn. **67**, 2622.

Nakano, T., N. Momono, M. Oda, and M. Ido, 2003, J. Phys. Soc. Jpn. **67**, 2622.

Nantoh, M., T. Hasegawa, M. Kawasaki, J. P. Gong, K. Fujito, A. Takagi, W. Yamaguchi, M. Ogino, H. Koinuma, and K. Kitazawa, 1994, J. Supercond. **7**, 349.

Nantoh, M., T. Hasegawa, W. Yamaguchi, A. Takagi, M. Ogino, K. Kitazawa, M. Kawasaki, J. P. Gong, and H. Koinuma, 1994, J. Appl. Phys. **75**, 5227.

Nantoh, M., M. Kawasaki, T. Hasegawa, K. Fujito, W. Yamaguchi, H. Koinuma, and K. Kitazawa, 1995, Physica C **242**, 277.

Ness, H., and A. J. Fisher, 1997, Phys. Rev. B **56**, 12469.

Ng, K.-W., and A. K. Gupta, 2000, Physica B **284**, 659.

Nicol, J., S. Shapiro, and P. H. Smith, 1960, Phys. Rev. Lett. **5**, 461.

Nishimori, H., K. Uchiyama, S.-i. Kaneko, A. Tokura, H. Takeya, K. Hirata, and N. Nishida, 2004, J. Phys. Soc. Jpn. **73**, 3247.

Nishiyama, M., 1996, Mater. Sci. Eng., B **41**, 93.

Nishiyama, N., G. Kinoda, S. Shibata, T. Hasegawa, N. Koshizuka, and M. Murakami, 2002, J. Supercond. **15**, 351.

Noguera, C., 1990, Phys. Rev. B **42**, 1629.

Norman, M. R., H. Ding, M. Randeria, J. C. Campuzano, T. Yokoya, T. Takeuchi, T. Takahashi, T. Mochiku, K. Kadowaki, P. Guptsarama, and D. G. Hinks, 1998, Nature (London) **392**, 157.

Norman, M. R., and C. Pépin, 2003, Rep. Prog. Phys. **66**, 1547.

Oda, M., K. Hoya, R. Kubota, C. Manabe, N. Momono, T. Nakano, and M. Ido, 1997, Physica C **281**, 135.

Oda, M., C. Manabe, and M. Ido, 1996, Phys. Rev. B **53**, 2253.

Oda, M., T. Matsuzaki, N. Momono, and M. Ido, 2000, Physica C **341**, 847.

Orenstein, J., and A. J. Millis, 2000, Science **288**, 468.

Ozyuzer, L., J. F. Zasadzinski, K. E. Gray, C. Kendziora, and N. Miyakawa, 2002, Europhys. Lett. **58**, 589.

Ozyuzer, L., J. F. Zasadzinski, C. Kendziora, and K. E. Gray, 2000, Phys. Rev. B **61**, 3629.

Pan, S. H., E. W. Hudson, and J. C. Davis, 1998, Appl. Phys. Lett. **73**, 2992.

Pan, S. H., E. W. Hudson, and J. C. Davis, 1999, Rev. Sci. Instrum. **70**, 1459.

Pan, S. H., E. W. Hudson, A. K. Gupta, K.-W. Ng, H. Eisaki, S. Uchida, and J. C. Davis, 2000, Phys. Rev. Lett. **85**, 1536.

Pan, S. H., E. W. Hudson, K. M. Lang, H. Eisaki, S. Uchida, and J. C. Davis, 2000, Nature (London) **403**, 746.

Pan, S. H., E. W. Hudson, J. Ma, and J. C. Davis, 1998, Appl. Phys. Lett. **73**, 58.

Pan, S. H., J. P. O'Neal, R. L. Badzey, C. Chamon, H. Ding, J. R. Engelbrecht, Z. Wang, H. Eisaki, S. Uchida, A. K. Gupta, K.-W. Ng, E. W. Hudson, K. M. Lang, and J. C. Davis, 2001, Nature (London) **413**, 282.

Paramekanti, A., M. Randeria, and N. Trivedi, 2001, Phys. Rev. Lett. **87**, 217002.

Pavarini, E., I. Dasgupta, T. Saha-Dasgupta, O. Jepsen, and O. K. Andersen, 2001, Phys. Rev. Lett. **87**, 047003.

Phillips, J. C., A. Saxena, and A. R. Bishop, 2003, Rep. Prog. Phys. **66**, 2111.

Pietzsch, O., A. Kubetzka, D. Haude, M. Bode, and R. Wiesendanger, 2000, Rev. Sci. Instrum. **71**, 424.

Podolsky, D., E. Demler, K. Damle, and B. I. Halperin, 2003, Phys. Rev. B **67**, 094514.

Polkovnikov, A., S. Sachdev, and M. Vojta, 2001, Phys. Rev. Lett. **86**, 296.

Prange, R. E., 1963, Phys. Rev. **131**, 1083.

Presland, M. R., J. L. Tallon, R. G. Buckley, R. S. Liu, and N. E. Flower, 1991, Physica C **176**, 95.

Randeria, M., N. Trivedi, A. Moreo, and R. T. Scalettar, 1992, Phys. Rev. Lett. **69**, 2001.

Ranninger, J., J. M. Robin, and M. Eschrig, 1995, Phys. Rev. Lett. **74**, 4027.

Rantner, W., and X.-G. Wen, 2000, Phys. Rev. Lett. **85**, 3692.

Renner, C., 1993, Ph.D. thesis, University of Geneva.

Renner, C., and Ø. Fischer, 1994a, Physica C **235**, 53.

Renner, C., and Ø. Fischer, 1994b, Proc. SPIE **2158**, 135.

Renner, C., and Ø. Fischer, 1995, Phys. Rev. B **51**, 9208.

Renner, C., A. D. Kent, P. Niedermann, and Ø. Fischer, 1991, Phys. Rev. Lett. **67**, 1650.

Renner, C., I. Maggio-Aprile, A. Erb, E. Walker, and Ø. Fischer, 1996, Proc. SPIE **2696B**, 322.

Renner, C., P. Niedermann, A. D. Kent, and Ø. Fischer, 1990, Rev. Sci. Instrum. **61**, 965.

Renner, C., B. Revaz, J.-Y. Genoud, K. Kadowaki, and Ø. Fischer, 1998, Phys. Rev. Lett. **80**, 149.

Renner, C., B. Revaz, K. Kadowaki, I. Maggio-Aprile, and Ø. Fischer, 1998, Phys. Rev. Lett. **80**, 3606.

Renner, Ch., and Ø. Fischer, 1993, unpublished.

Rodrigo, J. G., and S. Vieira, 2004, Physica C **404**, 306.

Rossel, C., R. R. Schulz, A. Schilling, H. R. Ott, and J. Karpinski, 1994, Physica C **235**, 1871.

Rusinov, A. I., 1969, Sov. Phys. JETP **29**, 1101.

Sachdev, S., 2003, Rev. Mod. Phys. **75**, 913.

Sacks, W., S. Gauthier, S. Rousset, and J. Klein, 1988, Phys. Rev. B **37**, 4489.

Sacks, W., and C. Noguera, 1991, Phys. Rev. B **43**, 11612.

Sakata, H., A. Katagiri, M. Yokoi, T. Kato, and H. Morimoto, 2003, J. Low Temp. Phys. **131**, 275.

Sakata, H., M. Oosawa, K. Matsuba, N. Nishida, H. Takeya, and K. Hirata, 2000, Phys. Rev. Lett. **84**, 1583.

Salkola, M. I., A. V. Balatsky, and D. J. Scalapino, 1996, Phys. Rev. Lett. **77**, 1841.

Scalapino, D. J., J. R. Schrieffer, and J. W. Wilkins, 1966, Phys. Rev. **148**, 263.

Schmalian, J., S. Grabowski, and K. H. Bennemann, 1997, Phys. Rev. B **56**, R509.

Schopohl, N., and K. Maki, 1995, Phys. Rev. B **52**, 490.

Schrieffer, J. R., 1964, Rev. Mod. Phys. **36**, 200.

Schrieffer, J. R., D. J. Scalapino, and J. W. Wilkins, 1963, Phys. Rev. Lett. **10**, 336.

Schulz, H. J., 1989, Phys. Rev. B **39**, 2940.

Schulz, R. R., and C. Rossel, 1994, Rev. Sci. Instrum. **65**, 1918.

Šestović, D., and M. Šunjić, 1995, Phys. Rev. B **51**, 13760.

Shan, L., A. Ejov, A. Volodin, V. V. Moshchalkov, H. H. Wen, and C. T. Lin, 2003, Europhys. Lett. **61**, 681.

Shiba, H., 1968, Prog. Theor. Phys. **40**, 435.

Shibata, K., M. Maki, T. Nishizaki, and N. Kobayashi, 2003a, Physica C **388-389**, 277.

Shibata, K., M. Maki, T. Nishizaki, and N. Kobayashi, 2003b, Physica C **392-396**, 323.

Shih, C. K., R. M. Feenstra, and G. V. Chandrashekhar, 1991, Phys. Rev. B **43**, 7913.

Shore, J. D., M. Huang, A. T. Dorsey, and J. P. Sethna, 1989, Phys. Rev. Lett. **62**, 3089.

Singh, D. J., and W. E. Pickett, 1995, Phys. Rev. B **51**, 3128.

Soininen, P. I., C. Kallin, and A. J. Berlinsky, 1994, Phys. Rev. B **50**, 13883.

Sosolik, C. E., J. A. Stroscio, M. D. Stiles, E. W. Hudson, S. R. Blankenship, A. P. Fein, and R. J. Celotta, 2003, Phys. Rev. B **68**, 140503.

Stroscio, J. A., and W. J. Kaiser, 1993, Eds., *Scanning Tunneling Microscopy*, Vol. 27 of *Methods of Experimental Physics* (Academic, Boston).

Suderow, H., M. Crespo, P. Martinez-Samper, J. G. Rodrigo, G. Rubio-Bollinger, S. Vieira, N. Luchier, J. P. Brison, and P. C. Canfield, 2002, Physica C **369**, 106.

Sugita, S., T. Watanabe, and A. Matsuda, 2000, Phys. Rev. B **62**, 8715.

Sutherland, M., S. Y. Li, D. G. Hawthorn, R. W. Hill, F. Ronning, M. A. Tanatar, J. Paglione, H. Zhang, L. Taillefer, J. DeBenedictis, R. Liang, D. A. Bonn, and W. N. Hardy, 2005, Phys. Rev. Lett. **94**, 147004.

Suzuki, K., K. Ichimura, K. Nomura, and S. Takekawa, 1999a, Phys. Rev. Lett. **83**, 616.

Suzuki, K., K. Ichimura, K. Nomura, and S. Takekawa, 1999b, J. Phys.: Condens. Matter **11**, 3133.

Suzuki, M., T. Watanabe, and A. Matsuda, 1999c, Phys. Rev. Lett. **82**, 5361.

Szpunar, B., and V. H. Smith, Jr., 1992, Phys. Rev. B **45**, 10616.

Tachiki, M., S. Takahashi, F. Steglich, and H. Adrian, 1990, Z. Phys. B: Condens. Matter **80**, 161.

Takigawa, M., M. Ichioka, and K. Machida, 2004, J. Phys. Soc. Jpn. **73**, 450.

Tallon, J. L., and J. W. Loram, 2001, Physica C **349**, 53.

Tanaka, S., E. Ueda, and M. Sato, 1994, Physica C **224**, 126.

Tanaka, S., E. Ueda, M. Sato, K. Tamasaku, and S. Uchida, 1995, J. Phys. Soc. Jpn. **64**, 1476.

Tanaka, S., E. Ueda, M. Sato, K. Tamsaku, and S. Uchida, 1996, J. Phys. Soc. Jpn. **65**, 2212.

Tang, J.-M., and M. E. Flatté, 2004, Phys. Rev. B **70**, 140510(R).

Tao, H. J., F. Lu, and E. L. Wolf, 1997, Physica C **282-287**, 1507.

Tersoff, J., 1989, Phys. Rev. B **40**, 11990.

Tersoff, J., and D. R. Hamann, 1983, Phys. Rev. Lett. **50**, 1998.

Tersoff, J., and D. R. Hamann, 1985, Phys. Rev. B **31**, 805.

Tešanović, Z., 2004, Phys. Rev. Lett. **93**, 217004.

Tessmer, S. H., J. W. Lyding, and D. J. van Harlingen, 1994, Rev. Sci. Instrum. **65**, 2855.

Timusk, T., and B. Statt, 1999, Rep. Prog. Phys. **62**, 61.

Tinkham, M., 1996, *Introduction to Superconductivity*, 2nd ed. (McGraw-Hill, New York).

Troyanovski, A. M., J. Aarts, and P. H. Kes, 1999, Nature (London) **19**, 665.

Troyanovski, A. M., M. van Hecke, N. Saha, J. Aarts, and P. H. Kes, 2002, Phys. Rev. Lett. **89**, 147006.

Tsuchiura, H., M. Ogata, Y. Tanaka, and S. Kashiwaya, 2003, Phys. Rev. B **68**, 012509.

Tsuei, C. C., and J. R. Kirtley, 2000, Rev. Mod. Phys. **72**, 969.

Tsukada, M., K. Kobayashi, N. Isshiki, S. Watanabe, H. Kageshima, and T. Schimizu, 1993, in *Scanning Tunneling Microscopy*, edited by R. Wiesendanger and H.-J. Güntherodt (Springer-Verlag, Berlin), Vol. III, p. 77.

Ueno, S., S. Kashiwaya, N. Terada, A. Sawa, N. Matsubara, M. Koyanagi, Y. Tanaka, Y. Tanuma, K. Obara, and K. Takita, 2001, Physica C **357-360**, 1576.

Ueno, S., S. Kashiwaya, N. Terada, Y. Tanaka, Y. Tanuma, M. Koyanagi, and K. Obara, 2003, Physica C **388-389**, 301.

Upward, M. D., J. W. Janssen, L. Gurevich, A. F. Morpurgo, and L. P. Kouwenhoven, 2001, Appl. Phys. A: Mater. Sci. Process. **72**, S253.

Urazhdin, S., I. J. Maasilta, S. Chakraborty, I. Moraru, and S. H. Tessmer, 2000, Rev. Sci. Instrum. **71**, 4170.

Varlamov, S. V., M. V. Eremin, and I. M. Eremin, 1997, JETP Lett. **66**, 569.

Varma, C. M., 1997, Phys. Rev. B **55**, 14554.

Vedneev, S. I., A. G. M. Jansen, E. Haanappel, and P. Wyder, 1999, Phys. Rev. B **60**, 12467.

Vershinin, M., A. Misra, S. Ono, Y. Abe, Y. Ando, and A. Yazdani, 2004, Science **303**, 1995.

Vershinin, M., S. Misra, Y. Abe, S. Ono, Y. Ando, and A. Yazdani, 2004, Physica C **480**, 764.

Vinnikov, L. Y., L. A. Gurevich, G. A. Emel'chenko, and Y. A. Osip'yan, 1988, JETP Lett. **47**, 131.

Vlasko-Vlasov, V. K., L. A. Dorosinskii, A. A. Polyanskii, V. I. Nikitenko, U. Welp, B. W. Veal, and G. W. Crabtree, 1994, Phys. Rev. Lett. **72**, 3246.

Vobornik, I., R. Gatt, T. Schmauder, B. Frazer, R. J. Kelley, C. Kendziora, M. Grioni, M. Onellion, and G. Margaritondo, 1999, Physica C **318**, 589.

Vojta, M., 2002, Phys. Rev. B **66**, 104505.

Vojta, M., and S. Sachdev, 1999, Phys. Rev. Lett. **83**, 3916.

Volodin, A. P., A. A. Golubov, and J. Aarts, 1997, Z. Phys. B: Condens. Matter **102**, 317.

Volovik, G. E., 1993, JETP Lett. **58**, 469.

Wan, J.-C., A. M. Goldman, and J. Maps, 1989, Physica C **153-155**, 1377.

Wang, C., B. Giambattista, C. G. Slough, R. V. Coleman, and M. A. Subramanian, 1990, Phys. Rev. B **42**, 8890.

Wang, Q.-H., 2004, Phys. Rev. Lett. **92**, 057003.

Wang, Q.-H., and D.-H. Lee, 2003, Phys. Rev. B **67**, 020511(R).

Wang, Y., and A. H. MacDonald, 1995, Phys. Rev. B **52**, R3876.

Wang, Y., Z. A. Xu, T. Kakeshita, S. Uchida, S. Ono, Y. Ando, and N. P. Ong, 2001, Phys. Rev. B **64**, 224519.

Warren, W. W., R. E. Walstedt, Jr., G. F. Brennert, R. J. Cava, R. Tycko, R. F. Bell, and G. Dabbagh, 1989, Phys. Rev. Lett. **62**, 1193.

Wei, J. Y. T., C. C. Tsuei, P. J. M. van Bentum, Q. Xiong, C. W. Chu, and M. K. Wu, 1998, Phys. Rev. B **57**, 3650.

Wei, J. Y. T., N.-C. Yeh, D. F. Garrigus, and M. Strasik, 1998, Phys. Rev. Lett. **81**, 2542.

Welp, U., T. Gardiner, D. Gunter, J. Fendrich, G. W. Crabtree, V. K. Vlasko-Vlasov, and V. I. Nikitendo, 1994, Physica C **235-240**, 237.

Wen, X.-G., and P. A. Lee, 1996, Phys. Rev. Lett. **76**, 503.

White, S. R., and D. J. Scalapino, 1998, Phys. Rev. Lett. **80**, 1272.

White, S. R., and D. J. Scalapino, 2004, Phys. Rev. B **70**, 220506(R).

Wiebe, J., A. Wachowiak, F. Meier, D. Haude, T. Foster, M. Morgenstern, and R. Wiesendanger, 2004, Rev. Sci. Instrum. **75**, 4871.

Wiesendanger, R., and D. Anselmetti, 1992, in *Scanning Tunneling Microscopy*, edited by R. Wiesendanger and H.-J. Güntherodt (Springer-Verlag, Berlin), Vol. I, p. 131.

Wiesendanger, R., and H.-J. Güntherodt, 1993, Eds., *Scanning Tunneling Microscopy* (Springer-Verlag), Vol. III.

Wittneven, C., R. Dombrowski, S. H. Pan, and R. Wiesendanger, 1997, Rev. Sci. Instrum. **68**, 3806.

Wolf, E. L., 1985, *Principles of Electron Tunneling Spectroscopy* (Oxford University Press, New York).

Wolf, E. L., A. Chang, Z. Y. Rong, Y. M. Ivanchenko, and F. R. Lu, 1994, J. Supercond. **7**, 355.

Won, H., and K. Maki, 1994, Phys. Rev. B **49**, 1397.

Won, H., and K. Maki, 1995, Europhys. Lett. **30**, 421.

Wu, C., T. Xiang, and Z.-B. Su, 2000, Phys. Rev. B **62**, 14427.

Yang, K., and S. L. Sondhi, 1998, Phys. Rev. B **57**, 8566.

Yasui, K., and T. Kita, 1999, Phys. Rev. Lett. **83**, 4168.

Yazdani, A., C. M. Howald, C. P. Lutz, A. Kapitulnik, and D. M. Eigler, 1999, Phys. Rev. Lett. **83**, 176.

Yazdani, A., B. A. Jones, C. P. Lutz, M. F. Crommie, and D. M. Eigler, 1997, Science **275**, 1767.

Yeh, N. C., C. T. Chen, G. Hammerl, J. Mannhart, A. Schmehl, C. W. Schneider, R. R. Schulz, S. Tajima, K. Yoshida, D. Garrigus, and M. Strasik, 2001, Phys. Rev. Lett. **87**, 087003.

Yeh, N. C., *et al.*, 2002, Physica C **367**, 174.

Yu, L., 1965, Acta Phys. Sin. **21**, 75.

Yurgens, A., D. Winkler, T. Claeson, S. Hwang, and J. Choy, 1999, Int. J. Mod. Phys. B **13**, 3758.

Yurgens, A., D. Winkler, T. Claeson, S. Ono, and Y. Ando, 2003, Phys. Rev. Lett. **90**, 147005.

Yurgens, A., D. Winkler, T. Claeson, S. Ono, and Y. Ando, 2004, Phys. Rev. Lett. **92**, 259702.

Yusof, Z., J. F. Zasadzinski, L. Coffey, and N. Miyakawa, 1998, Phys. Rev. B **58**, 514.

Zaanen, J., and O. Gunnarsson, 1989, Phys. Rev. B **40**, 7391.

Zandbergen, H. W., W. A. Groen, F. C. Mijlhoff, G. van Tendeloo, and S. Amelinkx, 1998, Physica C **156**, 325.

Zasadzinski, J. F., L. Coffey, P. Romano, and Z. Yusof, 2003, Phys. Rev. B **68**, 180504.

Zasadzinski, J. F., L. Ozyuzer, N. Miyakawa, K. E. Gray, and C. Kendziora, 2001, Phys. Rev. Lett. **87**, 067005.

Zavaritsky, V. N., 2004a, Phys. Rev. Lett. **92**, 259701.

Zavaritsky, V. N., 2004b, Physica C **404**, 440.

Zawadowski, A., 1967, Phys. Rev. **163**, 341.

Zhang, D., and C. S. Ting, 2003, Phys. Rev. B **67**, 100506(R).

Zhang, H., U. Memmert, R. Houbertz, and U. Hartmann, 2001, Rev. Sci. Instrum. **72**, 2613.

Zhang, K., D. A. Bonn, S. Kamal, R. Liang, D. J. Baar, W. N. Hardy, D. Basov, and T. Timusk, 1994, Phys. Rev. Lett. **73**,

2484.

Zhang, S.-C., 1997, Science **275**, 1089.

Zhang, Y., E. Demler, and S. Sachdev, 2002, Phys. Rev. B **66**, 094501.

Zhao, X., S. Nakao, K. Ueno, G. Kinoda, T. Endo, T. Hanaguri, K. Kitazawa, and T. Hasegawa, 2000, Physica B **284**, 1065.

Zhu, J.-X., I. Martin, and A. R. Bishop, 2002, Phys. Rev. Lett. **89**, 067003.

Zhu, J.-X., and C. S. Ting, 2001a, Phys. Rev. B **64**, 060501(R).

Zhu, J.-X., and C. S. Ting, 2001b, Phys. Rev. Lett. **87**, 147002.

Zhu, J.-X., C. S. Ting, and C.-R. Hu, 2000, Phys. Rev. B **62**, 6027.